Development of Porous and Patient-Specific Shape Memory Polymer Composites as an Embolic Agent for Endovascular Embolization

A Thesis

submitted in partial fulfilment of the requirements

for the award of the degree of

Doctor of Philosophy

by

Devarshi Kashyap
(Roll No.-136103003)

DEPARTMENT OF MECHANICAL ENGINEERING
INDIAN INSTITUTE OF TECHNOLOGY GUWAHATI
GUWAHATI-781039
INDIA

December 2021

Department of Mechanical Engineering
Indian Institute of Technology Guwahati
Guwahati-781039, Assam, India

CERTIFICATE

It is certified that the work contained in the thesis entitled "**Development of Porous and Patient-Specific Shape Memory Polymer Composites as an Embolic Agent for Endovascular Embolization**" submitted by **Mr. DEVARSHI KASHYAP** to the Indian Institute of Technology Guwahati, Guwahati, India for the award of degree of Doctor of Philosophy has been carried out under our supervision in the department of Mechanical Engineering, Indian Institute of Technology Guwahati. This work has not been submitted elsewhere for the award of any other degree or diploma.

Dr. S. KANAGARAJ
Professor
Department of Mechanical Engineering
Indian Institute of Technology Guwahati
Assam, India

ABSTRACT

Implantation of embolic agents with the help of interventional radiology technique to occlude a blood vessel suffering from medical complications such as aneurysms, arteriovenous malformations, tumors, etc., is being increasingly used as an alternative to conventional surgery. Fewer complications, less pain, affordability, better outcomes, and lesser recovery time are some of the advantages of minimally invasive surgery. However, the currently used embolic agents have issues such as non-target embolization, incomplete occlusion, coil migration, recanalization, and others. The objective of the present work is to develop a radiopaque, porous, and patient-specific shape memory polymer (SMP) based embolizing agent for interventional radiology technique that overcomes the limitations of the currently used embolic agents. In this regard, a novel fabrication technique has been developed by combining extrusion, fused filament fabrication (FFF), and salt leaching process to produce the patient-specific porous composites. Initially, tungsten (7wt%) as a radiopaque filler and NaCl (43wt%) as a pore-forming agent are dispersed in acetone and mixed with shape memory polyurethane (SMPU) (50wt%) to obtain the coated polymer pellets, which are extruded to produce the filaments to be used in FFF process. The FFF printing process is used to fabricate the shape memory polyurethane composites (SMPC) having the desired shape, and the NaCl particles are leached out to produce the porous structure. The 3D printed porous Tungsten composite has the following features: improved radiopacity, porosity of about 32.7% with pore sizes of <250 μm, interconnected porous network, and excellent shape holding and shape recovery characteristics up to 100%. However, the tungsten used in the porous SMPC is oxidized during the shelf aging period, and its cytotoxic behaviour is also observed during the biocompatibility studies. Hence, different types of radiopaque SMPU composites have been developed by adding barium sulphate for radiopacity and hydroxyapatite for embolization to complement the novel processing technique. Nano $BaSO_4$ (4wt%,10wt%, and 12.5wt%)

SMPU composites, nanohydroxyapatite (2.5wt%, 5wt%, 7.5wt%, and 10wt%) SMPU composites, and hybrid composites (2.5wt%HaP/7.5wt%$BaSO_4$, 5wt%HaP/5wt%$BaSO_4$, 2.5wt%HaP/7.5wt%$BaSO_4$) are fabricated by extrusion and compression molding process. The nano $BaSO_4$ SMPU composite has improved radiopacity and shape recovery characteristics than the other composites proposed in this study. It is also observed that the programming temperature of the temporary shape of the sample is found to influence the total shape recovery volume and the rate of recovery. The higher albumin: fibrinogen (A:F) ratio of the nano $BaSO_4$ composite in the protein adsorption test compared to SMPU predicts a lesser probability of thrombosis in the composites, which enhances its suitability for a blood-contacting medical implant. Based on the different characterization techniques and the biocompatibility studies, the nano $BaSO_4$ (10wt%) is found to be a suitable radiopaque material to fabricate the 3D printed SMPU composites by the novel processing technique. The storage modulus of the 3D printed porous nano $BaSO_4$ SMPC in the rubbery state is observed to be in the similar range of the elastic modulus of the wall of an abdominal aortic aneurysm, which makes it suitable for the embolization process. The switching temperature of 3D printed porous SMPU is not influenced by the addition of 10 wt% $BaSO_4$ nanoparticles. The viability of the deployment of SMPC in an aneurysm is successfully tested in an in-house developed aneurysm simulator, and the 3D printed nano $BaSO_4$ SMPC is observed to recover completely within the aneurysm. Hence, the developed 10wt% nano $BaSO_4$ SMPU nanocomposites can be explored as embolic agent for interventional radiology technique due to their suitable mechanical properties, actuation profiles, and enhanced radiopacity.

ACKNOWLEDGEMENTS

It is my pleasure to acknowledge everyone who contributed to the journey towards the successful completion of my Ph.D. Thesis.

First and foremost, I take this opportunity to express my profound gratitude and deepest appreciation to my supervisor, Prof S Kanagaraj for his exemplary guidance, monitoring, constant support and encouragement throughout my doctoral research tenure. His vast knowledge and immense passion for research has greatly inspired me and shaped my perception of scientific research. I am extremely grateful to him for providing the essential arrangements, laboratory facilities and giving me the complete freedom in my work throughout my research days to accomplish my goals.

I would like to thank my doctoral committee members, Professor Santosha K. Dwivedy, Professor Sashindra K. Kakoty, and Professor Biman B. Mandal, for their valuable suggestions and insightful comments at different stages of my research.

A special thanks to my department and Central Instruments Facility (CIF) for providing me with a good research environment with state-of-the-art facilities. I wish to thank Prof Vimal Katiyar for allowing me to use the laboratory facilities in Centre of excellence in Sustainable polymer (CoE-SusPol).

I am extremely grateful to Professor Ajaikumar B. Kunnumakkara, Department of Biosciences and Bioengineering, Indian Institute of Technology Guwahati for his advice and allowing me the opportunity to work in his laboratory.

I would like to extend my gratitude to Mr. Jiten Basumatary, Mr. Saiffuddin Ahmed and Mr. Sanjib Sarma, for their constant support.

The completion of this work would have not been possible without the aid of Mr. Surendra Singh Gaur and Dr. Devivasha Bordoloi. I am thankful to Mr. Kishore Kumar Padi, Ms. Heta Panchal, and Dr. Akash Handique who constantly helped me in my research and provided all necessary inputs. I would also like to take this opportunity to thank all my labmates, Avanish, Vignesh, Charan, Raagdeep, Arnab, Anirban, Vaibhav, Ashirbad, Nandani, Aman, Mithinga, Mahanubhav, Nilutpal, Banamali, Arun and Priya maam, who made this research work easier and kept the working environment enjoyable. I am thankful to Dr. Kamal Basumatary, Dr. Dudul Das, and Mr. Samar Das for their help at various stages of my thesis work.

Last but not the least I place a deep sense of gratitude to my parents and family, who have been a constant source of inspiration throughout this project.

Devarshi

ABBREVIATIONS

2D	2-Dimensional
3D	3-Dimensional
4D	4-Dimensional
AAA	Abdominal Aortic Aneurysm
AM	Additive Manufacturing
AVM	Arteriovenous malformation
AVP	Amplatzer vascular plug
BCA	Bicinchoninic acid
CAD	Computer aided Design
CAGR	Compound annual growth rate
CB	Carbon black
CMF-PBS	Calcium, magnesium-free phosphate-buffered saline
COD	Crystallography Open Database
COVID	Coronavirus disease
CT	Computed tomography
DMA	Dynamic mechanical analyser
DMEM	Dulbecco's Modified Eagle Medium
DMSO	Dimethyl-sulfoxide
DSA	Digital subtracted angiography
EDTA	Disodium ethylenediamine tetraacetic acid
EDTA	Ethylenediaminetetraacetic acid
EEPROM	Electrically erasable programmable read-only memory
EVOH	Ethylene Vinyl Alcohol
FBS	Fetal bovine serum
FDM	Fused deposition modelling
FE-SEM	Field emission scanning electron microscope
FFF	Fused Filament Fabrication
FTIR	Fourier Transform Infrared Spectroscopy
GDC	Guglielmi detachable coil
HaP	Hydroxyapatite
HDI	1,6-diisocyanatohexane
IME	Individual memory element

IR	Interventional Radiology
ISO	International Organization for Standardization
JCPDS	Joint Committee on Powder Diffraction Standards
MRI	Magnetic Resonance Imaging
MTT	Methyl thiazolyl tetrazolium
NBCA	N-butyl-2 cyanoacrylate
NEMA	National Electrical Manufacturers Association
PGPLA	Polyglycolic polylactic acid
PHIL	Precipitating Hydrophobic Injectable Liquid
PPE	Personal Protection equipment
PVA	Polyvinyl alcohol
RTV	Room-temperature-vulcanizing
SAH	Subarachnoid hemorrhage
SLA	Stereolithography appartus
SLS	Selective laser sintering
SMP	Shape memory polymer
SMPC	Shape memory polymer composite
SMPU	Shape Memory Polyurethane
SRAM	Static random-access memory
T_g	Glass transition temperature
T_{sw}	Switching temperature
TAA	Thoracic Aortic Aneurysm
TCPS	Tissue-culture polystyrene
TEM	Transmission Electron microscopy
TGA	Thermogravimetric analyzer
TMHDI	2,2,4-(2,4,4-) Trimethylhexane 1,6-diisocyanate
UV	Ultraviolet
WHO	World Health Organization
XRD	X-ray diffraction

List of figures

List of Tables

CHAPTER 1: INTRODUCTION

1.1 BIOMEDICAL DEVICES

Medical devices have become a key factor in diagnosing and treating patients, and improving their overall quality of life. A medical device can be as rudimentary as a gauze bandage, walking stick to complex devices such as a cardiac pacemaker, Magnetic Resonance Imaging (MRI), etc. World Health Organization (WHO) [1] defines medical devices as "any instrument, apparatus, implement, machine, appliance, implant, reagent for *in vitro* use, software, material or other similar or related article, intended by the manufacturer to be used, alone or in combination, for human beings, for one or more of the specific medical purpose(s) of:

- diagnosis, prevention, monitoring, treatment or alleviation of disease,
- diagnosis, monitoring, treatment, alleviation of or compensation for an injury,
- investigation, replacement, modification, or support of the anatomy or of a physiological process,
- supporting or sustaining life,
- control of conception,
- disinfection of medical devices,
- providing information by means of *in vitro* examination of specimens derived from the human body;

and does not achieve its primary intended action by pharmacological, immunological or metabolic means, in or on the human body, but which may be assisted in its intended function by such means".

The global medical device market has been consistently growing due to the rapidly increasing population and consumer awareness about various medical procedures and

preventive care associated with a better and longer life. The global market for healthcare services reached a value of nearly $7,724 billion in 2017, and is expected to grow at an annual rate of 5.4% to nearly $10,059 billion by 2022 [2]. In sync with the global healthcare market, the global medical devices market has been increasing at a compound annual growth rate (CAGR) of 4.4% since 2015 and reached a value of nearly $457 billion in 2019. However, the lockdowns imposed by the different governments across the globe due to COVID-19 is expected to decrease the medical device market to $442.5 billion in 2020 at a rate of -3.2%. But, there is an extraordinary increase in the manufacturing of the ventilators, Personal Protection equipment (PPE) kits, and other kits that are used to treat COVID-19 patients. The market is expected to recover from 2021 and grow to $603.5 billion in 2023 at a CAGR of 6.1% [3]. Similarly, the Indian healthcare industry is experiencing rapid change and has become one of the India's largest sectors, both in terms of revenue and employment. Though this change has been underway for many years, it has become significantly visible during the last decade with a renewed thrust from both the government and a growing market for healthcare services and products. The healthcare market worth of $160 billion in 2017 is expected to reach $372 billion by 2022 due to increased demand for specialized and quality healthcare facilities at a predicted CAGR of 22%. Indian medical device market is worth an estimated $8 billion in 2020 and is growing at a CAGR of 15.8%, which is expected to exceed $50 billion by the end of 2025 [4].

Fig. 1.1 (a) represents the market size of the medical devices imported to India during the last five years. A steady increase in import of medical devices can be observed with an import bill of ₹ 38837 crores for the year 2018-19 from ₹ 23170 crores during 2014-15 [5]. As per WHO data for the year 2015–16, more than 74% of required medical devices, costing as high as 0.65 million USD, are being imported to India [6]. Fig. 1.1 (b) represents the category wise market share of the medical devices in India for the year 2019. Diagnostic devices such as

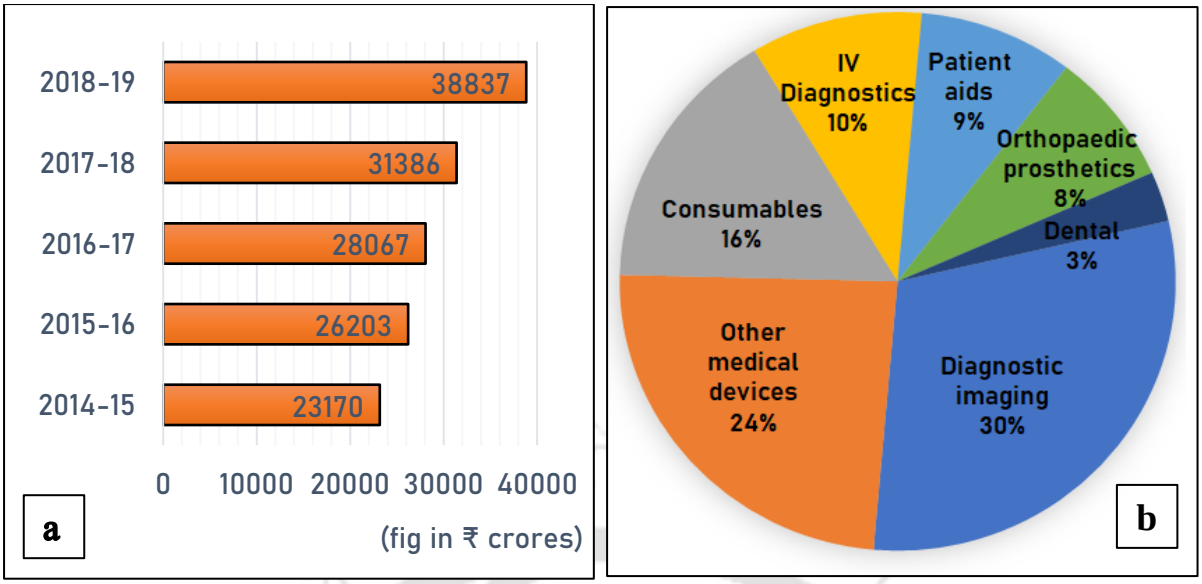

Fig. 1.1. (a) Medical devices import to India in last 5 years (adopted from [5]); (b) Segment-wise market share of medical devices in India for the year 2019 (adopted from [6])

X-ray imaging system, CT scanner, ultrasound imaging, MRI, etc. held the highest market share at 30% followed by other medical devices such as patient monitors, ECG, Oxygenators, etc. The various consumables used in hospitals and clinical laboratories have a market share of 16%. The growth of the medical device market is being fueled by an ageing population of over 100 million, rising incidences of lifestyle diseases, growing income and increased penetration of health insurance. Since, only 25% of the medical devices are developed and manufactured in India, it increases the cost of the products due to import, further, burdening the Indian consumers. Therefore, there is a genuine need for developing indigenous medical devices and implants for the Indian people.

1.2 BIOMATERIALS

The principal requirements of all medical implants/devices that are placed inside or on the surface of the body are biocompatibility, bioadhesion, and biofunctionality, which come under the aegis of a biomaterial. Biomaterial is defined as “a substance that has been engineered to take a form which, alone or as part of a complex system, is used to direct, by control of

interactions with components of living systems, the course of any therapeutic or diagnostic procedure" [7]. The ultimate goal of a biomaterial is to improve the quality of life by restoring the function of natural living tissues and organs in the human body. The distinctive characteristic of a biomaterial is the biocompatibility, which is defined as "the ability of a biomaterial to perform its desired function with respect to a medical therapy, without eliciting any undesirable local or systemic effects in the recipient or beneficiary of that therapy, but generating the most appropriate beneficial cellular or tissue response in that specific situation, and optimizing the clinically relevant performance of that therapy" [8]. Significant advancement in the field of biomaterials and the biomedical devices during the last 70 years after the end of World War II have led to the development of intraocular lenses, hip and knee prostheses, dental implants, artificial hearts, artificial kidneys, vascular grafts etc. Materials such as silicones, polyurethanes, teflon, nylon, methacrylate, hydroxyapatite, titanium, and stainless steel have been used successfully under *in vivo* conditions. Biomaterial is an interdisciplinary field involving chemists, biologist, engineers and physicians. The rapid development in all the spheres of traditional science and materials has aided in continuous progress in the field of medical devices and implants.

A medical device before being used in human trials and clinical applications must be tested under *in vitro* conditions to ensure its safety and efficacy. Medical devices in contact with the human body must undergo rigorous testing in compliance with international standards for medical devices i.e. ISO 10993: Biological evaluation of medical devices, to determine their suitability as an implant, regardless of their mechanical, physical, and chemical properties [9]. ISO 10993 consists of tests on cytotoxicity, sensitization, intradermal irritation, acute systemic toxicity, and a series of other tests depending on the types of medical devices (surface devices, external communicating devices, implant device), the period of contact (limited: ≤ 24hr,

prolonged: 24 hr-30 days, permanent: > 30 days), and the human body contact surface (skin, mucosal membrane, breached surfaces, indirect blood path, tissue/bone, and blood).

A wide range of medical devices, diagnostic products, and new techniques have been introduced in the clinical practices. One such medical technique that has been benefitted from the advancement in X-ray imaging technique is the Interventional Radiology (IR) techniques. Though X-ray was discovered in 1895 by Wilhelm Röentgen [10], the steady advancement of the technology from the nascent stage of using glass plates for viewing radiographic images to the films followed by digital sensors and Computed tomography (CT scan) has made it possible to come up with techniques like Interventional Radiology. It has a huge clinical impact and has become one of the most sought medical specialties. It has been widely accepted by the medical community that the capability of interventional radiologist will steadily increase with continued advancement in imaging technology and medical devices. Though IR technique tools such as imaging technology, implant materials, devices, and manufacturing process etc. have evolved during the last two decades, there is still a lot of scope of improvement for decreasing mortality and morbidity of patients.

1.3 INTERVENTIONAL RADIOLOGY

Interventional Radiology (IR) is a medical subspecialty of Radiology, which relies on the use of radiological image guidance such as X-ray fluoroscopy, ultrasound, computed tomography (CT) and magnetic resonance imaging (MRI) to diagnose and treat diseases in nearly every organ system. The range of diseases and organs open to image-guided therapeutic and diagnostic procedures are extensive and constantly evolving, which include, but are not limited to, diseases and elements of the vascular, gastrointestinal, hepatobiliary, genitourinary, pulmonary, musculoskeletal and the central nervous system. Most IR treatments are minimally invasive alternatives to open and laparoscopic (keyhole) surgery, where an organ is accessed

through the vasculature with the help of a catheter and the radiological imaging techniques are used for guiding the same. Typically needles, wires, catheters, balloons, snares, collapsible baskets, emboli, and other small-caliber devices, which can be sent through the blood vessels, are used in this technique. In most cases, the procedures are accomplished under local anesthesia with moderate sedation, eliminating the need for general anesthesia, which is often needed for conventional surgical interventions. Fewer complications, less pain, better outcomes, lesser recovery time, and lower cost are some of the advantages of minimally invasive surgery in comparison to conventional surgery. IR is used for Angioplasty (restore blood flow by widening the narrowed arteries), Stenting (placing a tiny tube to open clogged vessels), Thrombolysis (dissolving blood clots), Embolization (blocking or closing of blood vessels), and cancer treatment procedures such as radiofrequency ablation, microwave ablation, cryoablation, chemoembolization, and radioembolization. Embolization is selective occlusion or blocking of blood vessels using embolic agents to prevent excessive bleeding or stop blood flow into a certain part of the body. This technique is highly effective in treating diseases or conditions such as Aneurysm, Arteriovenous Malformation (AVM), tumors, etc., where occlusion of the diseased vessels is required.

1.3.1 Aneurysm

An aneurysm is a permanent focal dilatation of an artery due to weakening of the vessel wall. The weak section of the artery wall bulges out due to the pressure of the blood flow resulting in an abnormal widening, ballooning or bleb. The angiogram of an aneurysm is shown in Fig. 1.2, where the localized and abnormal swelling of the blood vessel is observed in Fig. 1.2 (a). Its drastic increase in size from 6 mm to 14 mm in 13 days is observed from Fig 1.2 (b) [11]. The sections subjected to higher blood pressure are more susceptible to aneurysm development, such as the branching points of arteries, called bifurcations, and it can

occur in the cerebral circulation as well as in peripheral arteries. Aneurysms usually remain asymptomatic until they rupture, but a ruptured aneurysm is catastrophic and generally fatal. Advanced age, hypertension, atherosclerosis (hardening of the arteries), family history, positive smoking history, and drinking are some of the factors that increase the risk of aneurysm. The decisions regarding optimal treatment of an unruptured aneurysm are made on the basis of short-term and long-term risks of aneurysm rupture. The factors that are considered before deciding on the treatment are aneurysm size and location, the patient's family and medical history, and the availability of an interventional option with an acceptable risk. Aneurysms have been categorized on the basis of blood vessel it effects: (i) Cerebral Aneurysm, and (ii) Aortic Aneurysm.

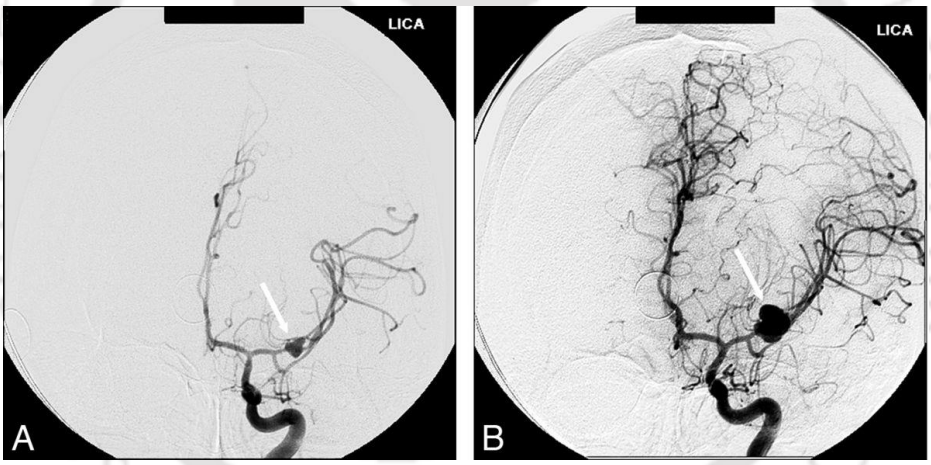

Fig. 1.2. Catheter angiograms: (a) multilobed 6mm aneurysm, (b) 13 days later the aneurysm grows to 14mm. Reproduced with permission from Ref. [11]

Cerebral aneurysms occur when the blood vessels in the brain become weak and bulge or balloon out. It can range from a few millimeters to more than a centimeter, and commonly form a berry like structure. Cerebral aneurysms having more than 7 mm diameter are at an increased risk of rupture, and the chance of rupture increases with its diameter [12]. Intracranial aneurysm rupture affects approximately 30,000 people in the United States every year, and it

can lead to severe disability or death [13]. There are almost 500,000 deaths worldwide each year caused by brain aneurysms, and half of the victims are younger than 50 years [14].

The aorta is the main artery that carries blood from the heart to other parts of the body. Depending on the origin site of the aneurysm on the aorta, Aortic aneurysm is classified into (i) Abdominal Aortic Aneurysm (AAA), and (ii) Thoracic Aortic Aneurysm (TAA). The aneurysms developed on the aorta passing through the abdomen and exceeding the normal diameter by 50%, or by >3 cm are referred as Abdominal Aortic Aneurysms. AAA is commonly occurring in 3/4th of the aortic aneurysm cases and affects about 4 - 8 % of men over 65 [15]. Men are six times more likely to have an AAA than women. A ruptured AAA is fatal in 80% of the cases; the mortality rate is 50% even after surgery and causes 5000 deaths each year in UK and 1,75,000 deaths globally [16]. Thoracic aneurysms may involve one or more aortic segments namely aortic root, ascending aorta, arch, or descending aorta. TAA is less common than AAA, however, a ruptured TAA is equally fatal as AAA. A contrast enhanced CT scan of an AAA (below the kidneys) is shown in Fig. 1.3 (a) [17].

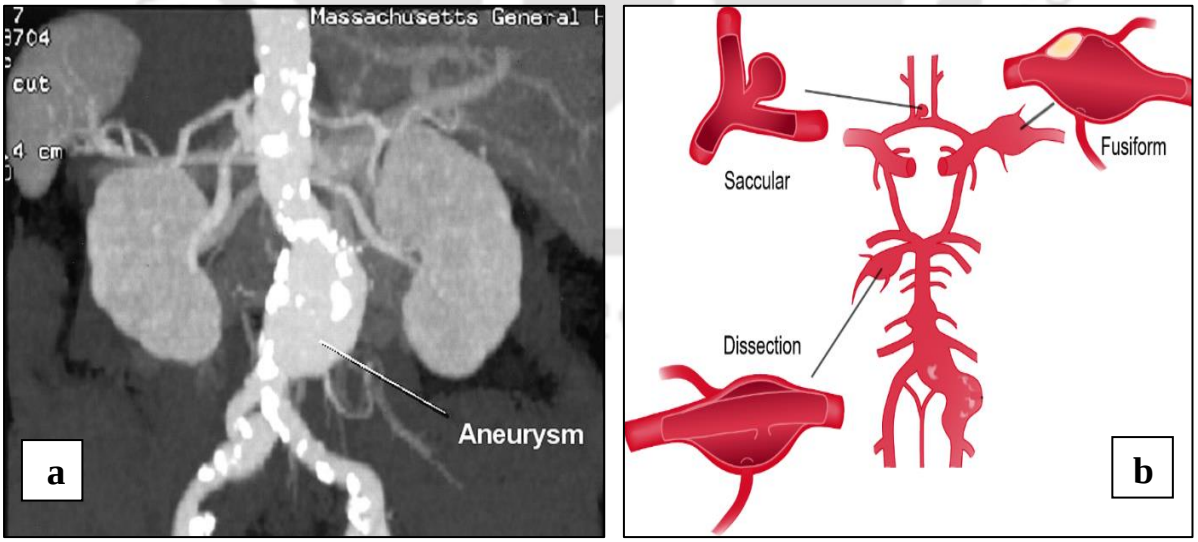

Fig. 1.3. (a) CT image of Abdominal Aortic Aneurysm (below the kidneys);
(b) Classification of aneurysm on the basis of shape. Reproduced with permission from Ref. [17,18]

Aneurysm is also classified on the basis of their shape as (i) saccular, (ii) fusiform, and (iii) dissection [18], which are shown in Fig. 1.3 (b). Saccular aneurysm dilates on only one side of the blood vessel and has a neck region which makes it easier to be treated due to the sac like shape. Fusiform aneurysm dilates on all sides of the aorta with no neck region and is fairly more common. In aortic dissection/ pseudoaneurysm, the blood flows in between the wall layers of the aorta due to tearing of the layers causing the aorta to bulge out.

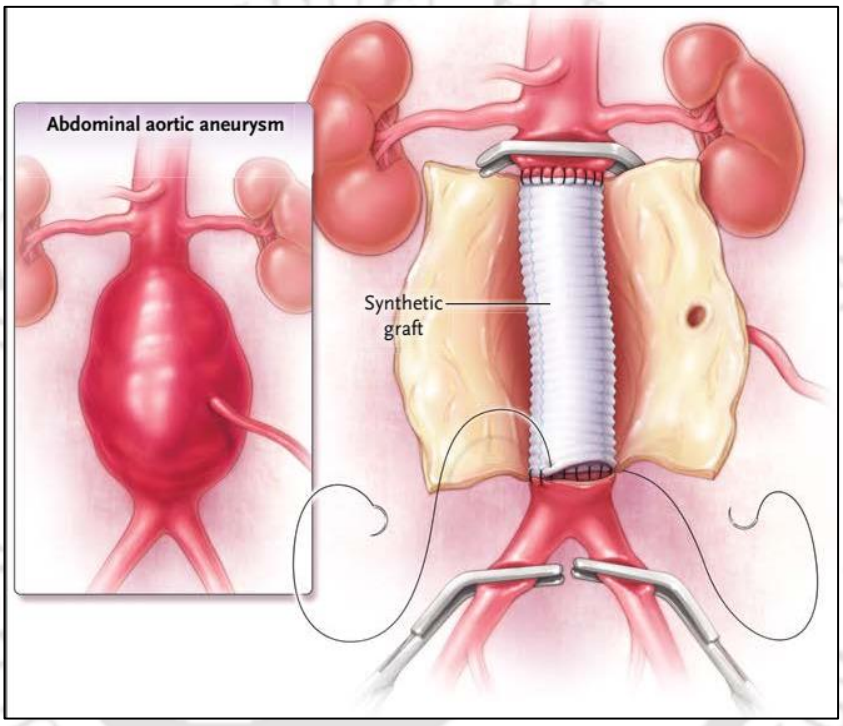

Fig. 1.4. Surgical grafting of Abdominal Aortic Aneurysm. Reproduced with permission from Ref. [19]. Copyright Massachusetts Medical Society

Aneurysms can be treated either by open surgery or endovascular approach. Conventional open surgery techniques include surgical clipping, grafting, and bypass, where the surgeon cut opens the body near the aneurysm and perform the required procedure. In grafting, the aneurysm sac is cut opened and a synthetic graft is sutured proximally and distally to the aorta as seen in Fig. 1.4 [19]. The surgical clipping procedure is shown in Fig. 1.5, and the dilated posterior inferior cerebellar artery aneurysm pre-clipping is seen in Fig. 1.5 (a). The metallic

clip is applied on the neck of the aneurysm as shown in Fig. 1.5 (b), which stops the blood flow into the aneurysm and decreases the size of the dilation [20]. These procedures cannot be performed if the aneurysm is inaccessible or the risk factor is high. Serious complications related to open surgery such as heart related problems, swelling or infections at the site, respiratory or urinary infections are always probable.

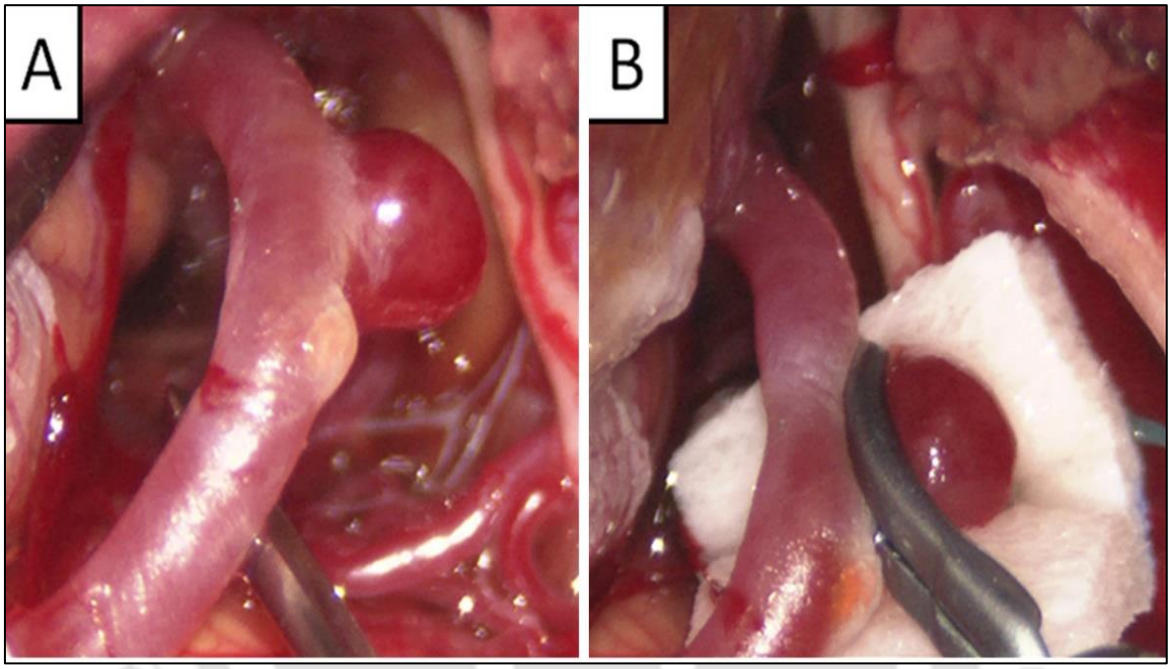

Fig 1.5. Surgical clipping of intracranial aneurysm: (a) posterior inferior cerebellar artery aneurysm prior to clipping, (b) Surgical clip placed across the neck of the aneurysm. Reproduced with permission from Ref. [20]

Minimally invasive procedures have become important in treating patients with aneurysms due to the risks associated with open surgical repair [21–23]. The ultimate goal of embolization is to fill the sac, and isolate it from the bloodstream, thus reducing the risk of aneurysm expansion and rupture [24]. The development of soft steerable microcatheters and coils has enabled safer and less traumatic intra-arterial access to aneurysms. Various embolic agents such as metal coils, polymer particulates, and liquid embolic are currently used to fill the aneurysms.

1.3.2 Arteriovenous malformation (AVM)

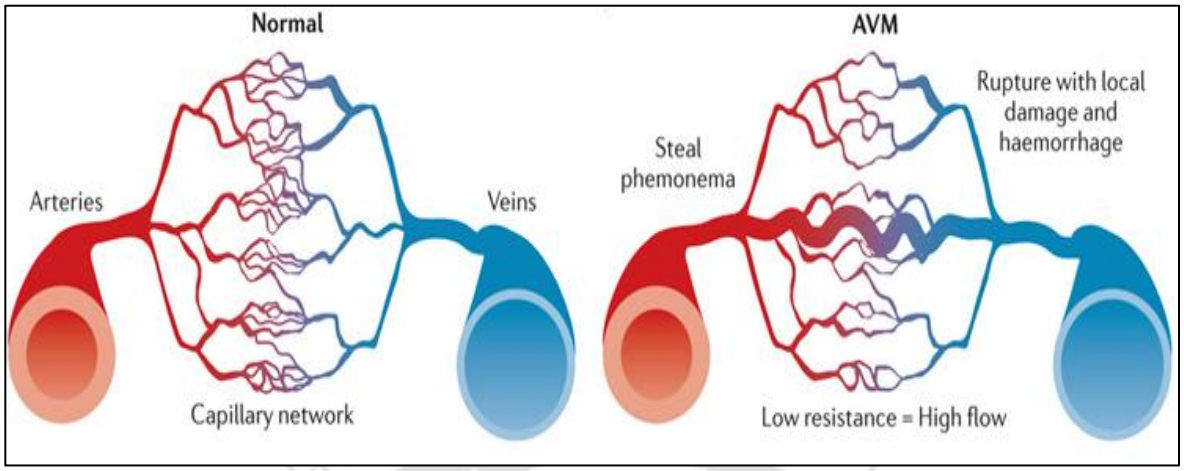

Fig. 1.6. Schematic representation of normal vasculature and an arteriovenous malformation. Reproduced with permission from Ref. [25]

AVM is an abnormal connection between the veins and arteries. Normally, the oxygenated blood is pumped from the heart through the arteries to the whole body. The arteries branch off into fine network of tiny vessels called capillaries, where the blood nourishes the tissue by exchanging oxygen and nutrients and taking waste from it. The deoxygenated blood flows back into the heart through the veins. The AVM is formed in the absence of these capillaries and is like a shortcut directly joining the arteries to veins without exchanging oxygen and nutrients as shown in Fig. 1.6 [25]. When the high-pressured blood in the arteries directly enter the thin walled veins through AVM without the damping effect of the capillaries, it might cause rupture of the vein resulting in bleeding. AVM is considered to be hereditary and occurs with equal frequency in both men and women. AVM is treated by surgery, endovascular embolization, and stereotactic radiosurgery. Surgeries are preferred when the AVM is accessible and can be removed with less risk of significant damage to the surrounding tissues. In endovascular embolization, embolic agents are injected on the AVM to reduce the blood flow. Stereotactic radiosurgery uses highly focused radiation to damage the blood vessels to stop blood flow to the AVM.

1.4 CLINICALLY USED EMBOLIC AGENTS

The embolic agents that are currently being used by the interventional radiologist for the closure of diseased parts or blood vessels are presented in Fig. 1.7 [26]. The embolic agents can be broadly classified into (i) mechanical devices, (ii) particulates, and (iii) liquids/gel which are explained in detail in the following sections.

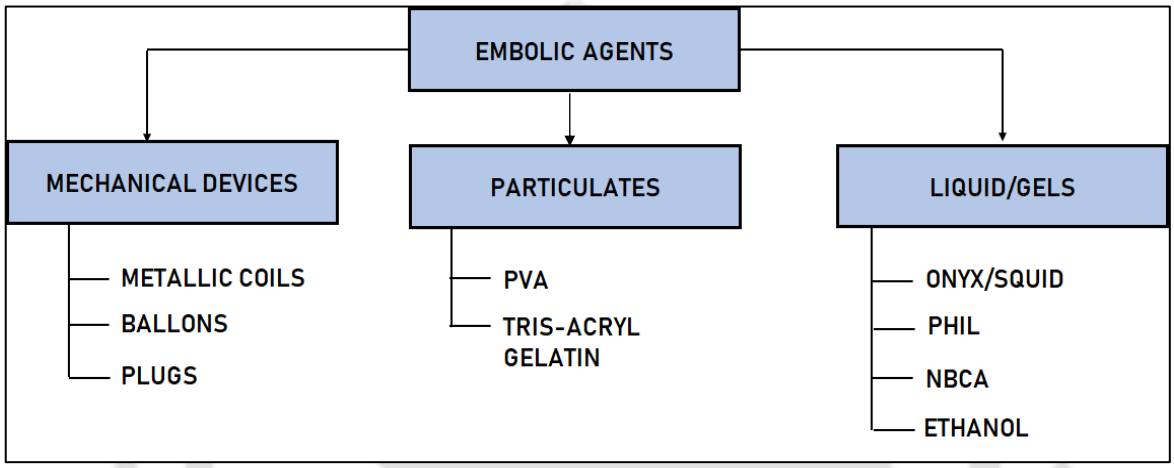

Fig.1.7. Available embolic agents

1.4.1 Mechanical Devices

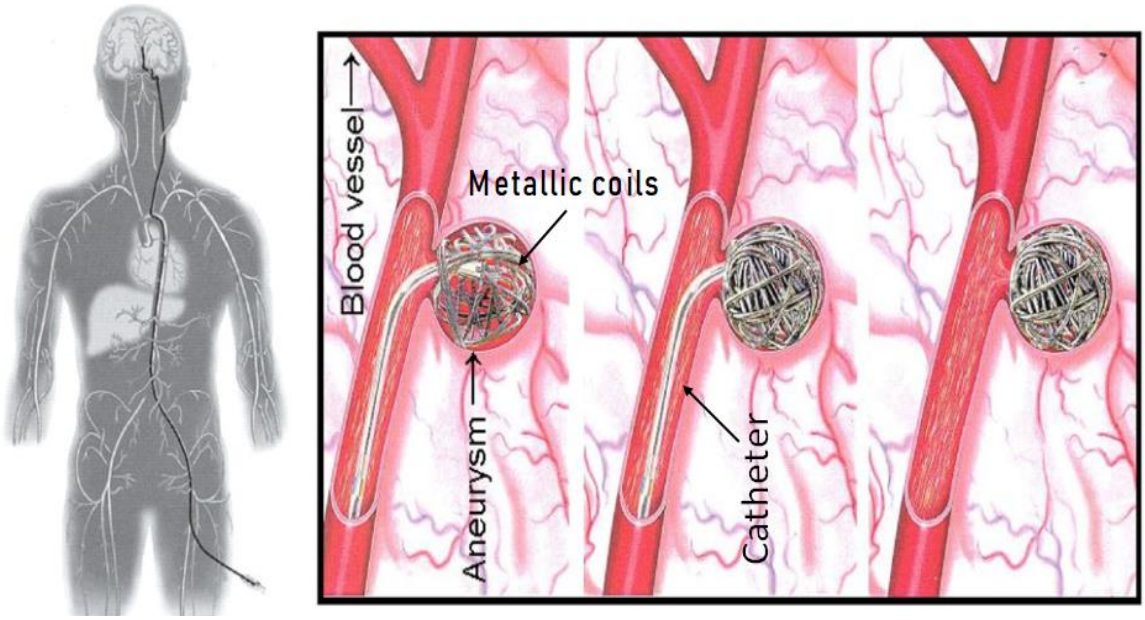

Fig. 1.8. Schematic demonstration of embolization of aneurysm with metallic coils. Reproduced with permission from Ref. [27]

Mechanical coils are one of the most commonly used embolic agents for the embolization of the aneurysm. They are permanent occlusion devices and were first used as an embolization agent by Gianturco *et al.* in the year 1975 [28]. The coil is delivered by pushing through a catheter, which is steered through the vasculature (starting from femoral artery) to reach the target vessel (for cerebral aneurysm) as shown in Fig. 1.8 [27]. On reaching the desired site, the coils are squeezed in the aneurysm sac or vessel lumen and the catheter is withdrawn. The coils reduce the blood flow to the malformations and provide a clotting surface for thrombosis. The coils are generally made of steel, platinum, tungsten, nitinol, etc. and their alloys. A platinum (92%)/tungsten (8%) alloy has become the basic material for most of the currently used coil designs [29]. The introduction of the Guglielmi detachable coils in 1995 increased the enthusiasm towards endovascular embolization of aneurysms. As the bare metallic coils have low thrombogenic characteristics, they have been attached with synthetic fibers of polymeric materials such as Dacron, Nylon, Polyester, wool, silk, polyvinyl alcohol (PVA), and Polyglycolic-Polylactic acid (PGLA) to promote quicker and increased thrombogenicity. There are different bioactive coils available in the market: (i) Matrix detachable coil (Stryker Neurovascular, CA, USA), (ii) Cerecyte coil (DuPuy Synthes, CA, USA), and (iii) Nexus coil (Microtherapeutics, Irvine, CA, USA), etc. HydroCoil Embolic system (MicroVention, Inc., CA, USA) is platinum coils coated with expendable hydrogels. When the coils come in contact with blood, it causes disentanglement of polymer chains of the hydrogel and then expands. The expansion of the coils potentially helps in increasing the packing density and volume filling for improvement of occlusion efficacy. These coils can expand up to 500% of their original diameters within 20 min of their implantation.

Detachable balloons were first used in 1974 for occlusion of large-vessels, cavernous carotid fistulas, and pulmonary AVMs. The Amplatzer Vascular Plug (AVP; St. Jude Medical, St. Paul, MN, USA) consists of a disk-shaped mesh of braided nitinol attached to

polytetrafluoroethylene coated delivery wire. The nitinol mesh of the AVP provides resistance to blood flow and surface for fibrin attachment aiding the clotting process. The different versions of AVP, which are being clinically used, are shown in Fig. 1.9 [30]. The AVP II is designed to reduce the time to occlude and to better conform to the blood vessels. The unique lobe shapes and additional layer(s) of dense nitinol mesh of the AVP III decreases the occlusion time, and the extended rims improve wall apposition. AVP III is ideal for high-flow situations. The multilayered, double-lobed design of AVP IV helps in rapid embolization and the flexible mesh enable delivery of the implant through tortuous anatomy with ease. Though AVP IV is a newer product, emerging data regarding its usage seems to be promising. Some of the advantages of using AVP are the ability to be repositioned, minimal migration of the plugs even in high flow situations. The AVP is mostly used in the embolization of large vessels such as the Pulmonary artery, Splenic artery, Aortoiliac segments, left coronary vein, etc.

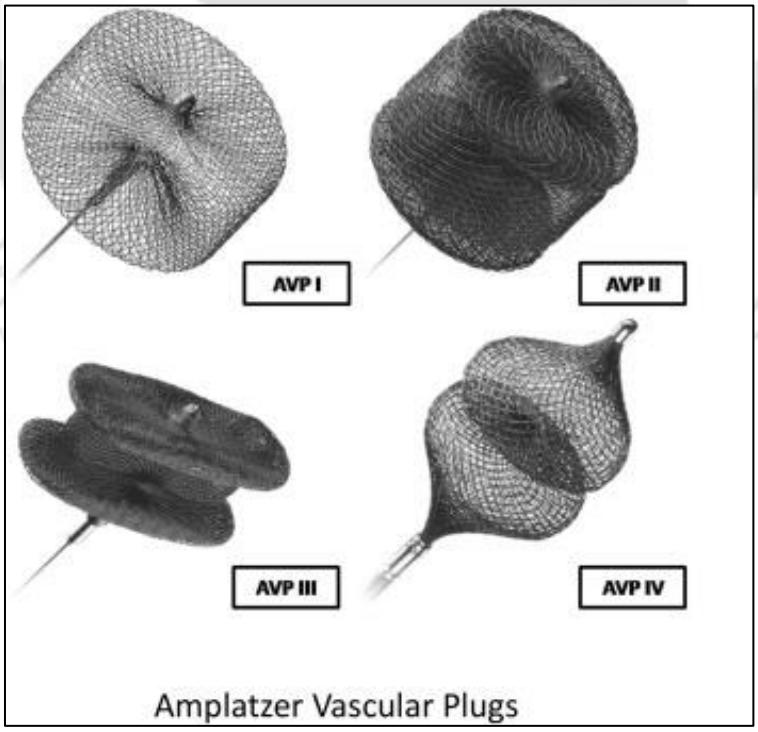

Fig 1.9. Family of Amplatzer vascular plugs. Reproduced with permission from Ref. [30]

1.4.2 Particulates

Particulates were the first embolic agents and are presently the most commonly used agents due to their versatile functionality. Initially, autologous embolic such as blood clots and muscle tissue were used for embolization. Blood clots modified with different materials such as thrombin, aminocaproic acid, oxidized cellulose, tantalum powder, etc., have been used as temporary embolic agents. Autologous muscle and subcutaneous tissue are considered as permanent embolic agents and are injected by suspending into saline solution. Due to the rapid development of other embolic agents, autologous embolic agents are rarely used in current clinical practice. The clinically used microparticles are either made of Polyvinyl alcohol (PVA) or Trisacrylic Gelatin. PVA is used in medical devices because of its biocompatible, non-toxic, non-carcinogenic, swelling properties, and bioadhesive characteristics [31]. They can be either irregularly shaped or calibrated, natural or synthetic, and permanent or biodegradable. Currently, micro sized embolic agents are commonly used for embolization of uterine arteries, bronchial arteries, external carotid artery branches, renal arteries, and in the preoperative embolization of primary bone tumors. A schematic representation of particulate embolic material blocking the blood flow into a uterine fibroid alongside the uterine arteries is shown in Fig. 1.10 [32]. Additionally, they can also be used for the management of epistaxis, benign or malignant liver neoplasms, arteriovenous malformations, and preoperative portal vein embolization [33]. The PVA particles promote occlusion by mechanical obstruction followed by thrombus formation and inflammatory reaction on the surrounding tissue leading to vessel remodeling. The currently used calibrated spherical microspheres are: (i) Bead Block (Boston Scientific, Marlborough, MA, USA), which is a PVA hydrogel-based microsphere containing acrylamido polyvinyl, and available in different sizes, (ii) DC Bead (Boston Scientific, MA, USA) is a spherical PVA based bead that can be loaded with chemotherapeutic agents (doxorubicin/ epirubicin/ irinotecan) to treat primary and metastatic liver cancer, and (iii) LC

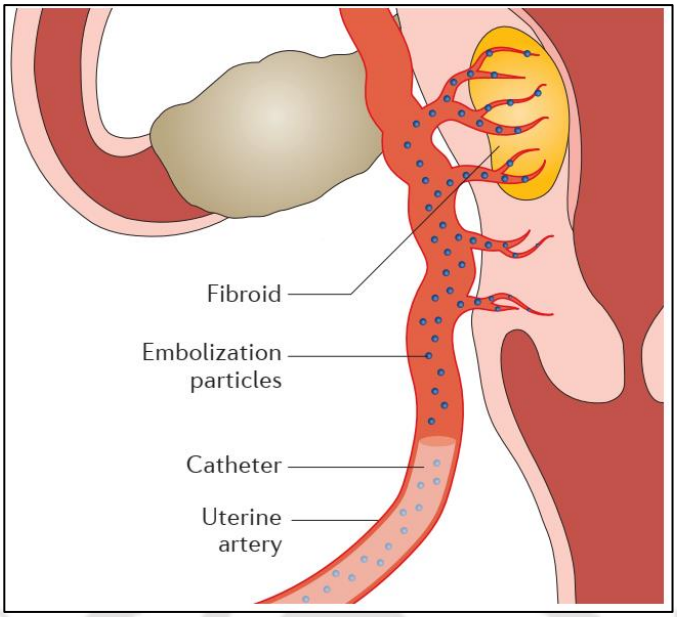

Fig. 1.10. Schematic representation of a particulate embolic agents used for blocking blood flow to the uterine fibroid. Reproduced withh permssion from Ref [32]

Bead (Boston Scientific, MA, USA) and LC Bead LUMI with intrinsic radiopacity (Boston Scientific, MA, USA) have been cleared by the FDA for the embolization of hyper vascularized tumors and AVMs.

Trisacryl gelatin microspheres, i.e. a tris-acrylic polymer matrix impregnated with porcine gelatin, are hydrophilic, compressible upto 20-30% of the initial diameter, nonbiodegradable, and have precise spherical shapes and smooth surfaces. EmboGold®, Embosphere®, (Merit Medical Systems Inc., South Jordan, UT, USA), are commercially available clinical microspheres. EmboGold® microspheres are impregnated with 2% elemental gold for visibility.

1.4.3. Liquid Embolic Agents

Liquid embolic agents are of interest to the interventional radiologist due to its capability to penetrate vessels, where coils and catheters cannot enter, which is demonstrated in Fig. 1.11 [34] . The microcatheter cannot reach the AVM nidus. However, the liquid embolic agents can flow to the targeted site and occlude the damaged blood vessel. Generally, the liquid embolic

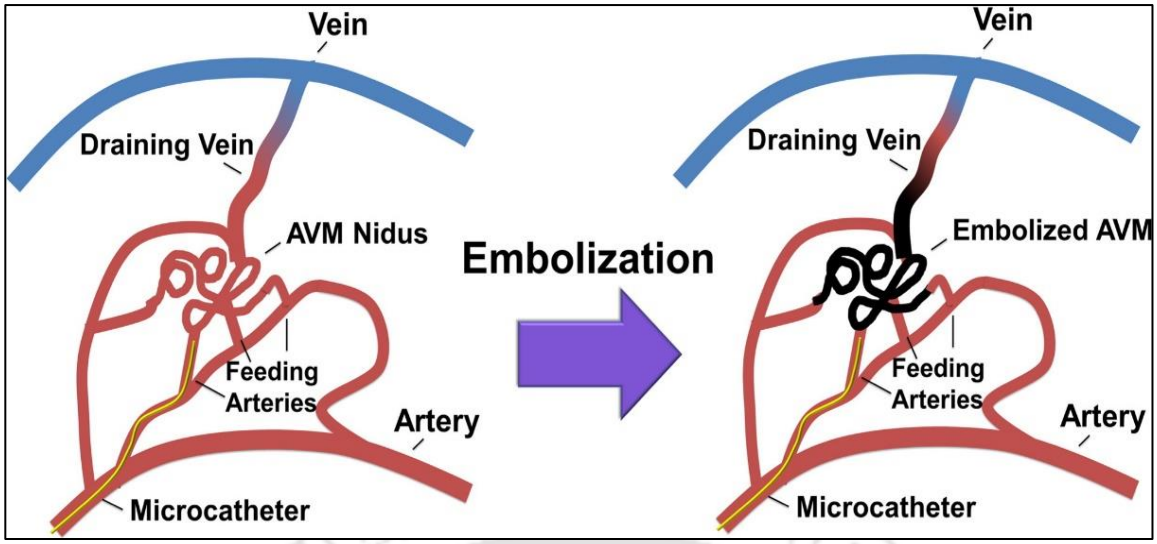

Fig 1.11. Schematic representation of liquid embolic agent occluding an AVM. Reproduced with permission from Ref [34]

agents undergo a phase transformation from liquid in the delivery system to a solid phase in the target. The low viscous liquid phase in the catheter/syringe helps in easier movement of the embolic agent, and the stiffer solid phase at the target site helps to achieve better occlusion. The phase transformation is achieved either by chemical cross-linking (polymerization) or physical cross-linking (ionic cross-linking/precipitation). The chemical cross-linking approach for phase transition is utilized by cyanoacrylates. They were accidentally discovered by Harry Coover in 1942 and later were marketed as “Super Glue” by Kodak in 1958 [35]. Cyanoacrylates rapidly polymerize when they come in contact with an anionic environment such as water or blood, as the monomers react with hydroxyl ions to form the long polymer chains. Medical grade cyanoacrylates were developed and used in the Vietnam War to close up wounds of the soldiers. N-butyl cyanoacrylates, octyl cyanoacrylates, and isobutyl cyanoacrylates are common tissue adhesives used as an alternative to standard wound closure, such as sutures, staplers, adhesive tapes for closing laceration, and surgical incisions. N-butyl-2 cyanoacrylate (NBCA) (e.g., TruFill (Cordis, Miami Lakes, FL, USA), and Glubran 2 (Gem, Lucca, Italy)) are being successfully used for endovascular embolization due to their excellent thrombogenicity, hemostatic properties, and adequate mechanical strength. Since

cyanoacrylates are not visible under fluoroscopy, lipiodol or tantalum is mixed with the cyanoacrylate to improve their radiopaque characteristics.

Other commercially available liquid embolic agents are Onyx (Medtronic plc, Dublin, Ireland) and Squid (Abmedica Deutschland GmbH & Co. KG, Germany), which consist of Ethylene Vinyl Alcohol (EVOH) dissolved in Dimethyl-sulfoxide (DMSO). The EVOH precipitates from the DMSO upon contact with blood and forms a permanent cast, which solidifies on the outer surface initially, and gradually hardens towards the core. Similar to NBCA, occlusion of the target area occurs by mechanical casting and is independent of thrombosis. The viscosity of the solution can be adjusted by varying the amount of EVOH dissolved in the DMSO. Higher viscosity is expected to offer better control during injection, whereas the lower viscosity allows for deeper penetration. The EVOH/DMSO solution is mixed with micron-sized tantalum powder (35% weight) to provide opacity under fluoroscopy.

Precipitating Hydrophobic Injectable Liquid (PHIL) (MicroVention, Aliso Viejo, CA, USA) is a newly developed liquid embolic agent working on the same principle as the EVOH system but with intrinsic radiopacity. It contains polylactide-co-glycolide and poly (hydroxyethyl methacrylate) dissolved in DMSO solvent. The radiopacity is achieved from the chemically bonded iodine component (tri-iodophenol), which removes the glare artifact on CT follow up [36]. Further, this negates the time required for mixing the contrast agent in Onyx preparation [37].

Sclerosing agents damage the endothelial cells and break blood proteins causing vessel wall necrosis. This results in acute thrombosis and fibrosis leading to embolization. It can include chemical irritants, detergents, osmotic agents, but the most commonly used agent for embolization is ethanol.

The above-discussed embolic agents have their own advantages and limitations. As discussed in the previous sections, aneurysms can be of different shapes and sizes and affect any blood vessel. Customized patient-specific embolic agents can overcome the issues with the presently used agents and will aid in proper occlusion of the aneurysm. Additive manufacturing can play a vital role in the fabrication of personalized embolic agents at an affordable cost and less time.

1.5 ADDITIVE MANUFACTURING (AM)

Another technology that has been greatly developed during the last decade is 3D printing or Additive Manufacturing (AM) technology. One of the major advantages of using additive manufacturing in medical sector is the ability to customize the products according to the patients' need at a fraction of time, cost and effort of conventional manufacturing process. Additive manufacturing has many applications and possibilities in clinical practices such as printing tissues and organoids, printing custom surgical instruments and prosthetics, 3D models for surgical preparation, etc., [38,39]. However, the use of AM for clinical cases is still at an initial stage.

Additive manufacturing has been called by many names such as 3D printing, Rapid prototyping, Direct digital manufacturing, and Layered manufacturing. Additive manufacturing is defined as "the process of joining materials to make objects from 3D model data, usually layer upon layer, as opposed to subtractive manufacturing methodologies" [40] . In additive manufacturing process, the design is converted into a 3D object with the help of computer aided design (CAD). The design is then sliced into several 2D layers/planes, and the 3D printer deposits each layer to form the desired object. The first 3D printer was developed by Charles W. Hull of 3-D Systems Corp in 1984 [41]. It was very expensive and not feasible to be used for commercial purposes. However, with the advancement and maturing of the

technology, 3D printers have become cheaper and captured the interest of the technology experts, industries, and the general public. As the technology has become more accessible to the people, many innovative and novel applications have been identified and new ideas are still being discovered. According to a report by Wohlers, the worldwide revenues from AM were $3.07 billion in 2013, and the industry is expected to exceed $21 billion by 2020 [42].

All 3D printers follow the same AM principles for creating the objects but different technologies are being used to build the layers. Some of the common techniques are (i) FFF Fused Filament Fabrication)/ FDM (Fused Deposition Modeling), (ii) SLS (Selective laser sintering), and (iii) SLA (Stereolithography apparatus). In FFF process, a thermoplastic polymer is extruded through a small nozzle on a platform to form the object. SLS technology joins materials such as plastic, metal, ceramic into the desired 3D shape by fusing the small particles by melting them with the help of a laser. Stereolithography uses a laser to cure photopolymer resin into the desired shape. The advantages of AM over traditional manufacturing are as follows [43]:

1) Rapid Prototyping: reduced processing time, and cost involved in developing new products
2) Customized unique parts: mass customization at low cost and quicker production of desired parts.
3) Small volume manufacturing: efficient for batch production.
4) Very Complex workpieces: production of complex and intricate designs at much lesser cost.
5) Rapid Manufacturing: direct manufacturing of finished parts.
6) Machine tool/ Component manufacturing: inexpensive tooling, avoid warehousing and reduces supply chain.

7) On-Site and On-demand manufacturing: eliminates transportation and reduces inventory costs.

The above advantages of AM make them a remarkable proposition for the medical sector, where the needs of every patient are different. The rapid prototyping and manufacturing of complex customized implants/devices in reduced time and cost propel AM as a definitive and disruptive technology for the healthcare industry. Healthcare experts can scan a patient and fabricate a custom implant or prosthetic that is specific to the patient's unique need using a CAD software. The custom-made implants will reduce the surgical time, cost and the risk of post-operative complications. Further, the required parts can be printed in remote locations which negates stockpiling and inventory shipping. The prosthetics/implants that would have taken many days to reach the patients could be made available in a matter of hours or a day. AM is also being used by surgeons to print 3D models of complex organ/organ systems to study, analyse and practise before attempting the real operation. Another notable feature of AM, which gained traction in the medical fraternity, is 3D bioprinting, i.e., the ability to print organs that can perform its specified functions. Three-dimensional organs can be created by depositing layers of living cells onto a gel medium and built into three-dimensional structures. 3-D bioprinting has been used for printing different types of tissue, including skin, bone, vascular grafts, heart tissues, other vital tissues, and organs. Thus, additive manufacturing has huge potential in the medical sector, and the benefit to the patients and healthcare professionals are plenty. The applications of AM are numerous but slowly progressing due to less communication between the healthcare professionals and engineers.

1.6 MOTIVATION OF THE PRESENT WORK

The annual incidence of aneurysmal subarachnoid hemorrhage (SAH) from a ruptured intracranial aneurysm is 6 to 16 per one lakh population, which estimates about 81,000 to

2,16,000 new cases per year in India [44]. Similarly, extrapolating 5 to 10 per one lakh population of Aortic aneurysm cases every year [45], it estimates about 67,500 to 1,35,000 cases per year in India. Also, the embolic agents are not produced indigenously and imported from other countries. Imported implants and medical devices are expensive and not suitable for Indian patients because of their design constraints. Thus, it is essential to develop indigenous devices at an affordable cost without compromising their functional activities. Further, the indigenously developed devices will not only be affordable but also better suit the needs of our countrymen and reduce the import dependency of our country. The present work is related to developing an indigenous implant/embolic agent for minimally invasive transcatheter embolization, i.e. deliberate occlusion of blood vessels with the aid of radiology imaging techniques. Occlusion or blocking of vasculature is required for diseases like Aneurysms, Arteriovenous malformations, pseudoaneurysms, and solid tumors. Further, a patient-specific embolic agent that will address the problems associated with the present embolic agents will be a blessing to the patients and the medical sector alike.

1.7 ORGANISATION OF THE THESIS

This thesis contains seven chapters. **Chapter 1** discusses the various aspects of biomedical devices, implants and the requirement of developing indigenous implants. A brief introduction to the various elements of this research work has been presented. It also contains the motivation behind the present work and the organization of the thesis.

Chapter 2 highlights the problems and issues with the presently used embolic agents based on the published literature. An assessment about the potential use of shape memory polymer (SMP) for endovascular embolization and the research work carried out by different groups in this regard have also been presented. A review on Fused filament fabrication (FFF) printing of SMP is done to evaluate the possibility of fabricating patient-specific embolic agents. Based

on these studies, it reports on the different technical gaps noticed from the available literature, and accordingly, the objectives of the proposed thesis work have been framed.

Chapter 3 contains a novel fabrication method developed to produce radiopaque, and patient-specific Shape memory polymer composite (SMPC). The fabrication procedure is explained in detail, and it is followed by material characterization of the developed SMPC to evaluate its suitability for the proposed application.

In **Chapter 4**, the nano Barium sulphate, nano Hydroxyapatite, and hybrid SMPCs have been prepared through compression molding technique and characterized to explore their suitability for endovascular embolization. The developed composites are characterized by various methods to judge the suitability of the SMPC as an embolic agent and the optimum concentration of fillers to be added to the SMP.

Chapter 5 includes the results obtained from biocompatibility test on the developed SMPC according to ISO 10993 and the quantification of fibrinogen and albumin adsorption by the SMPC.

Chapter 6 discusses about the porous, and 3D printed nano barium sulphate based SMPC, which is found to be suitable as an embolic agent obtained from chapter 4 & 5. The properties of the porous 3D printed barium sulphate SMPC is reported. In addition, the viability of the developed SMPC for minimally invasive procedure is checked in an *in vitro* model developed for this application.

Chapter 7 summarizes the overall work done and important findings of the present thesis work. Future scope of the work is also reported here.

INTENTIONALLY LEFT BLANK

CHAPTER 2: LITERATURE REVIEW

2.1 INTRODUCTION

In this section, the issues with the presently used embolic agents have been reported after reviewing the available literature. The viability of using shape memory polymers as an alternate embolic agent has also been elaborately studied. In addition, studies on 3D printing of SMPs have been reported. Based on the detailed studies, the technical gaps noticed from the available literature are summarized, and the objectives of the proposed thesis work are framed.

2.2 CHARACTERISTICS OF AN EMBOLIC IMPLANT

A number of embolization agents have been developed, which are either being clinically used or tested. The choice of the embolization agent for treating a specific condition depends on the clinical scenario and the goal of the embolization procedure. Many factors influence the choice of embolization agent such as [46]:

1) period of time for occlusion. The occlusion is to be temporary, i.e., for hours/weeks, or permanent?
2) size of the vessel. Is the size of the vessel large (arteries up to 1–2 cm diameter) or small (capillaries 5–10 µm diameter)?
3) functionality of the tissue. Should the occluded part be viable after embolization?

The primary role of an embolic agent is to stop the blood flow into a designated place, and successful embolization occurs when hemostasis is achieved. There are also many other characteristics that an ideal embolic agent should possess for safer, better, and easier application [47]:

1) definitive occlusion, i.e., it should occlude the desired vessel perfectly and prevent the blood flow into the desired area,

2) non-toxic, safe, and should not cause any undesirable effect on the neighbouring tissues,
3) affordable and easily available for the people,
4) should not fail and promote unintended recanalization of the blocked vessel,
5) easy to deliver and should not have any complications while being injected,
6) visible on common imaging devices (fluoroscopy, Computed tomography, etc.).

Several materials are currently being used for the embolization of blood vessels by interventional radiology techniques. These materials should possess the desirable characteristics that make them eligible for application as embolic agents for successful embolization. The material properties, which an embolic agent should possess for successfully fulfilling its application, are as follows [37]:

1) biocompatibility,
2) ease of delivery,
3) resistance to fragmentation/migration,
4) biodegradability (depending on application),
5) visibility and trackability on common imaging modalities such as fluoroscopy, magnetic resonance imaging (MRI), computed tomography (CT), or ultrasound, and
6) the ability to serve as a therapeutic (e.g., anticancer drug) delivery vehicle.

The clinically used embolic agents such as metallic coils, NBCA, Onyx, etc., are being successfully used in the different clinical scenarios. Generally, metallic coils are used for permanent occlusion of the diseased area, and the liquid embolic agents are used in occlusion of blood vessels with smaller diameter. However, these embolic agents have limitations, which have been discussed below in detail.

2.3 ISSUES WITH THE CLINICALLY USED EMBOLIC AGENTS

2.3.1 Mechanical Devices

The principal characteristics expected from the metallic endovascular coils are that they should be easily deliverable without any obstruction and should have intrinsic radiopacity. After implantation, the coils must withstand the blood pressure without collapsing, and the coils should maintain adequate packing density without exerting excessive force on the vasculature wall. Excellent mechanical strength and low-stress-relaxation behavior are critical for successful occlusion in the long term. Permanent occlusion and coil surface activation are desired to promote endothelium formation at the aneurysm neck, which prevents recanalization and rebleeding.

Leyon *et al.* [26] reported that the primary issues with endovascular coils are the complications associated with non-target embolization and coil migration resulting in pulmonary embolism, stroke, myocardial infarction, aneurysm regrowth, and rupture. Coil misplacement and coil vessel size disparity are the main reasons behind non-targeted embolization. Systemic migration of the small-sized coils has been reported in 2-6% of the cases [48]. The coils displace into the parent vessel if the coil size is too large, causing thrombosis in the non-target vessels. Also, an oversized coil can cause aneurysm rupture. Further, depending on the coil delivery technique, there is about 5% chance of the aneurysm perforation during endovascular coil embolization. In a review discussing about endovascular treatment in 1383 patients, aneurysm perforations were reported in 2.4% cases using controlled detachable coils and 4.7% cases using pushable coils [49]. Similar results were also reported by Cloft and Kallmes [50], where the risk of intraprocedural aneurysm perforation was found to be 4.1% in ruptured aneurysm. Recanalization of the aneurysm is another common complication observed while using coils and may require additional post-operative procedures.

Brinjikji *et al.* [51] observed that aneurysm regrowth, coil compaction, unstable thrombus formation, and lack of neointima formation at the aneurysm neck are some of the causes for recanalization. It has been observed that the recanalization rate depends on the packing density and aneurysm volume. A larger residual volume, i.e. difference between the volume of the inserted coils and the aneurysm volume, increases the recanalization risk. Occlusion of less than 50% of the aneurysm volume while using Guglielmi detachable coil (GDC) has also been reported [37].

Fibred coils were introduced to increase thrombogenicity; however, the fibres create difficulty during delivery due to the friction caused by rubbing on the catheter wall. Also, rapid thrombus formation increases the risk of its dislodging from the wire or aneurysm during the procedure. Initially, wool fibres were used with the coils for better occlusion, but it developed an intense chronic inflammatory reaction [52]. Dacron (polyester), Ivalon (poly(vinyl alcohol)), and silk fibres showed better biocompatibility than wool. Fiorella *et al.* [53] coated polyglycolic polylactic acid (PGPLA), a bioabsorbable polymer, on the bare coils to increase the occlusion rate by promoting cellular reaction, which helped in the formation of stable intra-aneurysmal scar tissue formation. Several clinical interventions have been done to study the efficacy of bioactive coils (Matrix detachable coil (Stryker Neurovascular, CA, USA) and Nexus coil (Microtherapeutics, CA, USA)) as compared to bare platinum coils (Guglielmi detachable coils, Stryker Neurovascular, CA, USA) in both short and long term. In a single-center study conducted by Rooij *et al*. [54], Nexus coils were used to treat 101 aneurysms and the results were compared with 120 aneurysms treated with Guglielmi detachable coils after a period of 6 months. They reported that 11.9% of the aneurysm treated with Nexus coils required additional coiling after 6 months compared to 13.3% in GDC. However, it was concluded that it was not statistically significant, and there was no evidence of any benefit of using PGPLA coated coils in recanalization of an aneurysm. A multicentre study was

conducted across Europe by Gory and Turjuman [55] involving 390 patients with 404 intracranial aneurysms, who were embolized with at least 75% of coil length as Nexus coils. They reported the recanalization in 17.7% of the cases after 13.3 months and came to a similar conclusion as the earlier study that Nexus coils did not demonstrate efficacy in aneurysm recanalization. Similarly, the long-term benefits of the HydroCoil Embolic system (MicroVention Inc., CA, USA) over bare platinum coils were found to be inconclusive in a multicentre study, where they reported that the overall recurrence rate was similar between aneurysm treated with GDC and the HydroCoil Embolic system [56,57]. Im *et al.* [58] reported that hydrogel coated coils may cause delayed aseptic meningitis (inflammation of the linings of the brain) and hydrocephalus (abnormal build-up of fluid deep within in the brain).

The detachable balloon is not currently approved by the FDA due to the risk of aneurysm rupture, migration, and deflation [59]. Wakhloo *et al.* [60] reported that a detached balloon could act as a ball valve within the aneurysm sac, leading to rapid refilling and rupture of aneurysm. In addition, inappropriate placement of the balloons in the aneurysm boundaries would rupture/deflate, resulting in non-target embolization and suboptimal aneurysm occlusion. In a single-center study done by Sluzewski *et al*. [61], thromboembolic events and intra-operative aneurysm rupture were observed in 9.8% and 4.0% of patients, respectively, while using balloon assisted coil embolization for ruptured and unruptured aneurysm. The issues with the Amplatzer Vascular Plug (AVP; St. Jude Medical, St. Paul, MN, USA) are difficulties in administering through complex and tortuous vessels and the requirement of large guiding catheters. The newer versions of AVP have better thrombosis characteristics than the earlier versions, but the issue remains. AVP is expensive compared with mechanical coils. Lopera [62] reported that relatively straight vessels with constant diameter are necessary for preventing plug detachment.

2.3.2 Particulates

The early practice of using autologous muscles and subcutaneous tissues in particulate form was popular because of their inherent biocompatibility and low cost. However, there were issues related to temporary recanalization, fragmentation, and migration of the clots. PVA was first used as an embolic agent during 1970's, when Tadavathy *et al.* [63] used IVALON® to embolize the hepatic artery and arteriovenous malformations of the spinal artery of their patients. Initially, the PVA microparticles were irregularly shaped and prepared from the mechanical fragmentation of the polymer, followed by sieving to segregate particles of different sizes. However, the embolization with the irregular-shaped particles was unpredictable due to their lack of size precision and irregular shape. These shortcomings led to the development of calibrated microspheres (Bead Block (Boston Scientific, MA, USA)), which are spherical-shaped microparticles within the specified range of diameters. PVA particle embolization has issues with recanalization, non-target embolization, duration of occlusion, and tissue ischemia [33,64]. When the particle size is decreased, the risk of complications is increased due to the greater penetration in the vascular bed. The selection of appropriately sized microparticles is important to prevent any unwanted complications. Further, PVA, like all polymers, is inherently not radiopaque. As such, PVA is prepared by mixing a dilute suspension of contrast agents for catheter injection. The contrast agents not only provide acceptable opacity but also help in decreasing the overall viscosity of the solution, resulting in decreasing the risk of microcatheter occlusion. Lu *et al.* [65] produced a radiopaque embolic agent by encapsulating lipiodol in PVA.

Subsequently, Trisacrylic gelatin microspheres (EmboGold®, Embosphere®, (Merit Medical Systems, Inc., South Jordan, UT, USA)) were developed, which showed better performance than PVA microparticles in regards to lesser particle agglomeration, fragmentation, and catheter occlusion [37]. However, the trisacryl gelatin microspheres have

issues related to sedimentation of the microsphere. In addition, Embosphere® contains porcine gelatin, which has been reported to cause allergic reactions to the people. It has also been reported that Embosphere® can cause unintended ischemia in some vessels or organs as they can penetrate more deeply compared to PVA [59].

2.3.3 Liquid Embolic Agents

The problems reported by the clinicians when using N-butyl-2 cyanoacrylate (NBCA) (TruFill (Cordis, Miami Lakes, FL), and Glubran 2 (Gem, Lucca, Italy)) are related to the difficulties experienced in delivering a precise quantity of NBCA due to its rapid polymerization [59]. The addition of the radiopaque materials changes the viscosity and the rate of polymerization of the NBCA. The random nature of polymerization may lead to non-target embolization. Furthermore, its adhesive properties led to adhesion with the catheter and vascular walls [66,67]. Pollack and White [68] reported that the patient also experiences acute and chronic inflammatory reactions due to the toxic byproducts and the exothermic polymerization.

The advantage of the EVOH/DMSO-based system such as Onyx (Micro Therapeutics, Inc., Irvine, CA, USA) and Squid (Abmedica Deutschland GmbH & Co. KG, Germany) over NBCA is non-adhesiveness, which decreases the probability of catheter adhering to the tissues. Velat *et al.* [69] reported that the handling of EVOH/DMSO was better, as it can be delivered in a more precise and controlled manner because of its relatively longer solidification time than NBCA. EVOH/DMSO has been successfully used for the treatment of large aortic aneurysms, controlling the bleeding in the pelvis, kidney, and mesenteric region, intracranial aneurysms, AVMs, and tumors [70,71]. However, one of the major issues is the sedimentation of the tantalum and insufficient radiopacity [69,72]. In addition to that Onyx is an expensive agent, and the specialized catheters, which are compatible with DMSO, are required for its delivery.

Furthermore, concerns have been raised about the toxicity of DMSO. Murayama *et al.* [73] suggested that the EVOH system is required to be delivered under the supervision of experts because a large volume of DMSO administered in a short period of time causes vasospasm (a sudden contraction of the muscular walls of an artery) and vascular toxicity. A recanalization rate of 36% in giant aneurysms has also been reported by Cekirge *et al.* [74].

The newly developed Precipitating Hydrophobic Injectable Liquid (PHIL) (MicroVention, Aliso Viejo, CA, USA) has intrinsic radiopacity from chemically bonded iodine to the copolymer, which prevents the problem of tantalum sedimentation faced in DMSO/EVOH systems, but it does not address the problems related to the use of DMSO as a solvent [75]. Absolute ethanol, a sclerosing agent is limited to the cases, where the chances of non-target embolization are unlikely due to its low viscosity. Other disadvantages of alcohol include lack of radiopacity and dilution by vascular fluids. Other common side effects are hemoglobinuria (excess hemoglobin in the urine), focal skin necrosis, and blister formation. An overdose of ethanol can also cause complications such as cardiac arrhythmias, respiratory depression, and seizures [26].

2.3.4 Future Requirements

As discussed above, many embolic agents are currently being used by the medical fraternity. Each one of them has its specific abilities, advantages, and limitations. An embolic agent addressing the present issues would be beneficial to both the patients and doctors. A metallic coil that is rigid during the delivery but replicates the mechanical properties of blood vessels under *in vivo* conditions and having the desired surface properties for facilitating thrombosis will improve its performance. The performance of particulate embolic agents can be improved by controlling their flow characteristics with effortless movement in the catheter and predictable movement in the vasculature. The NBCA with a longer polymerization rate, lesser

adhesiveness, and cleaner polymerization will decrease the difficulties associated with it. The precipitating embolic agents without the toxic solvent DMSO and better radiopacity will improve the rate of successful embolization. However, these are physical and inherent material characteristics of the embolic agents, and substituting them from a tiny pool of biomaterials is an improbable task. As such, researchers are working on new biomaterials that have better performance and negate the issues with the currently used embolic agents. Further, the medical device field is governed by stringent approval regulations creating a hindrance in introducing new implantable medical devices to the market. Therefore, the introduction of more promising substitutes from traditionally used materials or improving the design of the presently established device is viable and easier to bring the devices to the market.

2.4 SHAPE MEMORY POLYMER AS EMBOLIC AGENT

Based on the above discussed requirements, shape memory polymers are found to have a great potential to be used as an alternative embolization material for the treatment of aneurysms and occluding the targeted blood vessels. They are relatively new and exciting products, and their properties make them a suitable material for use as an embolic agent.

2.4.1 Shape Memory Polymer

Shape memory polymer (SMP) based products have found a great interest in recent times for technological innovations, and the researchers are continuously exploring new avenues for their applications in textile, medical devices, aerospace, electronics, etc. SMP is a smart material that can recover its permanent shape on the application of external stimuli such as light, temperature, moisture, magnetic, or electric field after being held in a stable temporary shape. This phenomenon of SMP and its foams has made them as a potential candidate for an embolic agent in interventional radiology techniques [76–79]. The shape memory effect of the SMP has the inherent advantages of being able to be sent through a catheter in a compressed

temporary shape (smaller footprint/small diameter wire), which will be activated to their primary shape (larger footprint/complicated shape) at the targeted site. The stimuli for the transition can be body temperature or other sources. SMP has become a popular choice because of its numerous other advantages, such as lightweight, significant shape recovery of up to 400% plastic strain, nontoxicity, non-mutagenicity, ease of processing, and inexpensive, which make them as a preferable choice compared to shape memory alloys. Furthermore, the ease in tailoring the characteristics of SMP and its biocompatibility makes it as an exciting material.

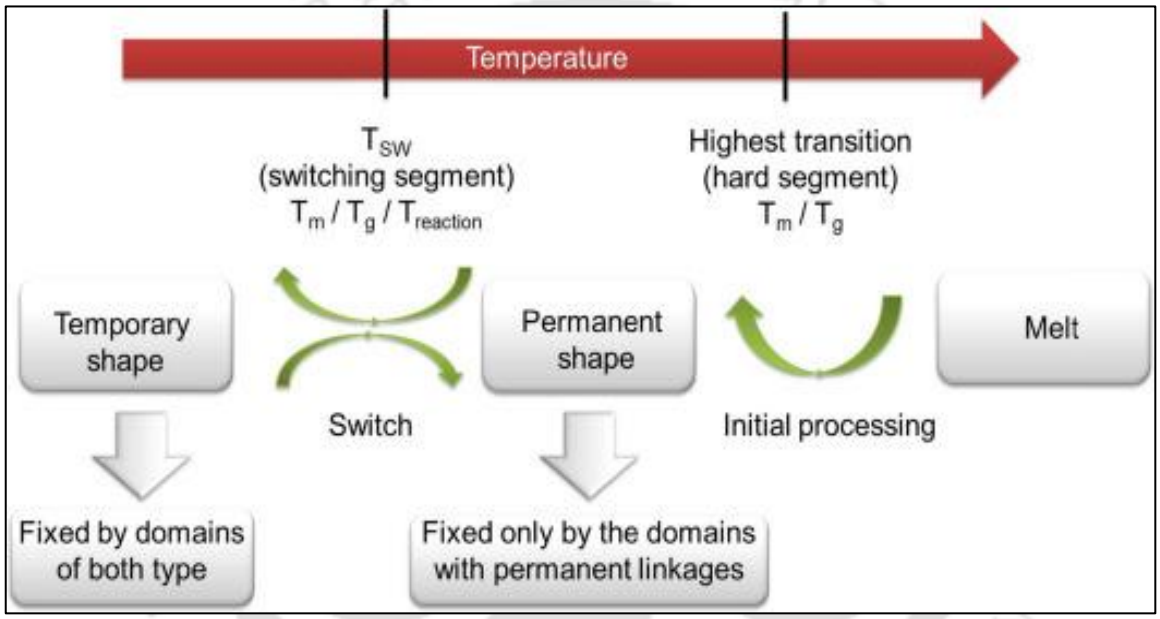

Fig. 2.1. Schematic representation of the basic principle of the shape-memory effect in polymers. Reprinted with permission from [80]

The shape memory effect of the SMP is not an inherent property; that is, polymers do not display the said effect naturally. Shape memory effect results from the combination of polymer structure and processing. The schematic representation of the steps behind the shape memory effect is represented in Fig. 2.1. During the initial processing of the SMP, the permanent/ original shape of the polymeric product is fabricated. The secondary/temporary shape is programmed by heating the SMP above its switching temperature (T_{sw}), then deforming it to the required shape and cooling it below T_{sw} as shown in Fig. 2.1. The temporary shape will be retained by the SMP until it is stored below its T_{sw}. On heating the same above the T_{sw}, the

SMP will recover to its permanent shape. SMP possesses a complex 3D molecular structure, which is the outcome of numerous cross-linking net points and switching segments. The required shape-memory phenomenon is achieved by tailoring two components in the SMP structure: firstly, the net points or the hard segments which determine the permanent shape, and secondly, the switching segments or soft segments with a suitable switching temperature (T_{sw}) are responsible for the shape fixity or temporary shape. The hard segments are formed by chemical cross-linking, crystalline phase, and molecule entanglement and interpenetrated network while the switching segments are formed during the crystallization/melting transition, vitrification/glass transition, liquid crystal anisotropic/isotropic transition, reversible molecule cross-linking and supramolecular association/dissociation. Thermally activated SMP is the most common type, where the shape transition is triggered by an increase in temperature. The T_{sw} of a thermally activated SMP can be adjusted by tailoring its chemical composition and structure.

The shape memory effect of the SMP is an entropic phenomenon, as discussed by Xie [81]. In its permanent shape, the molecular chains of the SMP are in a thermodynamically stable state, i.e., highest entropy. When the SMP is heated above the T_{sw}, the chain mobility is increased, and on application of the deformation load, the polymer chain conformations are easily changed, leading to lower entropy state and change in macroscopic shape. Subsequently, the temporary shape of the polymer will be fixed by cooling the polymer below its switching temperature (T_{sw}), which freezes the molecular chain arrangements, resulting in macroscopic shape fixation. When the heat is applied to the SMP to reach the temperature above its T_{sw}, the mobility of polymer chain is re-activated, allowing the SMP to recover its permanent shape.

Shape memory polymers can be of different polymers such as poly (e-caprolactones), polyurethane, polyethersulfone, Poly (DL-lactide-co-caprolactone), etc. However, for application in human, a proven biomaterial, which is already being used for the targeted

application/site, decreases the probability of problems and makes it easier to get an approval and bring it to the market. As such, polyurethane becomes a suitable candidate for an embolic agent due to its low cytotoxicity, low thrombogenicity, low platelet activation, low cytokine activation, and low *in vivo* inflammatory response. Polyurethane has been used for a long time for making cardiovascular components such as intra-aortic balloons, blood sacs for ventricular assist devices, catheters, pacemakers, etc. Polyurethane is formed by reacting a polyol (an alcohol with more than two reactive hydroxyl groups/molecules) with a diisocyanate or a polymeric isocyanate in the presence of suitable catalysts and additives. Since a variety of diisocyanate and a wide range of polyols can be used to produce polyurethane, a broad spectrum of tailored materials can be prepared to meet the requirements of specific applications. A detailed review of the research being carried out on polyurethane-based SMPs for application in embolization has been reported in the following section.

2.4.2 Shape Memory Polyurethane (SMPU) and its Foams for Endovascular Embolization

The initial idea of using SMP for biomedical applications can be credited to Lendlein and Langer [82], who developed a smart suture and successfully implanted it in a rat without any complications. Metcalfe *et al.* [83] used a commercially available cold hibernated elastic memory (CHEM) polyurethane-based foams (Mitsubishi Heavy Industry and Jet Propulsion Laboratory, California Institute of Technology, Pasadena, CA) for embolization of experimental canine aneurysms. It is reported that CHEM polyurethane is non-toxic, and non-mutagenic. It also has poor thrombogenic characteristics, and it could be used as a material for endovascular application. Furthermore, the porous foam permits cellular invasion and secondary neointima formation, which helped in sealing the aneurysm neck. They recommended embolic agents that could completely fill the aneurysm sac rather than the

embolic agents, which depended on thrombus formation for occlusion to reduce the chances of recanalization. This work is further continued by De Nardo *et al.* [84], where they tested the effect of sterilization on the morphological, thermomechanical, and cytotoxicity characteristics of CHEM 3520 and CHEM 5520 foam. They concluded that CHEM foams showed a high possibility of using them as aneurysm fillers due to their good cytotoxicity response, cell proliferation, and high shape recovery. Porous structure in SMPU is created by different techniques such as co-extrusion with chemical blowing agents and salt co-extrusion/particulate leaching (NaCl) in Calo-MER 48™ (Polymer Technology Group, Berkeley, CA, USA), solvent casting/particulate leaching (gelatin microspheres) in MM4520 (Mitsubishi H.I. Ltd, Japan) and compared with CHEM 3520 and CHEM 5520 [85]. The porosity was observed to be varied between 23% to 78%, where a wide range of sizes, dimension, distribution, and interconnection of pores are observed. It is also reported that the porous structure of the foam aided in shape recovery.

A research group headed by Maitland working on SMP for embolization developed a non-commercial ultra-low density and highly cross-linked biocompatible SMPU foam [86]. The foam showed the glassy storage modulus of 200–300 kPa, excellent shape recovery of 97%–98%, and up to 70 times volume expansion. To reduce the effect of moisture on the switching temperature of the above SMPU foam, the 1,6-diisocyanatohexane (HDI) is replaced with more hydrophobic 1,6-diisocyanatotrimethyl hexane, 2,2,4- and 2,4,4- mixture (TMHDI). The addition of TMHDI increased the switching temperature and decreased the shape recovery effect [87]. The SMPU is implanted on a porcine vein pouch aneurysm model, where the initial pathological results after 90 days demonstrated the possibility of using this SMPU for clinical application [88]. An amorphous, biodegradable, covalently cross-linked polymer based on polycaprolactone triol (PCL-t) is developed by Singhal *et al.* [76], which had the shape recovery in the range of 91%-99% and a low density of 0.20-0.093 g cm^{-3}. The degradation

rate of the foam is increased with the PCL-t content and hydrophilicity. An SMP implant consisting of two SMPU foam layers is developed by Hwang et al. [89], where (i) inner SMPU foam layer had lower density and higher volumetric expansion [86], and (ii) the outer layer contained 4 vol% Tungsten to increase its radiopacity but reduced its volumetric expansion [90]. The SMPU foam implanted in an aneurysm in a porcine model showed a better healing in comparison to that of the 2D helical shape (GDC®, Stryker Neurovascular) after 90 days of implantation [91]. However, a conclusive remark is not reported due to the smaller sample size, but the results encouraged a wider and longer study. Another issue was the incompatibility of the implant device to be delivered with the standard microcatheters and the requirement of an external heating device to actuate the foams. Similarly, SMPU foam coated coils showed a good potential for aneurysm treatment. It is reported that it promoted more complete healing of the dome and neck of the aneurysm in comparison to bare platinum coils on the rabbit elastase model. However, a higher rate of recanalization is observed in foam coated coils, which was hypothesized due to sub-optimal packing and accelerated degradation of the SMPU foam [92]. A laser actuated SMPU stent-foam device is demonstrated for endovascular embolization of non-necked fusiform aneurysms, which could embolize the aneurysm and maintain an open lumen in the artery. The occlusion of a fusiform aneurysm is quite difficult due to its wide neck. Thus, filling the same using an embolic agent is cumbersome. The thermally actuated SMPU foam in the device is heated by a laser, where an absorbing dye (Epolight 4121, Epolin, Inc., Newark, New Jersey) is mixed to increase its light absorption capacity. However, the use of a powerful laser is unsuitable due to its impact on the blood vessels, and in addition, the SMPU stent and foam are not radiopaque [78].

A critical factor in the feasibility of SMPU foams as an embolic agent is the pressure exerted by the SMPU foam on the aneurysm wall during expansion. Ortega et al. reported that the wall strength of an aneurysm is in the range of 0.73–5 MPa, which is sufficient enough to withstand

the pressure generated from SMP foam expansion [93]. Hwang *et al.* [94] concluded with the help of finite element model simulation that SMP foam samples having 1.5–2 times the size of an aneurysm could be safely implanted in the aneurysm without risk of rupture, thereby providing a high packing volume during the treatment. However, an oversized SMP foam may protrude into the vessel lumen.

2.4.3 Radiopaque Shape Memory Polyurethane (SMPU) and its Foam Composites

A polymer in its pure form is not suitable as an embolic agent for interventional radiology techniques due to its lack of inherent radiopacity. A radiopaque SMP makes it easier to deliver under fluoroscopy and later track it post-implantation. Researchers have proposed new SMP composites to be used in interventional radiology techniques by adding high-density radiopaque biomaterials such as barium sulphate, tantalum, and tungsten, etc. In an initial study by Hampikian *et al*. [95], 3 vol% (50 wt%) tantalum is used as a radiopaque filler in a commercially available SMPU, Calomer™ as embolic coils, and the composite coils are successfully tested as an alternative to metallic coils in an artificial aneurysm model. The shape memory polymer composite (SMPC) is fabricated by the extrusion process, and the addition of the filler made the composite opaque even at a material thickness of 0.088 mm under the clinical fluoroscopic X-ray. The T_g of the SMPC is decreased by 3 ℃, and the maximum recovery stress is decreased by 33% in comparison to that of unfilled SMPU. It is also hypothesized that the particle size played a role in the radiopacity. The radiopacity of SMPU foam is increased by adding tungsten at different concentration of 0.5,1, and 4 vol% by Rodriguez *et al.* [90]. It is observed that 4 vol.% tungsten powder in SMPU foams was visible under X ray at a minimum thickness of 2 mm, and it is increased to 8 mm, when SMPU foams are superimposed with the skull and tissues. In general, the visibility is increased with thickness of test sample and concentration of tungsten. The Young's modulus and tensile strength are

increased by 43% and 67%, respectively, at 4 vol% composite foam. Complete healing of the aneurysm site in a porcine model after 90 days and the lack of inflammation were indicative of the biocompatibility of the tungsten-dispersed SMPU foam.

Barium sulphate is a medically approved contrast material for diagnostic radiographic examinations, and it is already being used in catheters as radiopaque agents in interventional radiology, Christoph Miethke GmbH & Co. KG. It has been reported by Ricker and Weber [96] that 10 wt% filled nano barium sulphate (80-500 nm) in the polymethyl methacrylate (PMMA) matrix had about 23% better radiopacity in comparison to micro barium sulphate (2 µm). Polyurethane nanocomposites with 1 wt% nano-sized barium sulfate spherical particles and fibers are prepared by Romero-Ibarra *et al.* [97] via melt extrusion process. It is reported that the nanoparticles did not influence the mechanical properties, and the nanocomposite did not have any qualitative difference in the radiopacity level compared to conventional composites. Nano barium sulphate (73 nm) enhanced antimicrobial characteristics, and it provided better radiopacity in comparison to that of micron-sized Barium sulphate (7 µm) for the same concentration of 40 wt% as reported by Aninwene II *et al.* [98]. It has been reported that shape recovery of 21.8 wt% barium sulphate (3µm) SMPU composite is varied in the range of 91-95%, which depends on the programming temperature and it played an important part in the shape memory characteristics of the composite [99]. A study is conducted by Weems *et al*. [100] to compare the effect of adding different types of radiopaque materials, $BaSO_4$, W, and ZnO_2 to SMPU foams with the concentration of 1 and 4 vol%. Barium sulphate filled SMPU foams on an average showed an 8% increase in strain recovery in comparison to that of tungsten filled SMPU foams at the same concentration. The addition of the radiopaque materials increased the radiopacity, and 4 vol% of $BaSO_4$, W, and ZnO_2 provided higher opacity than the standard GDC. The shape recovery and recovery time of SMPU foams are decreased with the addition of these fillers. Tungsten nanoparticles (40-60 nm) at 4 to 11vol% are added to the

pre-polymer during the synthesis process of the SMPU foam to produce the foams with inherent radiopacity [101]. The dispersion of filler is found to be improved in case of nanoparticles compared to microparticles and the foam visibility under fluoroscopy beyond 6 vol% W content is observed to be better than the GDC control. However, the addition of the filler decreased the mechanical strength, volume recovery, and increased actuation time of the SMPC.

From the above discussion, it is noted that SMPU makes a very strong case as an embolic agent for aneurysms. Different research groups have been working on improving and tuning the characteristics of SMPU and SMPU based devices for applications in minimally invasive surgeries. However, none of the SMP based medical device as an embolic agent has been approved for clinical applications in human beings. Human trials are being conducted on Impede, Impede-Fx Embolization plugs [92], and TrelliX Embolic Coil [79] (Shape Memory Medical Inc., Santa Clara, USA). The above devices use marker bands to increase their radiopacity, but the foam used in the above devices is not radiopaque. In an unfortunate circumstance of the foam detaching from the marker and migrating to other parts, the tracking of the detached part would be very difficult. In addition, the exact shape, contour, and expansion behaviour of the foam are not visible under fluoroscopy, creating uncertainty of proper occlusion.

It has been already established that patient-specific implants are better for improving the safety and cure. Custom embolic implants in the shape of aneurysms, organs, or the vasculature recreated from the X-rays, CT scans, or MRI will decrease the risk associated with embolization. They will help in complete occlusion of the aneurysms, organs, etc. and decrease the chances of recanalization. The probability of bursting of the aneurysm and bulging of the embolic agent into the vessel lumen are also expected to decrease. Thus, the embolic implants obtained by a 3D printing technique are desirable under the above circumstances to overcome

the currently faced problems by the medical fraternity. The proposed manufacturing technique is the quickest, cost-effective, and sustainable way of fabricating patient specific implants.

2.5 ADDITIVE MANUFACTURING OF SHAPE MEMORY POLYMER BASED PRODUCTS: 4D PRINTING

4D printing is coined by Skylar Tibbits to define 3D printed objects that would shift their shape over time. The 4th dimension is indicative of the shape-changing characteristic of the printed object over time. 4D printing has been popularly defined as "the shape, property, and functionality of a 3D printed structure could evolve with time when it is exposed to a predetermined stimulus, such as heat, water, light, pH, etc." [102]. 4D printing is a new research area, and its progress has been limited due to the lack of 3D printable functional materials. Currently, shape memory polymers, shape shifting polymers, and hydrogels are being investigated. In biomedical applications, 4D printing can be beneficial in different areas such as medical diagnosis, medical device fabrication, tissue regeneration, and drug delivery. SMP based products have been manufactured by different 3D printing techniques such as photopolymer inkjet (polyjet) [103,104], projection stereolithography (SLA) [104], fused filament fabrication (FFF)/ fused deposition modelling (FDM) [105,106] and selective laser sintering (SLS) [107].

A schematic representation of different 3D printing techniques is shown in Fig. 2.2 [108]. In SLA, as shown in Fig. 2.2 (i), a photopolymer in a tank is selectively polymerized with the help of a laser to fabricate the parts. In Inkjet printing, the photopolymer is injected through an inkjet head and subsequently polymerized with UV rays to get a part, and it is shown in Fig. 2.2 (ii). The metal/plastic powder is rolled over a build platform and a laser is used to fuse the powder together in SLS technique, as shown in Fig. 2.2 (iii). A thermoplastic filament is extruded through a nozzle and each layer is deposited over the other in FDM/ FFF, as shown

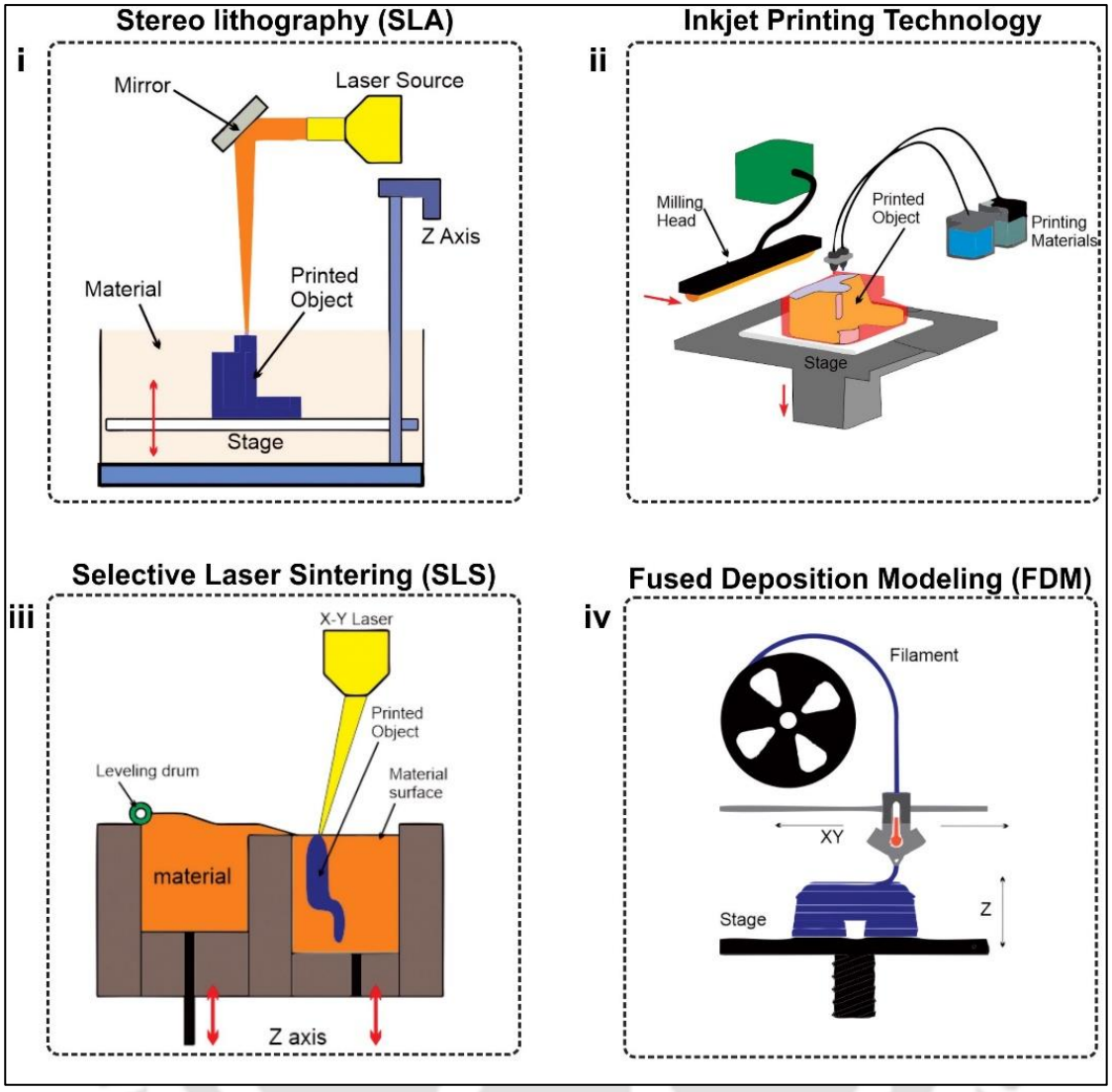

Fig. 2.2. 3D Printing techniques used for fabricating SMP: (i) Stereolithography (SLA), (ii) Inkjet printing, (iii) Selective laser sintering (SLS), (iv) Fused Deposition modelling (FDM). Reprinted with permission from [108].

in Fig. 2.2 (iv). The low cost, high reliability, availability, and simple operation of the FFF 3D printers make them an appropriate and attractive technical tool to fabricate the customized self-deployable embolic materials. The FFF and SLA 3D printing technologies can be used for printing the patient-specific embolic agents because of their wide availability, easier operation, and cheaper alternative than other 3D printing technologies. The major difference between these technologies is that FFF is used for thermoplastic polymers, while the SLA is used for thermosetting polymers. Thermosetting polymers are chemically cross-linked polymers and

have a less strain to failure, which will hamper its applications in minimally invasive surgeries. Thus, the most viable method for the fabrication of porous and patient-specific implants is the FFF. Fused filament fabrication (FFF) or Fused Deposition Modelling (FDM) is a material extrusion-based 3D printing technology for thermoplastic materials, where the products are fabricated by extruding the polymer filament through a hot nozzle and printing a layer over another layer to get the final models. In this section, FFF printing of SMPU has been reviewed because of its inherent advantages.

Commercially available thermoplastic polyurethane SMP MM-4520 (SMP Technologies Inc., Japan) has been successfully fabricated by the FFF process in 2015 [109,110]. The MM-4520 pellets are extruded into filaments of 1.75mm diameter and printed using commercial FFF 3D printers. The annealing or post-heating of the fabricated parts below the melting temperature increased the shape recovery and the mechanical properties of the SMPU. Thermally actuated SMPU is mixed with carbon black (CB) to make it photo responsive composite [111]. SMPU and 10wt% CB are mixed and extruded to produce a SMPU-CB composite of 1.75mm diameter filament and 3D printed by FFF to produce parts that are actuated by light. All the above-discussed works are focused on solid SMPU; however, the advantages of porous structure in biomedical applications are plenty. Due to the inherent limitation of the FFF process, creating shapes below 100-200μm thickness is difficult; as such, creating a porous structure below that resolution is not possible. To create a porous structure below 100 μm, FDM/FFF has to be combined with other compatible pore-forming techniques [112]. Porous PLA foam is fabricated using FDM/FFF and gas foaming technique, where the former is used to create macroporosity in the scaffold, and the latter is used to make the microporosity (1–10 μm). Mu *et al.* [113] printed porous photo-curable resin with a custom-made digital light processing (DLP) and salt leaching technique. Shim and Kim [114] fabricated porous scaffolds by combining salt leaching and polymer deposition system.

According to our review, there are a very few works on the 4D printing of polyurethane composites. Porous and radiopaque SMPU, which can be custom printed according to patients' requirements, has not yet been developed. From the above discussion, it can be summarized that there is still a requirement of radiopaque embolic agents that can overcome the limitations of the currently available materials and occlude a targeted site successfully, safely, and completely. SMPU is one of the leading potential candidates as it can change its shape and has a wide range of mechanical properties. The solid embolic agents need to be stiff while being sent through the catheter and soft like the targeted tissue after the implantation for better integration within the animal/human subject. Though many biocompatible polymers can be used, polyurethane is favorable because it is a proven material being clinically used in implants which are in contact with blood. The customized patient-specific embolic agents that can be fabricated in any complex shape and geometry are expected to decrease the morbidity and mortality. After comprehensive studies on the SMPU composites from the published literature, the following technical gaps are noticed.

2.6 TECHNICAL GAP

The technical gaps present in the above field of research are summarised below based on the detailed literature survey:

1) A fabrication process for developing a patient-specific porous SMP for embolization has not yet been developed.

2) Only a limited SMP composites have been developed for biomedical applications, which can be fabricated by the 3D printing process.

3) The absence of 3D printable radiopaque and porous SMP composites limited the number of options of embolic agents in minimally invasive surgeries.

4) The effect of different fillers on the improvement of radiopacity of 3D printable polymer and their influence on the shape memory effect have not been studied in detail.

5) Parametric studies and the optimal concentration of radiopaque fillers in 3D printed polymers to obtain the fluoroscopic images as per the standard procedure have not yet been reported.

6) The effects of concentration, morphology, type, and size of the filler, and the processing technique followed on the structure and material characteristics (mechanical and thermal) of the SMP are yet to be studied adequately.

7) Effects on programming temperature, recovery stress, recovery rate, and recovery time at body temperature due to the addition of filler in SMP are yet to be focussed.

8) The viability of using a patient-specific radiopaque embolic agent under *in vitro* and *in vivo* conditions has not been explored.

9) Studies on the influence of sterilization on the mechanical and shape memory characteristics of 3D printed SMP polymer, and its composites are not reported.

2.7 OBJECTIVES

The main objective of the present work is to develop a solid embolic medical device for the treatment of aneurysm, which can be accomplished by the following sub-objectives:

1) To develop a suitable manufacturing process for fabricating the porous shape memory polymer-based composites using a 3D printing technique.

2) To develop the radiopaque 3D printable shape memory polyurethane composites.

3) To study the effect of dispersing the radiopaque fillers on the mechanical properties, thermal properties, and the shape memory effect of the shape memory polyurethane.

4) Initial biocompatibility studies on the shape memory polyurethane composites following the ISO 10993 (Biological evaluation of medical devices) in order to explore the same for the proposed applications.

5) To study the viability of shape memory polyurethane composites for the proposed application in a lab-scale model under *in vitro* conditions.

INTENTIONALLY LEFT BLANK

CHAPTER 3: A 3D PRINTING TECHNIQUE FOR FABRICATING THE POROUS SHAPE MEMORY POLYURETHANE COMPOSITES

3.1 INTRODUCTION

In this chapter, a novel method of combining extrusion, Fused Filament Fabrication (FFF) technique, and salt leaching method has been proposed to print the patient-specific porous polymeric components. Tungsten is used as a radiopaque agent for providing the radiopacity required for visualization under the X-ray fluoroscopy for minimally invasive surgeries. The effect of adding a radiopaque filler on the characteristics of the test material has also been discussed.

3.2 MATERIALS

3.2.1 Shape Memory Polyurethane (SMPU)

Table 3.1. Properties of MM3520 [115]

	MM3520		
	units	Glassy	Rubbery
Hardness	H_DD	77	30
100%Modulus	MPa		2.3
Tensile Strength	MPa	51	10
Elongation	%	30 - 50	>600
Specific Gravity		1.25	
Glass Transition temperature, Tg	℃	35	

A semi crystalline ester-based shape memory polyurethane (SMPU), MM3520 (M/s SMP Technologies Inc., Tokyo, Japan) having the T_g of 35 °C in pellet form is used in this study.

The above SMPU is chosen because it is a thermoplastic polyurethane, which can be 3D printed, and has a switching temperature (T_{sw}) near the body temperature. A higher number of polymer chains will be triggered at body temperature in MM3520, which will improve the shape recovery, and it also negates the requirement of external stimulus for complete actuation. The data provided by the manufacturer of the SMP MM3520 is given in Table 3.1 [115].

3.2.2 Porogen

Sodium chloride (NaCl) (99.5% purity, 2.16g/cm^3) is procured from M/s Avantor Performance Materials India Ltd, Gurgaon, India, and it is used as a sacrificial element for pore formation. The commonly used nozzle diameter in FFF is 400 μm, and the FFF process has dimensional tolerance of 200 μm. Hence, the salt is ball milled to keep its size less than 180 μm. Though different porogens are available, salt is chosen as it is biocompatible and it has been used extensively for generating pores in medical implants [116].

3.2.3 Radiopaque Agent

Tungsten powder (purity>99.9%, 0.6-1 μm, 19.3 g/cm^3) is procured from M/s Sigma Aldrich, Bangalore, India and is used as a radiopaque agent to the polymer. Tungsten is being clinically used to enhance the radiopacity of cyanoacrylates for endovascular embolization [117] and thus, it is chosen as the radiopaque agent in this work.

3.3 METHOD

A novel method is proposed for fabricating a porous 3D printed composite product, which consists of extrusion, fused filament fabrication (FFF), and salt leaching. The schematic representation of the process is shown in Fig. 3.1. The polymer pellets, porogen, and fillers are mixed together to disperse the material homogeneously. This mixture is put into an extruder to ensure proper mixing and produce the filaments of the polymer composites. This filament is

used in the FFF printer to fabricate the required product. Finally, the porogen is leached out of the product to produce the porous custom-shaped composite product. The finer details of the process are discussed below in detail:

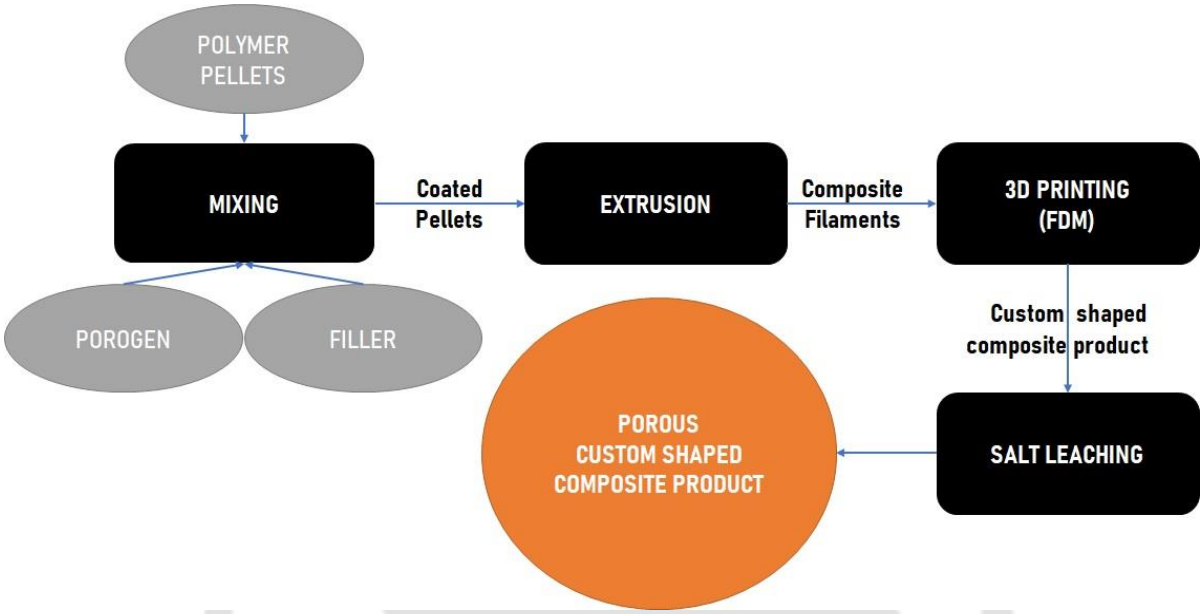

Fig. 3.1. Schematic representation of the novel fabrication process to obtain the 3D printed composite products

3.3.1 Mixing process

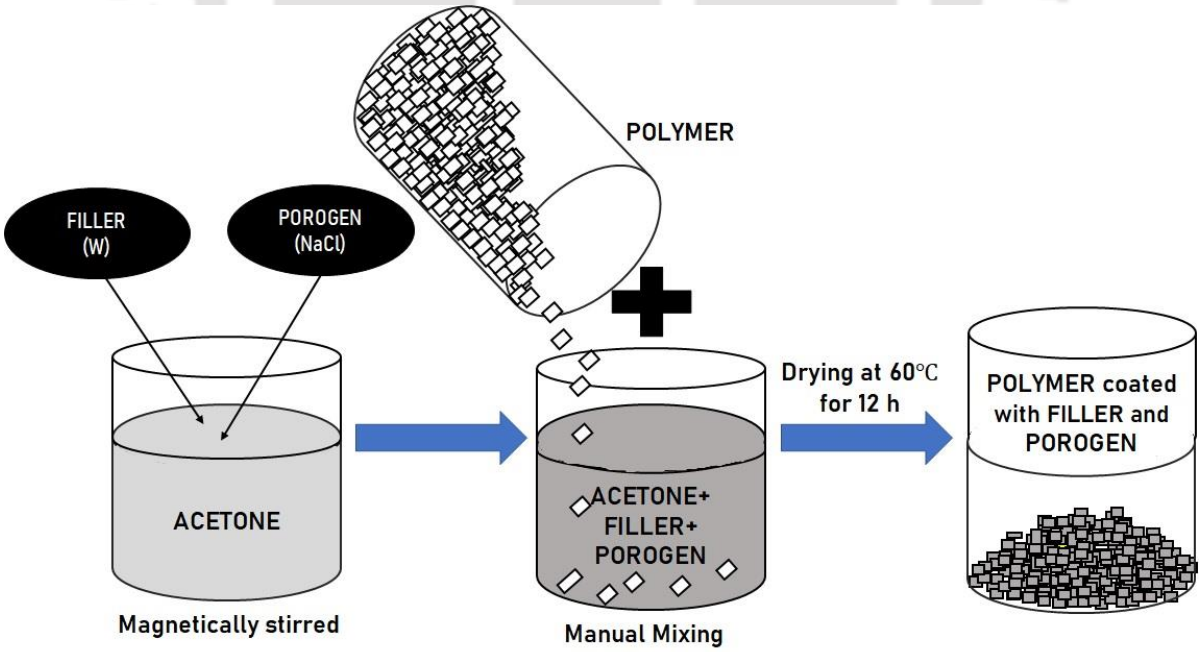

Fig 3.2. Schematic representation of the mixing process of the polymer, filler, and porogen

To produce the porous SMPU sample, the NaCl is used as a porogen and mixed with SMPU before the extrusion process. To ensure superior mixing between them, NaCl is dispersed in acetone by magnetic stirring and poured over the pellets, which are manually hand-mixed, and the weight ratio of pellet and salt is maintained at 1:1. The mixture is then kept at 60°C for 12 h for the acetone to dry. The above-discussed procedure is repeated to make the tungsten filled SMPU filament, where NaCl (43 wt%) and Tungsten (7 wt%) are dispersed in acetone prior to mixing with SMPU, as shown in the schematic representation in Fig. 3.2.

3.3.2 Filament extrusion

As the pure SMPU pellets cannot be directly used for the 3D-FFF process, the pellets are required to be converted in the form of filaments. The pellets as received from the company are used as a raw material, which is extruded through a twin-screw extruder. The pellets are dried at 100°C for 4 h in a hot air oven to remove the moisture from the pellets before extruding. The twin-screw extruder (Model: ZV20, Make: M/s Specifiq, India) has an L/D ratio of 40 and the screw length of 820 mm with four heating zones, which are maintained progressively at 180°C, 185°C, 190°C, and 195°C to make the filament. The temperature at each heating zone is set after the trial and error method, where the least number of defects on the filaments is observed by the naked eye. The filament is extruded through a die of 2 mm circular cross-section hole and the extruder rotating at 30 rpm, and it is immediately cooled by immersing it in a water tank to retain its diameter. The diameter of extruded filaments is maintained within 1.6 ± 0.1 mm in order to use them in the FFF process. The sections of filaments containing defects such as voids and bubbles are discarded.

The operational parameters such as temperature, and extruder speed are fine-tuned to produce good quality filaments for 3D printing. The temperature of the heating zone in the twin-screw extruder is increased by 5°C in each zone to compensate the increase in viscosity

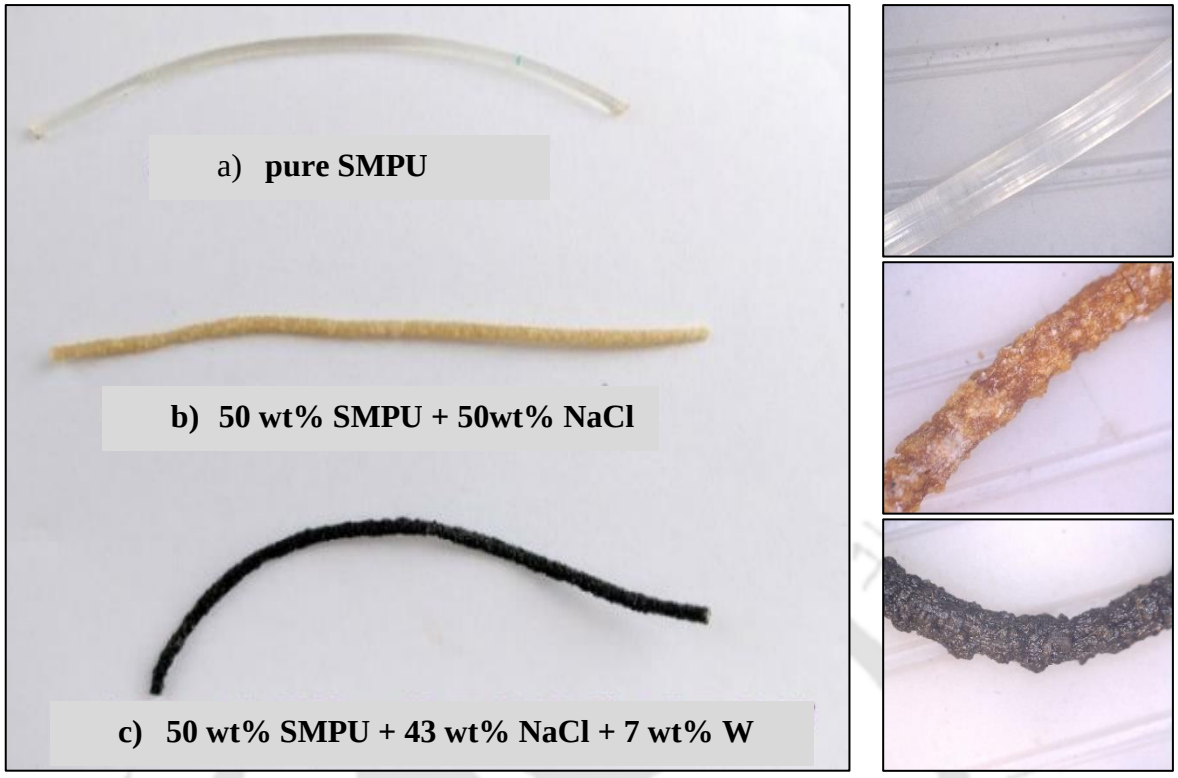

Fig. 3.3. Extruded filament: (a) pure SMPU, (b) 50 wt% salt filament, (c) 43 wt% salt + 7 wt % Tungsten filament

of the melt mixture due to the dispersion of NaCl and Tungsten. It is assumed that water cooling of the NaCl filled SMPU filament derived from the twin-screw extruder did not leach the salt as the filament is allowed to pass through a water bath for 10–15 s, and it is dried instantly. The different types of extruded filaments obtained from the above methodology are shown in Fig. 3.3, where Fig. 3.3 (a), 3.3 (b), 3.3 (c) show the pure SMPU filament, 1:1 SMPU and NaCl filament, and the 50:43:7 SMPU, NaCl, and tungsten mixed filament, respectively. The salt and tungsten filled filaments are rough on the surface due to protrusion of the filler particles at their high concentration. Due to the contraction of the polymer matrix during the cooling of the extruded filaments, the salt particles are pushed towards the outer periphery of the filaments causing the poor morphology of the filaments. The reduction in size of the salt particles and optimization of the extrusion process parameters would aid in improving the quality of the filaments. To prevent the humidity-induced premature leaching of salt particles from the

filaments, they are stored in a dry environment at 80 °C in a hot-air oven until it is used in a 3D Printer to get the desired components/parts/test samples.

3.3.3 3D printing of the filaments

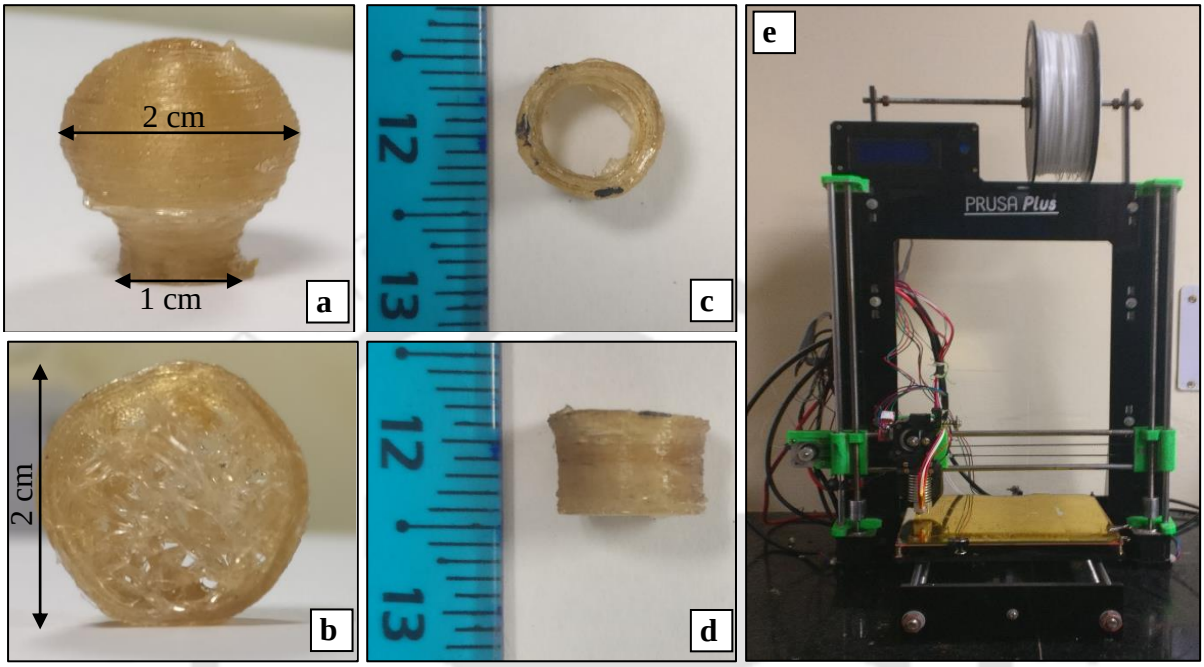

Fig. 3.4. FDM printed SMPU in different shapes: (a) aneurysm, (b) cylinder (2cm dia) with web-like structure in the lumen, (c) lateral view: stent (cylinder); (d) longitudinal view: stent; (e) Prusa i3 3D printer

The fabricated filaments are processed through a Prusa i3 3D printer, shown in Fig. 3.4 (e), running on Marlin firmware to produce the custom shaped products. The CAD models of the physical parts are prepared using AutoCAD, and the toolpath (G-code) for the printer is generated by an open-source software Slic3r. Few complex shapes such as in the shape of the aneurysm, cylinder with web in the lumen, and stent fabricated by FFF are shown in Fig. 3.4.

All the samples which are fabricated for the purpose of characterization are printed in the same conditions to avoid the influence of print orientation and other operating variables. The 3D CAD models are sliced into 0.2 mm layer height and printed with 100% material infill at an alternating angle of +45° and −45°. The printing is done with a 0.8 mm diameter nozzle at

20 mm/s print speed and 55°C build surface temperature. The nozzle diameter of 0.8 mm is used during printing for easy passage of the filament containing filler particles. The nozzle temperature is maintained at 210°C for pure SMPU, 230°C for both salt-filled SMPU, and the Tungsten filled SMPU in order to compensate the increase in viscosity of the polymer melt mixture due to the addition of filler materials. Rectangular samples having a dimension of 4 cm x 1 cm and thickness of 0.75 mm and 1.5 mm are printed using pure SMPU, salt filled SMPU, and Tungsten filled SMPU. In addition, two cubes of 1 cm x 1 cm x 1cm size are also fabricated using the Tungsten filled SMPU.

3D printing with FFF technology is difficult for polymers with low glass transition temperature. The polymer loses its stiffness at normal room temperature, which makes it difficult for the printing process as the softened filament cannot be extruded through the nozzle. Also, the gripping force of the extruder rollers creates uneven cross-section, which prevents the filament from reaching the heated portion of the nozzle. It is avoided in this case by printing the desired component at an ambient temperature of 18°C, i.e. below the glass transition temperature of the polymer.

3.3.4 Leaching of the product

The printed samples are soaked in distilled water, and magnetically stirred for 48 hours to complete the leaching process. The liquid medium is refreshed every 8 hours to enhance the process by decreasing the concentration of dissolved salts. The weight of the sample is measured continually to evaluate the progress of the leaching process and calculate its density.

3.3.5 Compression-molded sample

To compare the properties of the 3D FFF printed samples with the conventional manufacturing process, pure SMPU is also processed in a hot press. The extruded filament of

pure SMPU is cut into pellets before processing. A cuboid sample having the dimension of 20 cm x 20 cm x 0.6 cm is prepared at 160^{o}C and 3 MPa pressure. The processing parameters are chosen on the basis of defect free samples after a few trials. The SMPU is dried for 4 hours at 80°C before processing in a compression molding machine (Model: HYPR-25T, Make: M/s Saumya Machineries Pvt. Ltd, Ahmedabad, India) to prevent the formation of bubbles and other defects in the final sample due to the presence of moisture. HYPR-25T is an intermeshing counter-rotating screw extruder.

3.4 CHARACTERIZATION OF 3D PRINTED SAMPLES

3.4.1 Porosity and density of the samples

The density of the samples is determined by measuring its weight and volume by Archimedes' principle. The porosity of the samples is calculated based on the loss of its weight after the leaching process as the voids created in the sample is proportional to the volume of salt leached out. The pore volume is calculated based on the weight loss of the sample and the density of NaCl, i.e., 2.16 g/cm^3. The density of the SMPU, 1.25 g/cm^3, is referred from the datasheet of the material [115], which is also verified from the compression molded samples. Five samples from each category are measured for calculating the porosity, and density. The theoretical density of rest of the samples is calculated by the ratio of weight fraction of the components to the density of individual component , and it is expressed as follows [118]:

$$\rho_c = \frac{1}{\sum_{i=1}^{n}\left(\frac{W_i}{\rho_i}\right)} \qquad \ldots(3.1)$$

where ρ_c = density of the mixture, W_i = weight fraction of ith component, and ρ_i = density of the ith component.

3.4.2 Morphological studies on the samples

The morphology of the materials, filaments, and porous structure of SMPU are observed using Field emission scanning electron microscope (FE-SEM). The porous SMPU sample, porous Tungsten SMPU, and extruded SMPU-Tungsten filament are cut across the cross-section with a sharp knife and cleaned using the ultrasonic bath to remove any debris to observe the clear porous structure. The samples are sputter coated for 240 sec at 4 mA with gold using a coater. The samples are then imaged using the FE-SEM (Model: Sigma, Make: M/s Zeiss Inc, Oberkochen, Germany).

3.4.3 Thermomechanical studies on the samples

Thermomechanical tests are conducted on a dynamic mechanical analyser (DMA, Model: *DMA 242 E* Artemis, Make: M/s Netzsch GmbH, Selb, Germany). The solid rectangular specimens approximately 0.5 mm thick, 5 mm wide and 15 mm long are cut from a larger 3D printed sample with a sharp knife. The specimen is mounted using film tension fixtures and preloaded by 1 mN force to maintain its straightness. The test is run from -10°C to 60°C and heated at the rate of 5°C/min. The sample is kept under an isothermal condition at -20°C for 10 minutes to reach thermal equilibrium before starting the experiment. During the test, the strain oscillated at a frequency of 1 Hz with a peak-to-peak amplitude of 0.5%. The same test is also performed on the compression-molded pure SMPU to compare the effect of FFF process on the thermomechanical properties. Due to unavoidable experimental constraints, single specimen from each category is tested on the DMA.

3.4.4 Studies on thermal stability and leaching of particles

The thermogravimetric analysis of the test samples is done to confirm the weight fraction of the tungsten powder in the SMPU and verify the complete leaching of the salt from the

matrix. Moreover, the thermal stability of the porous sample is also studied, where the samples are heated from 27°C to 1300°C at 20°C/min in an Argon environment using a thermogravimetric analyzer (TGA) (Model: STA 8000, Make: M/s Perkin Elmer, USA). Due to experimental constraints, single specimen from each category is tested.

3.4.5 Shape memory test

A typical test cycle of shape memory studies consists of two steps: a programming step and a recovery step. The shape memory test is carried out on a 3D printed cubic sample (10 mm x 10 mm x 10 mm) printed with 100% infill. Salt is leached out of the sample to generate the porosity in the cubical sample. The porous Tungsten SMPU composite cube is heated to 60°C, above its glass transition temperature (T_g= 37°C) in a hot-air oven. The cube is then compressed to a thickness of 5 mm in one of its dimensions at 60°C and is placed in a freezer at -10°C to fix its compressed shape, which is the temporary shape of the test sample. During the free recovery step, the compressed cube is placed in a water bath at 40°C, and the test is conducted until the full shape recovery of the sample is observed. The dimension of the test sample is measured along the compressed direction to evaluate its shape recovery. This test is conducted on 2 different samples, and it is carried out several times on the same sample to demonstrate its repeatability.

3.4.6 Radiopacity studies

The radiopacity test is done as per ASTM F640, where Aluminium (purity >99%, Al 1100 series) wedge having a varying thickness of 1 mm to 10 mm is taken as a standard reference and it is shown in Fig. 3.5. The test samples are printed into the rectangular pieces, and the X-ray fluoroscopic images are taken with clinical standard X-ray equipment operated at 60 kVp and 12 mAs. The pixel intensity (0=black, 255=white) of the greyscale samples is observed with the help of ImageJ software.

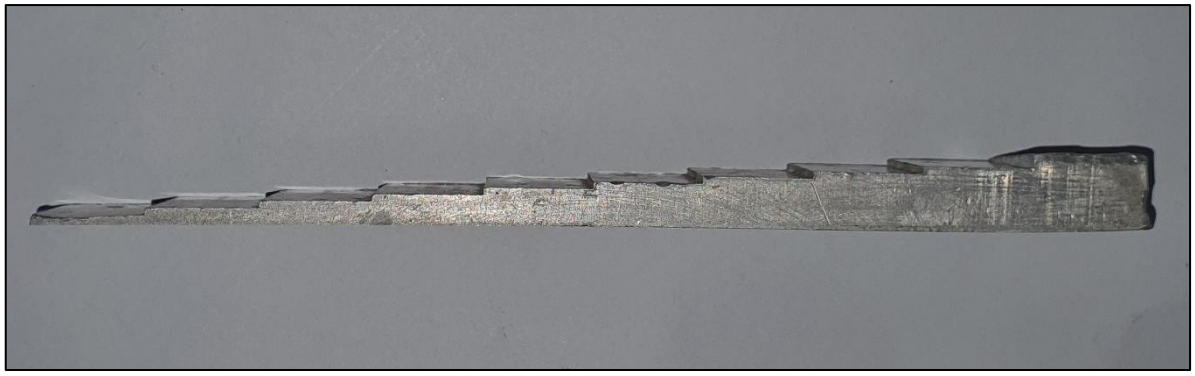

Fig: 3.5. Aluminium 1100 series wedge (1 mm to 10 mm thickness) as a standard reference

3.5 RESULTS AND DISCUSSION

3.5.1 Samples

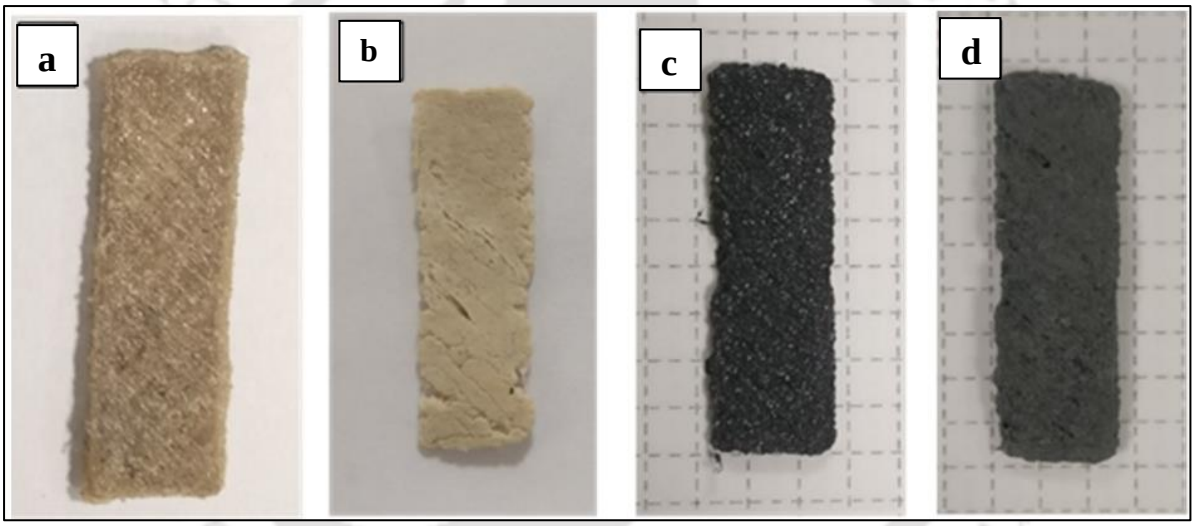

Fig. 3.6. The 3D printed samples: (a) salt filled sample, (b) leached porous SMPU, (c) unleached tungsten filled SMPU, (d) porous tungsten filled SMPU (after leaching)

The 3D printed rectangular samples obtained from the fabricated filaments are shown in Fig. 3.6, where the 45° raster printing of the samples can be observed. The salt-filled printed SMPU and its porous form obtained after the leaching process are shown in Fig. 3.6 (a) and 3.6 (b), respectively. Similarly, the tungsten filled SMPU samples before and after the salt leaching process are shown in Fig. 3.6 (c) and (d), respectively. It is observed that the samples retained their shape after the leaching process, and the formation of pores is seen in the leached samples after the removal of salt particles. The salt filled samples reflected and refracted the

light rays due to the presence of salt crystals which made them to shine. Thus, after leaching the salt particles, the shine of the samples is subdued.

The addition of 50 wt% (43 wt% NaCl + 7 wt% W) fillers increased the viscosity of the polymer and also caused a blockage in the nozzle while printing. Thus, a nozzle having a radius of 0.8 mm is used to avoid the above problems. However, it decreased the quality of the printed objects though they maintained good dimensional adherence with the CAD models. The printed samples after the leaching process looked like a foam, as shown in Fig. 3.6 (b) and (d), due to the removal of the salt from the surface.

3.5.2 Morphological studies

The FESEM images of the salt particles and tungsten particles used in this study are shown in Fig. 3.7 (a) and (b), respectively. A wide range of shape and size of the salt particles are observed from Fig 3.7 (a). The manufacturer of tungsten particles used in the present study reported their size in the range of 0.6-1 µm, which is confirmed from Fig. 3.7 (b). The FESEM images of the cross-sectional surface of extruded SMPU tungsten filament is shown in Fig. 3.7 (c, d), where the embedded salt particles are observed in the filament. The salt particles are lodged in the polymer matrix, and they do not have any interfacial bonding between them, which is observed from the presence of micron level gap between the salt crystals and the matrix. In addition, the agglomeration of salt particles in certain sections and voids are also observed in the filaments. It is also observed that the salt particles are inhomogenously distributed over the filament and small pores are also randomly distributed over the cross section. Fig. 3.7 (e, f) and Fig. 3.7 (g) show the cross-sectional view of porous SMPU samples, and porous Tungsten SMPU, respectively. It is observed from Fig. 3.7 (e, f) that the porous SMPU has many numbers of different sized and unevenly spaced open pores, where the pore sizes ranging from 250 µm to tens of µm are observed. Very similar observations are also made

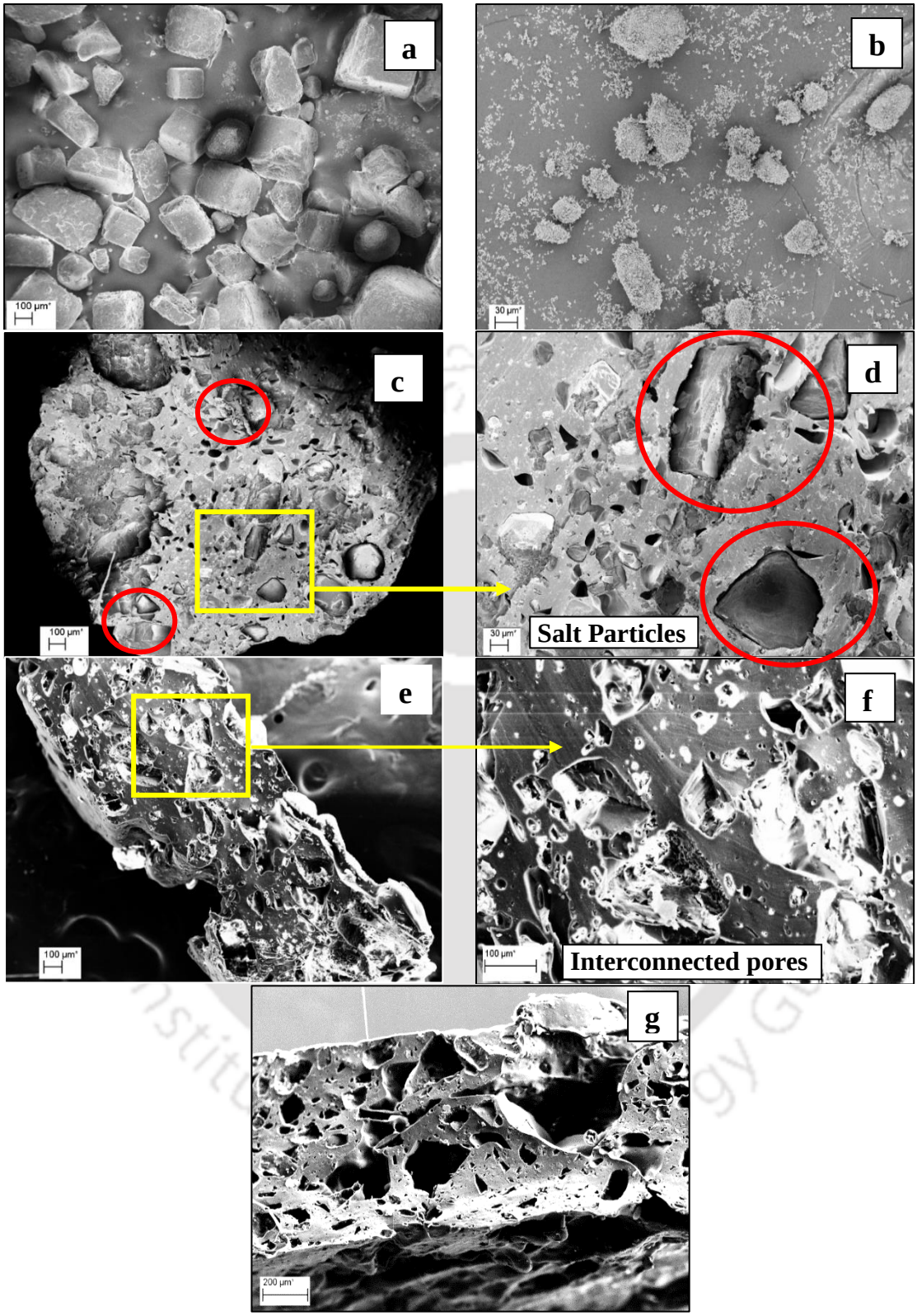

Fig. 3.7. Surface morphology of: (a) Salt particles, (b) Tungsten particles; Cross sectional view of: (c) extruded SMPU Tungsten filament (100X), (d) enlarged view of extruded SMPU Tungsten filament (400X), (e) Porous SMPU sample (112X), (f) enlarged view of Porous SMPU sample (350X), (g) Porous Tungsten SMPU sample

in the porous Tungsten SMPU, and it is shown in Fig. 3.7 (g). Further, different size of pores are also noted in the larger pores, which confirmed the presence of the inter-connected porous network. In addition, no salt particles are observed in the leached sample.

The small pores observed in the extruded tungsten filament as shown in Fig 3.7 (c, d) can be attributed to dislodging of the small salt particles from the matrix due to non-existent interfacial interaction between them, and void generation during the extrusion process. Since a wide range of salt particle sizes (<180µm) is used in the present study, the same sizes of pores are also observed in the porous SMPU. The agglomeration of salt particles and uneven distribution of them during the extrusion process might have created the large-sized voids. As the distribution of the salt during the extrusion cannot be controlled in an orderely manner, random pores are also observed in the samples.

3.5.3 Porosity and density studies

Table 3.2. Density of the samples and their porosity

S No.	Sample	Experimental density of the sample (after leaching) (g/cm^3)	Theoretical density of fully leached sample using Eq 3.1 (g/cm^3)	Theoretical porosity (%) considering full leaching	Porosity (%) based on weight loss of the sample
1	Molded SMPU	1.25	NA	NA	NA
2	3D printed SMPU	1.20±0.008	NA	NA	NA
3	Porous SMPU	0.72±0.013	0.79	36.5	36.05±0.15
4	Porous Tungsten SMPU	0.87±0.015	0.95	33.0	32.7±0.1

The density and porosity of the SMPU and its composites obtained after the leaching process are reported in Table 3.2. It is observed that the density of the 3D printed pure SMPU is lower than that of the compression-molded sample. It is noted that the density of porous SMPU and porous Tungsten filled SMPU is observed to be 0.72 ± 0.013 g/cm^3 and 0.87 ± 0.015 g/cm^3,

respectively. The experimental results are found to be less than that of their theoretical values, and it is due to the characteristic of the FFF process, where the extruded polymer raster is placed next to each other, and the layers are deposited one over another to form the part. In case of compression molding, it involves the application of high pressure to compact the molten material into the die cavity. Furthermore, the pressure applied during the cooling period of the product is expected to compensate the shrinkage effect of the material, which resulted in denser products compared to FFF processed parts.

Since the density of 3D printed samples is less than that of the molded counterparts, the porosity calculated from the density is not immaculate. Thus, the weight of the salt leached out of the sample is considered to calculate the porosity of the sample, as both are having a linear relationship between them. The porosity of the sample having 50 wt% and 43 wt% salt is calculated to be about 36.05 ± 0.15% for porous SMPU and 32.7 ± 0.1% for porous Tungsten SMPU composite, respectively. There is no leaching of the tungsten powder during the process, and it is also verified by TGA, where the same weight fraction of tungsten is observed before and after the leaching process. Based on the results, it is inferred that the salt has been completely leached out and a network of interconnected pores in the polymer has been formed due to same. The difference between the theoretical and experimental results of the porosity can be attributed to the inhomogeneity of salt distribution during the extrusion process, which is confirmed from the morphological studies, and the left-over salt particles, which are fully enclosed within the sample.

3.5.4 Studies on thermal stability and leaching of particles

The thermogravimetric studies on different samples are shown in Fig. 3.8, where the initial weight loss of about 2% is observed till 200°C in all the samples except salt crystals, and it is due to the presence of moisture in the samples. The detailed view of the initial degradation of

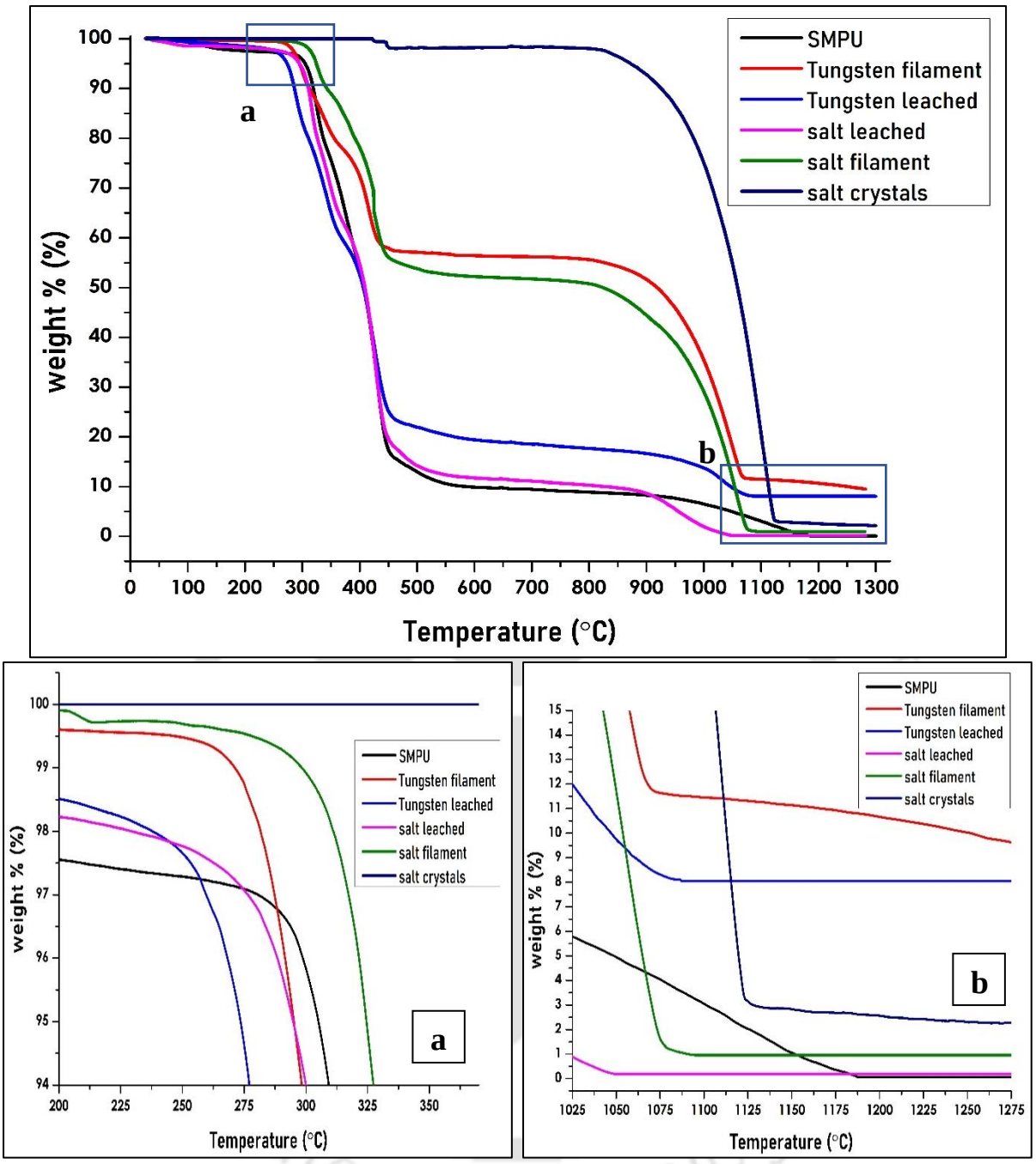

Fig. 3.8. TGA curve of the filaments and leached samples with the detailed view of (a) initial degradation, and (b) the final residue

different SMPU samples is given in inset (a) of Fig. 3.8, where the pure SMPU is observed to degrade from 275°C onwards. The extruded SMPU salt filament and the SMPU tungsten filament exhibited thermal stability till 280°C, and 265°C, respectively, and the corresponding salt leached porous samples showed thermal stability till 258°C and 240°C. The thermal stability of the porous SMPU and porous Tungsten SMPU is decreased by 6.1% and 12.7%,

respectively, in comparison to that of pure polymer. It is also observed that the thermal stability of 3D printed porous SMPU sample is decreased in comparison to that of the extruded filaments and it can be attributed to the dual thermal processing cycle, and the higher processing temperature of 230°C used during the FFF process. The residual weight(%) of different samples tested in the present study at 1250°C is reported in Table 3.3, and the detailed view of the final residue is provided in the inset (b) of Fig. 3.8. The pure SMPU left a residue of 0.05% at 1250°C. The pure salt started to degrade at 800°C, and about 2.29% is left at 1250°C. It is observed that the residue left by the porous SMPU and the porous Tungsten SMPU is about 0.19% and 7.27%, respectively, and the latter confirmed that the tungsten is not removed during the leaching process. The residue of SMPU Tungsten filament is observed to be 8.54 wt%, which is due to the presence of both the salt particles and tungsten particles.

Table 3.3. Residual weight % of different samples at 1250° C

SMPU	SMPU Salt filament	Porous SMPU	SMPU Tungsten filament	Porous Tungsten SMPU	Salt crystal
0.05	0.95	0.19	8.54	7.27	2.29

3.5.5 Thermomechanical studies

Fig. 3.9 (a) shows the storage modulus of the different SMPU samples obtained by compression molding and 3D printing technique in the temperature range of -10°C to 60°C. It is observed from Fig. 3.9 (a) that the storage modulus of test samples in the glassy region started to decrease slowly with an increase of temperature in the range of -10°C to 10°C. There is a drastic reduction in the storage modulus by two orders of magnitude, when the temperature is nearing to the glass transition point. The storage modulus of all test samples in the rubbery region is converged into a plateau in the order of few MPa irrespective of the type of sample.

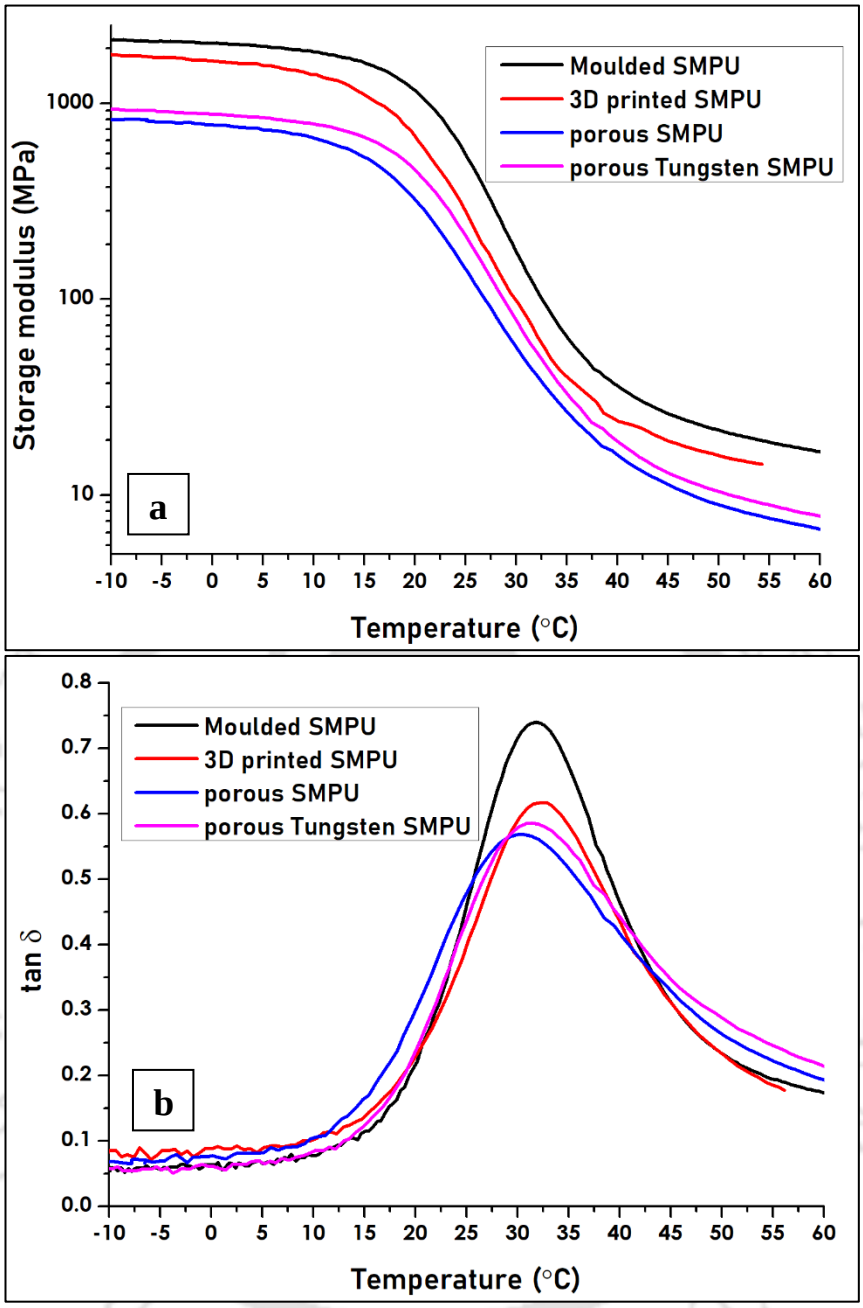

Fig. 3.9. (a) Storage modulus and (b) tan δ curves of molded and 3D printed SMPU samples

Table 3.4. Storage modulus at -1°C and glass transition temperature of the samples

Sample	Storage modulus (MPa)	Glass transition (T_g) (°C)
Molded SMPU	2031	31.8
3D printed SMPU	1662	32.1
Porous SMPU	783	30.0
Porous Tungsten SMPU	883	31.4

The storage modulus of the sample in the glassy state at -1°C and the glass transition temperature of all test samples are reported in Table 3.4. It is observed that the molded SMPU showed about 20% higher storage modulus than the 3D printed SMPU. In case of porous SMPU, the storage modulus is observed to be decreased by 61% and 53% in comparison to that of the molded SMPU and 3D printed SMPU, respectively. However, a 13% increase in the storage modulus of porous Tungsten SMPU is observed when compared to the porous SMPU.

The difference in storage modulus between molded SMPU and 3D printed SMPU by FFF technique can be attributed to the lower density of the FFF sample in comparison to that of the sample obtained by the molding process, as reported in Table 3.3. The storage modulus of porous SMPU and porous Tungsten SMPU is observed to be decreased by 53%, and 47%, respectively in comparison to that of 3D printed SMPU due to the lower density and porosity of the samples. Further, the addition of tungsten filler in the polymer matrix also assisted in increasing the storage modulus by 13% in comparison to that of porous SMPU and the same has also been reported by Yang *et al.* [110].

Fig. 3.9 (b) shows the damping factor (tan δ) of different SMPU samples tested in the present study in the temperature range of -10°C to 60°C. The temperature corresponding to the peak value of tan δ is specified as the glass transition temperature of the sample, and the results are reported in Table 3.4. The glass transition temperature of all the test samples is observed to be in the range of 30 to 32.1°C and there is no significant difference in the glass transition temperature of both porous SMPU and solid SMPU. It is inferred that the glass transition temperature of the test material is not significantly influenced by the processing techniques such as extrusion, compression molding, FFF processing, and salt leaching as there is no change in the polymer structure during these processes. Further, the porosity and density of the samples have a negligible effect on the glass transition temperature of the samples, which is also supported by Nardo *et al.* [85].

3.5.6 Shape memory studies

Fig. 3.10 (a) shows the 3D printed porous Tungsten SMPU cubic sample, which is used for the shape memory studies. The test sample after completing the programming step, i.e. temporary shape, and recovery process, i.e. recovery shape, is shown in Fig. 3.10 (b) and Fig. 3.10 (c), respectively. It is also observed that the compressed test sample has retained its temporary shape with very minimal change in dimension after it is programmed and kept at -10°C for 4 hours. In addition, the sample is observed to have completely regained its original shape after the recovery process.

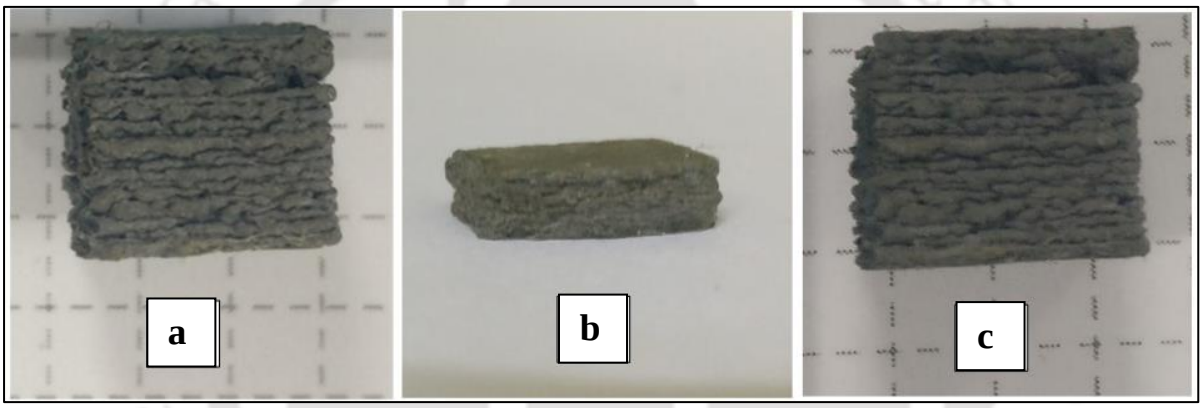

Fig. 3.10. Shape memory test: (a) Porous Tungsten SMPU cubic sample (test sample), (b) Programmed temporary shape of the test sample, (c) Test sample after shape recovery

Fig. 3.11 shows the shape recovery process of the compressed test sample at different time intervals after placing it in a water bath at 40°C. Initially, the test sample sank to the bottom of the beaker, and it started to move upwards along with its expansion during the heating process and started to float on the water surface after 60 sec. It is also observed that the shape recovery rate is rapid during the initial 120 sec, and then it is decreased at the later stage. The shape recovery of the cube is measured until 480 sec. The shape recovery is observed to be 95% during the first recovery cycle, and it is increased to 100% during the subsequent recovery cycles. It is observed that the porous Tungsten SMPU showed excellent shape holding and

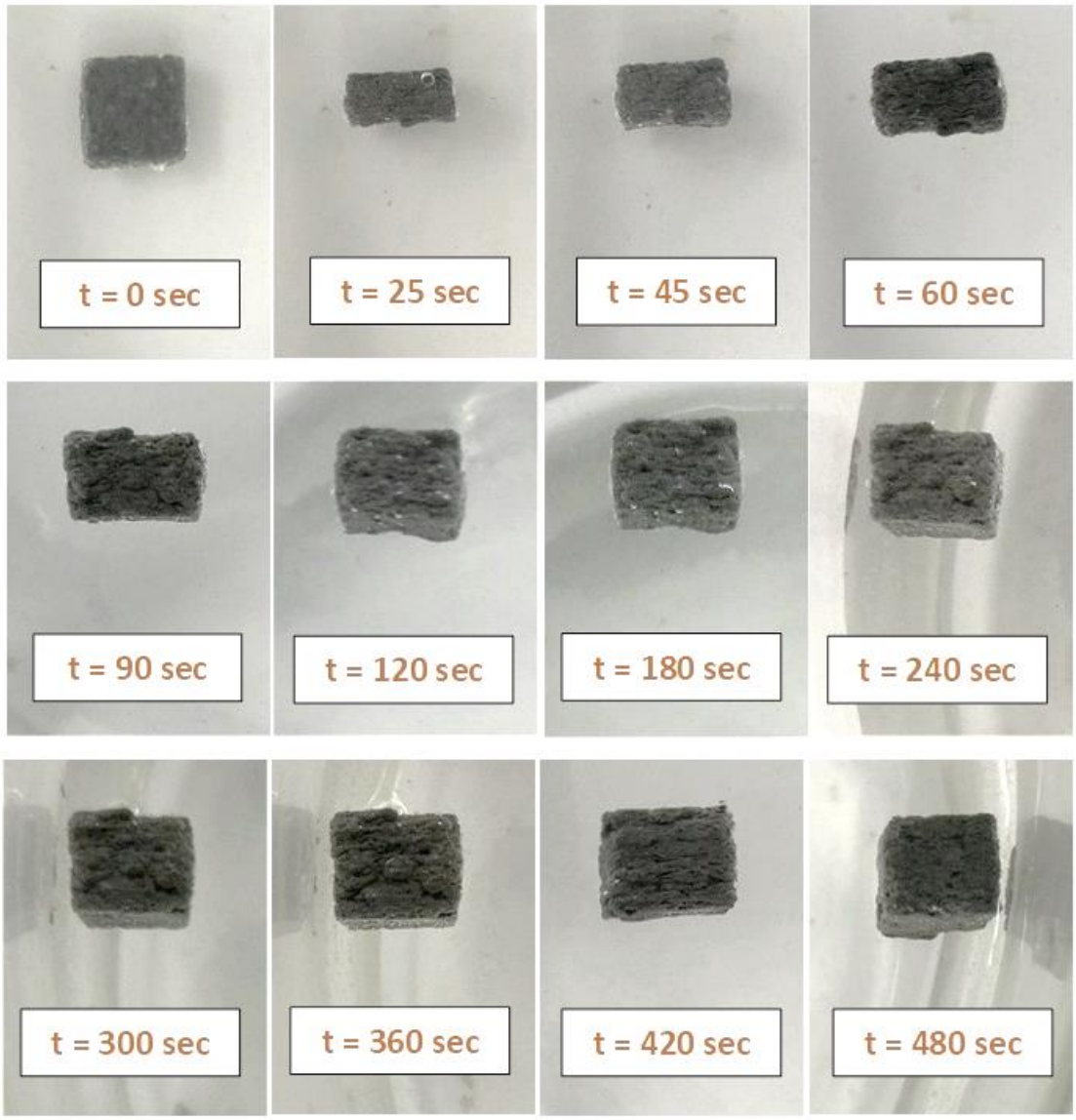

Fig. 3.11. Shape recovery of porous Tungsten SMPU cubic sample at different time intervals

shape recovery characteristics. The recovery of the cube is due to shape memory characteristics of the polymer, which regained its permanent shape after it is heated above its glass transition temperature. The density of compressed porous Tungsten SMPU sample is increased to more than 1 g/cm^3 leading to its initial sinking in the water. Once the sample is put in hot water, it started to expand, and its density is reduced to 0.87 ± 0.015 g/cm^3, which leads to the floating of the test sample on the water. During the first recovery cycle, the shape recovery of the sample is limited to about 95% due to the plastic deformation and initial damage to the porous Tungsten SMPU. During the subsequent cycles, there is minimal plastic deformation and

damage on the porous Tungsten SMPU as the compressive strain generated in the sample remains the same. Further, the polymer chains get oriented along the loading direction, which ensures full recovery of the porous SMPU in the subsequent recovery cycles, which is also confirmed by Tobushi *et al.*[119] *and* Ohki *et al.* [120].

3.5.7 Radiopacity studies

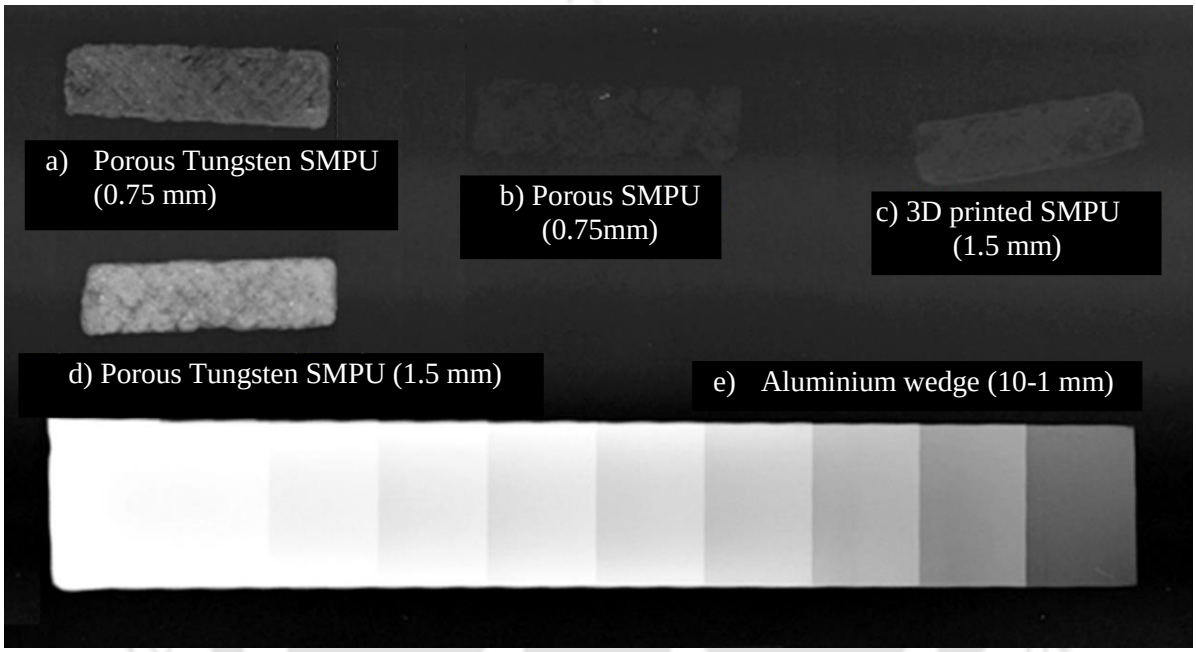

Fig. 3.12. X-ray image of the 3D printed samples: (a) Porous Tungsten SMPU (0.75 mm), (b) porous SMPU (0.75mm), (c) 3D printed SMPU (1.5mm), (d) Porous Tungsten SMPU (1.5mm), (e) Aluminum wedge

The radiograph of the 3D printed samples obtained by FFF process along with the Aluminium wedge prepared as per ASTM F640 is shown in Fig. 3.12, and the quantitative values of their intensity after subtracting its background are reported in Table 3.5. The radiograph of Aluminium wedge is given for comparison, and its radiopacity is increased with thickness. It is observed from Fig. 3.12 that the radiopacity of the porous Tungsten SMPU is increased significantly, and its 1.5 mm thickness sample showed 206% more radiopacity comapared to the Al sample having 1 mm thickness. The presence of Tungsten in porous

SMPU increased the radiopacity of the samples due to its high density and X-ray attenuation characteristics. The least radiopacity is observed in the porous SMPU due to its thickness and reduced density in comparison to that of 3D printed SMPU.

Table 3.5. Pixel intensity of the 3D printed test samples along with Al

Sample along with its thickness	Pixel Intensity	Intensity % relative to 1 mm Al
1mm Aluminum	31.126 ± 2.420	100
3D printed SMPU (1.5mm)	17.578 ± 1.969	56.5
Porous SMPU (0.75mm)	9.850 ± 1.410	31.64
Porous Tungsten SMPU (0.75mm)	30.050 ± 7.036	96.54
Porous Tungsten SMPU (1.5mm)	64.168 ± 11.404	206.14

3.6 SHORTCOMINGS: CORROSION/OXIDATION OF TUNGSTEN IMPLANTS

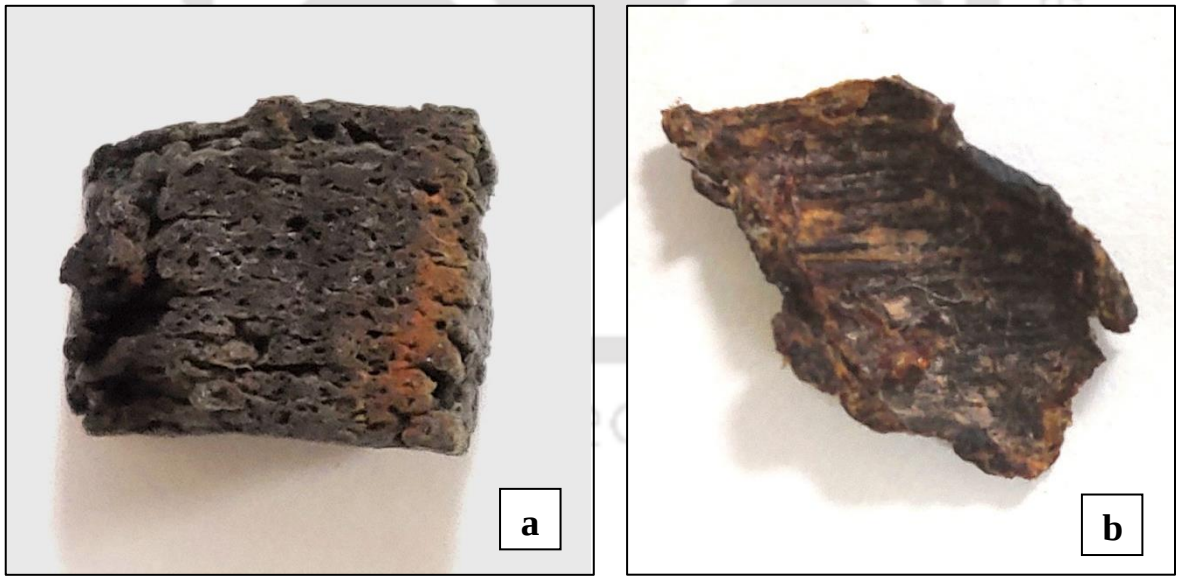

Fig. 3.13. Oxidized porous Tungsten SMPU composite samples: (a) Cross-section of a 3D printed cube, (b) thin sample

Fig. 3.13 shows the oxidized porous tungsten sample. The developed porous Tungsten SMPU composite started to oxidize/corrode uncharacteristically after being kept in an open

atmosphere for about 2 months. A brown/pinkish layer is observed on the outer periphery of the oxidized 3D printed cube, as shown in Fig. 3.13 (a), whereas a thin sample, as shown in Fig. 3.13 (b), is fully covered with a brownish tinge. The interaction of the tungsten powder with the salt particles during the fabrication process must have fast tracked the oxidation of the tungsten. Thus, the implantation of the porous tungsten SMPU under *in vivo* conditions is expected to cause complications and might be even fatal. As such, the tungsten cannot be used as a radiopaque filler in the present form, processing technique or shelf ageing conditions.

3.7 SUMMARY

In summary, a novel processing technique is presented by combining extrusion, the fused filament fabrication (FFF) and salt leaching technique to fabricate the radiopaque, porous, and custom shaped SMPU and its composites. The added advantage of this technique is the elimination of toxic and expensive solvents for dissolving the polymer and porogen. The environmental friendly and biocompatible NaCl is used as a recyclable sacrificial porogen. Based on the proposed methodology, the porous SMPU and its composites can be fabricated in any shape and size, with desirable pore size. From the present study, it is found that tungsten is not desirable to be used as a radiopaque filler in the current processing technique. Thus, a novel material which has radiopaque properties and is compatible with the novel processing technique is required to replace the tungsten.

CHAPTER 4: RADIOPAQUE 3D PRINTABLE SHAPE MEMORY POLYURETHANE COMPOSITES

4.1 INTRODUCTION

A patient-specific, porous, radiopaque, SMPU composite for endovascular embolization is successfully fabricated by a novel method combining filament extrusion, 3D FFF printing, and salt leaching and the results are discussed in the previous section. However, it is observed that the tungsten filled in the SMPU composites oxidized during the shelf aging period, and this process may be further aggravated under *in vivo* conditions and cause local or systemic toxicity. The inefficacy of tungsten as a long-term implant has been highlighted by Idil and Donaldson [121], where they concluded that the corrosion of tungsten in the human physiological environment into either metallic or metal oxide dissolution, and its long term genotoxicity should deter its use in humans. Hence, the tungsten as a radiopaque filler is required to be replaced with a material, which will not have any chemical reaction with the porogen. In order to address the above problems, nano barium sulphate ($nBaSO_4$) is chosen as a radiopaque filler because of the following advantages:

- It is a medically approved contrast agent for diagnostic radiographic examinations.
- It will not react with the NaCl and corrode or oxidize.
- It does not dissolve in water; thus, it will not come out during the leaching process.
- It is not dissolvable in acetone and will not affect the mixing process.

The optimum concentrations of nano $BaSO_4$ is to be added without affecting the other desirable charateristics of the SMPU. In this chapter, solid samples of SMPC are fabricated by compression moulding process to study their material characteristics and to compare them with porous composites. In addition, the solid radiopaque SMPC can replace the existing metallic coils. The SMPC coils can be programmed into a smaller diameter to be sent through a catheter,

and, on receiving stimulus, it will expand and fill the targeted area. The biggest issue with metallic coils is recanalization due to lack of thrombosis. Hence, to increase the thrombosis of the SMP, it is mixed with hydroxyapatite (HaP), which has been successfully used for increasing the bioactivity of the implant. GDC coated with hydroxyapatite is found to increase the biological response of the implant, which led to faster neo-endothelial proliferation and migration at the neck of an aneurysm [122]. Hydroxyapatite has been tested as an embolic agent on rabbits, and they reported that the mild inflammatory response played a synergetic role in ensuring effective thrombosis [123]. It has been reported that HaP nanoparticles possessed good hemostatic characteristics by providing a favorable protein-binding surface, which enhanced the platelet adhesion and the blood clotting formation during the blood coagulation cascade [124]. The above discussed characteristics of hydroxyapatite make it as a good candidate for embolization and to increase the healing rate of an aneurysm. However, the radiopacity of the hydroxyapatite particles is found to be weak, and the use of a large concentration of hydroxyapatite for vascular lesions is also a matter of concern [125].

In order to obtain the advantages of both, hybrid composites consisting of nano barium sulphate as a radiopaque filler material and nano-hydroxyapatite as a hemostatic agent are fabricated. The thermal, mechanical, and shape memory characteristics of both individual and hybrid nanocomposites are studied and reported in this chapter.

4.2 MATERIALS

The SMP, MM3520 (SMP Technologies Inc, Japan) as discussed in chapter 3 has been used to prepare the nanocomposites. For the synthesis of nano barium sulphate, barium chloride ($BaCl_2.2.5H_2O$, 99.9%), disodium ethylenediamine tetraacetic acid (EDTA-2Na.$2.5H_2O$, 99%), and Sodium sulphate (Na_2SO_4) are obtained from M/s Sigma Aldrich, Bengaluru, India and these reagents are used in as-received form. The nano-hydroxyapatite powder is

synthesized from the eggshells of locally available Gallus gallus domesticus, and the orthophosphoric acid (H_3PO_4, 85% aqueous solution) is obtained from M/s Alfa Aesar, Mumbai, India.

4.3 METHODS

4.3.1 Synthesis and characterization of nanoparticles

The process followed to synthesize nano barium sulphate is proposed by Romero-Ibarra *et al.* [126] , and it is briefly described here: A 100 ml of 0.1M $BaCl_2$ is added into a 100 ml of 0.1M EDTA-2Na. $2.5H_2O$ under vigorous magnetic stirring (Model: C-MAG HS 7, Make: M/s Ika, Germany) at room temperature and the pH value (Model: PB-11,Make: M/s Sartorius, Germany) of the solution is adjusted to 6 using Hydrochloric acid (HCl). A 100 ml of 0.1M Na_2SO_4 is added into the above solution under magnetic stirring, and the resulting precipitate from the suspension is collected. The particles are washed thoroughly with distilled water and dried in an oven for 24 h at 110°C. The synthesized nano barium sulphate is characterized by X-ray diffraction (XRD) and Transmission Electron microscopy (TEM) technique.

The nano-hydroxyapatite powder is synthesized as per the methodology proposed by Gergely *et al.*[127]. The collected eggshells are thoroughly washed with soap and water to remove all impurities and is dried in a hot air oven at 110°C for 8 h. The eggshells are calcinated in atmospheric air at 900°C for 4 h in an electric furnace to burn out the organic material and converted them into calcium oxide. It is then crushed into a fine powder in a ball mill (Model: Pulverisette 6, Make: M/s Fritsch GmbH, Germany**)** equipped with an alumina bowl and zirconia balls having 1:10 powder to ball weight ratio for 2 h at 350 rpm. Finally, the calcium oxide powder is mixed with water and orthophosphoric acid with the help of a magnetic stirrer in stoichiometric concentration to get the Ca/P ratio of 1.67 corresponding to hydroxyapatite, and it is also confirmed by XRD.

4.3.2 Preparation of composite samples

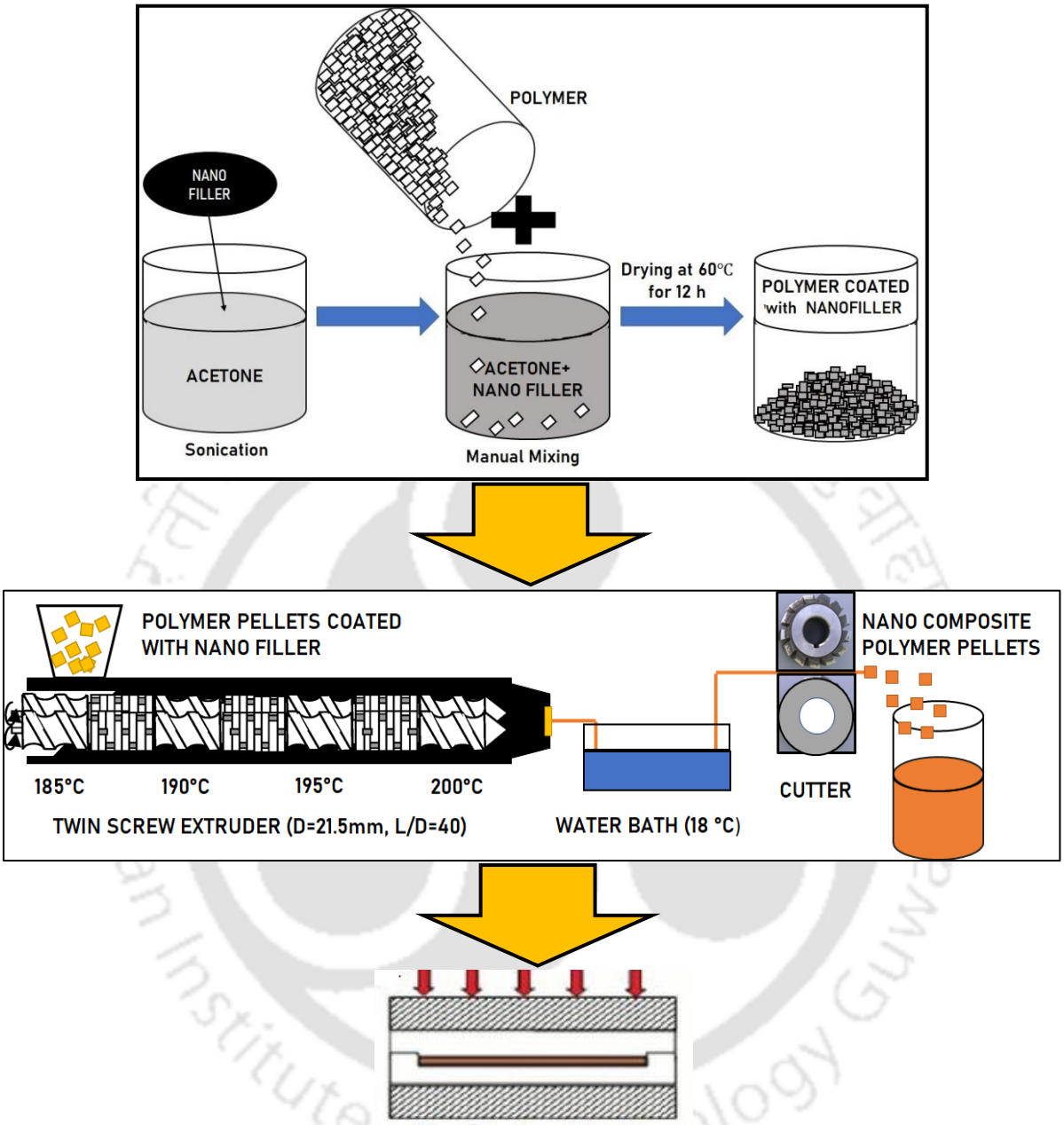

Fig. 4.1. Schematic representation of the processing technique to prepare the polymer composites

The processing technique followed to prepare the SMPU based composites is represented in Fig. 4.1, and the details are given below. The required quantity of filler material, i.e., $nBaSO_4$, nHaP, or both is sonicated in acetone using a bath sonicator (Model: Ultra Met 2002 Ultrasonic Cleaner, Make: M/s Buehler, Germany) to have a better dispersion and

deagglomeration of powder caused by the van der Waal's force of attraction. The suspension is poured on the measured quantity of SMPU and hand-mixed till the polymer is coated uniformly by the fillers. The coated samples are then heated at 60°C for 12 h in a hot air oven to evaporate the remaining acetone and complete the coating process. The SMPC is prepared by melt compounding the coated raw material in a twin-screw extruder (Model: ZV20, M/s Specific Engineering and Automats Pvt Ltd, India) at a screw speed of 100 rpm in the temperature range of 185-200°C at different heating zone. The extruded product in the form of a wire is solidified to obtain a filament in a water bath at 18°C. Finally, the SMPU nanocomposite filament is cut into pellets with the help of a pelletizer. Before each processing step to make the composite samples, the raw materials are dried at 120°C for 4 h to remove moisture in the sample as it has a significant influence on the quality and T_g of the composite test samples.

Dried extruded pellets are moulded in the form of sheets having the dimension of 20 cm x 20 cm x 0.5 mm using a hot press (Model: HYPR- 25T, Make: M/s Saumya Machineries Pvt. Ltd, Ahmedabad). During the moulding process, the bottom plate and the top plate are maintained at 160ºC and155ºC, respectively, with a holding pressure of 6 MPa and these conditions are maintained for 30min. The samples with the required dimension are cut from the sheet for their characterization.

The fabricated nanocomposites and their corresponding nomenclature used in this work are presented in Table 4.1. The pure SMPU dispersed with 4, 10, and 12.5 wt% concentration of nano barium sulphate is referred as 4NB, 10NB, and 12.5NB, respectively. The nano-hydroxyapatite loaded at the concentration of 2.5%, 5%, 7.5% and 10wt% in SMPU is referred as 2.5H, 5H, 7.5H, and 10H, respectively. Similarly, the hybrid composites are referred as 7.5H2.5B, 5H5B, and 2.5H7.5B for the individual filler concentration of 7.5wt% HaP/2.5wt% $BaSO_4$, 5wt% HaP/5wt% $BaSO_4$, and 2.5wt%HaP/7.5wt% $BaSO_4$, respectively.

Table 4.1. Nomenclature of the fabricated composites

Nano Barium Sulphate composites				
Wt.% of filler	4%	10%	12.5%	
Nomenclature	4NB	10NB	12.5NB	
Nano Hydroxyapatite composites				
Wt.% of filler	2.5%	5%	7.5%	10%
Nomenclature	2.5H	5H	7.5H	10H
Hybrid composites (Hydroxyapatite/Nano Barium Sulphate)				
Wt.% of filler	7.5wt%HaP/ 2.5wt% $BaSO_4$	5wt%HaP/ 5wt% $BaSO_4$	2.5wt%HaP/ 7.5wt% $BaSO_4$	
Nomenclature	7.5H2.5B	5H5B	2.5H7.5B	

4.4 CHARACTERIZATION

4.4.1 Mechanical testing

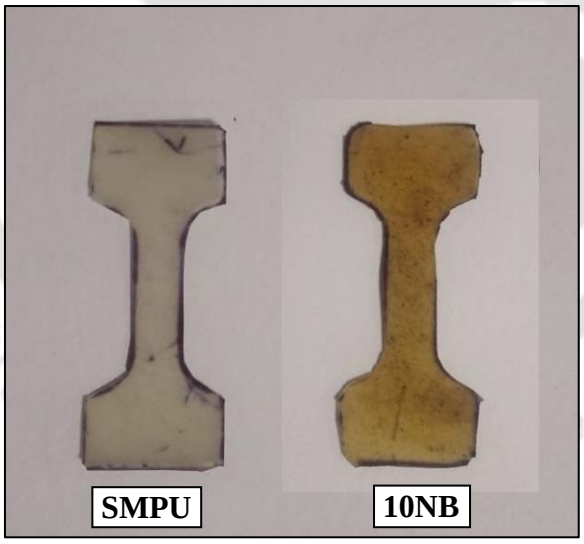

Fig. 4.2. Tensile specimens used in mechanical testing

Tensile tests are conducted at room temperature, which is maintained in the range of 22-24°C as per ASTM D1708. The specimen with the following dimension: thickness 0.5 mm, width 5 mm, gage length 22 mm is cut from the compression molded sheets as shown in Fig. 4.2. An Instron UTM (model: 5944) with a 100 N load cell is used for testing at a crosshead

speed of 5 mm/min. The samples are strained until failure and elongation at break is obtained from the crosshead travel.

4.4.2 Thermomechanical studies

The thermomechanical characteristics of the SMPC under dynamic conditions are studied using a DMA (Model: DMA 242 E Artemis, Netzsch, Gmbh, Germany) as per ASTM D5026-15. Rectangular specimens having a dimension of 5 mm (length), 5 mm (width), and 0.5 ± 0.01 mm (thickness) are cut from the compression molded sheets. Tests are conducted in tensile mode, and is scanned from -20°C to 70°C at a heating rate of 3°C/min. The applied strain and the oscillating frequency are kept at 0.1% and 1 Hz, respectively. The samples are kept in an open atmosphere and are not dried before testing.

4.4.3 Morphological studies

The fracture morphology and distribution of the filler within the SMPC test specimen are done as per the methodology described in Chapter 3. The cross-sectional view of the fractured surface of the composites is observed with an accelerating voltage of 2.5 kV. The crystallite size of the nano barium sulphate is studied using a Transmission electron microscope (TEM) (Model: JEM 2100, Make: M/s JEOL, Japan) at 120 kV. Samples are prepared by evaporating a drop of the aqueous suspension on a Cu TEM grid.

4.4.4 Shape memory cyclic studies

The shape memory cyclic studies are done at constant stress with free recovery conditions using DMTA (Model: DMA 242 E Artemis, Make: M/s Netzsch GmbH, Selb, Germany) under tensile mode conditions. The procedure followed to measure the shape recovery characteristics of test samples is given in Table 4.2. The maximum strain in the sample due to the application of 4N is considered as ε_{max}. The temporary strain of the SMP is denoted as ε_{min} and is measured

Table 4.2. Steps followed for shape memory characterization

Step 1	Heat the sample at 5.0 K/min from 20°C to 70°C and maintain isothermal condition for 5 min
Step 2	Apply 4N tensile force on the sample and maintain isothermal state at 70°C for another 10 min
Step 3	Under the 4N tensile force, cool at 5.0 K/min from 70°C to -25°C and maintain isothermal condition for 10 min
Step 4	Release the force and maintain isothermal state at -25°C for 5 min
Step 5	Heat at 5.0 K/min from -25°C to 37°C and maintain isothermal condition for 60 min
Step 6	Heat at 5.0 K/min from 37°C to 70°C and maintain isothermal condition for 30 min
Step 7	Repeat step 2
Step 8	Repeat step 3
Step 9	Release the force and maintain isothermal state at -25°C for 10 min
Step 10	Repeat step 5
Step 11	Heat at 5.0 K/min from 37°C to 70°C and maintain isothermal condition for 15 min

at the end of step 6. Finally, the temperature of the sample is increased, and the shape recovery is recorded as ε_{rec}. The most important parameters in studying the shape recovery characteristics of a test sample are the shape fixity (R_f) and shape recovery (R_r). Shape fixity is defined as the ability of the SMP to hold on to its temporary deformed shape and shape recovery is defined as the ability of a SMP to memorize or recover the original shape from the temporary deformed shape. Mathematically, shape fixity and shape recovery are determined using the following equations 4.1 and 4.2 [128].

$$\text{Shape fixity, } R_f(N) = \frac{\varepsilon_{min}(N)}{\varepsilon_{max}(N)} \times 100\% \quad \ldots (4.1)$$

$$\text{Shape recovery, } R_r(N) = \frac{\varepsilon_{max}(N) - \varepsilon_{rec}(N)}{\varepsilon_{max}(N) - \varepsilon_{rec}(N-1)} \times 100\% \quad \ldots (4.2)$$

where ε_{max} = maximum strain during loading

ε_{min} = minimum strain fixed during cooling

ε_{rec} = strain recovered after heating

4.4.5 Radiopaque Test

The radiopacity of the test samples is studied as per ASTM F640, as discussed in Chapter 3. The test samples are cut into small rectangular pieces of 0.5 mm thickness. Images are taken using clinical standard X-ray equipment operated at 56 kVp and 16 mAs.

4.5 RESULTS AND DISCUSSION

4.5.1 Structural characteristics of nano $BaSO_4$ and nano-hydroxyapatite nanoparticles

The X-ray diffraction pattern of the synthesized nano barium sulphate is shown in Fig. 4.3(a), and its peaks are observed to be matched with the corresponding Crystallography Open Database (COD) 9000650. The diffraction patterns observed at (011), (111), (002), (210), (102), and (211) planes are the characteristic features of orthorhombic $BaSO_4$ crystals. Thus,

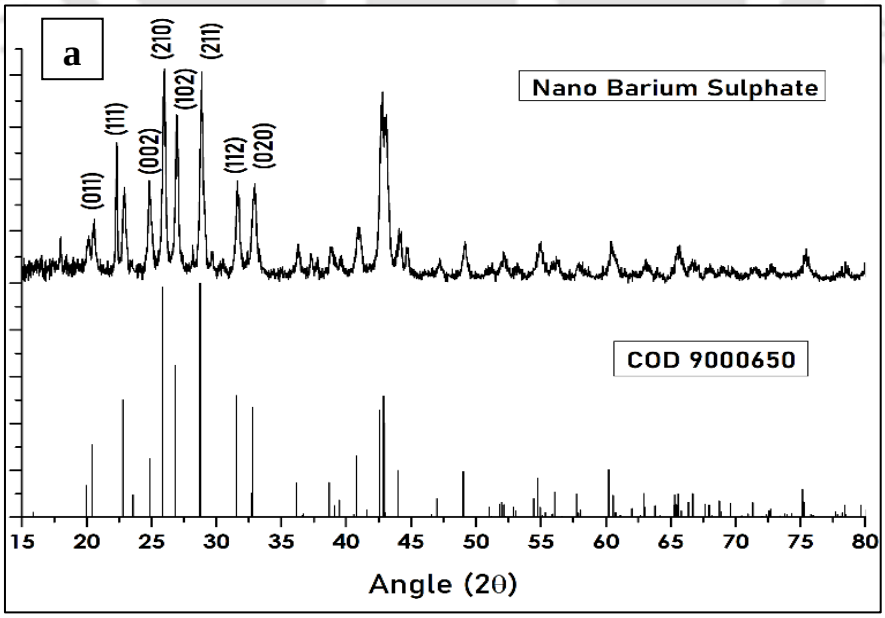

Fig. 4.3. (a) X-ray Diffraction pattern of the synthesized nano barium sulphate and its comparison with COD 9000650 data; (b) TEM image of the nano barium sulphate particles

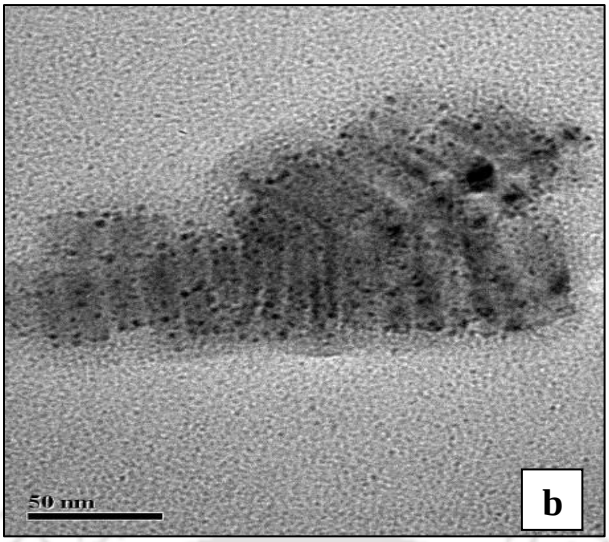

Fig. 4.3. (a) X-ray Diffraction pattern of the synthesized nano barium sulphate and its comparison with COD 9000650 data; (b) TEM image of the nano barium sulphate particles

it is confirmed from XRD spectra that the synthesized $BaSO_4$ has no impurities, which indicates that the prepared sample has high purity in nature. The crystallite size of $nBaSO_4$ is calculated from the Williamson-Hall plot method and is found to be 4 nm. The TEM image of the $nBaSO_4$ is shown in Fig. 4.3 (b), and the size of particles is observed to be in the range of 2-5 nm.

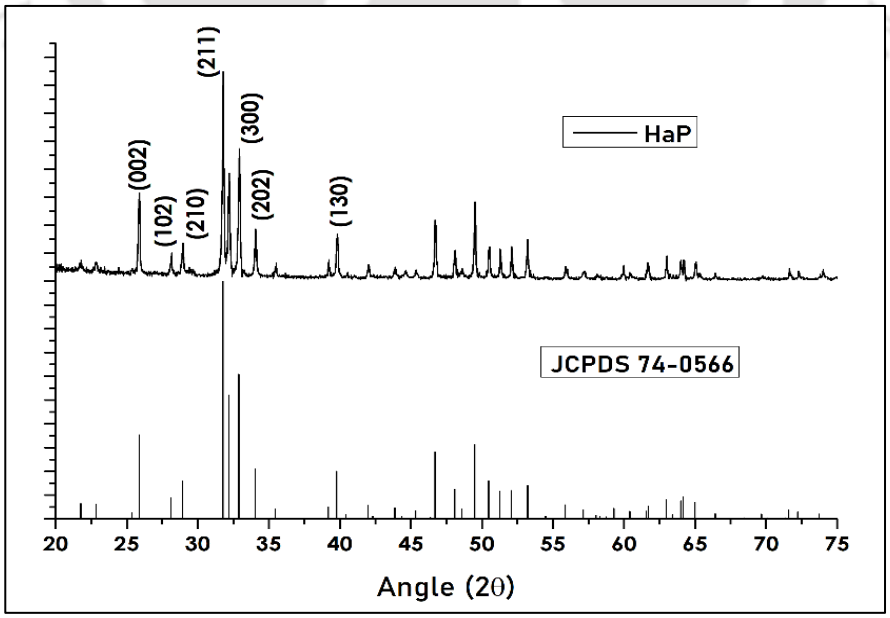

Fig. 4.4. XRD pattern of the synthesized nano-hydroxyapatite and its comparison with JCPDS No. 74-0566

The X-ray diffraction pattern of the nHaP particles and the corresponding data obtained from JCPDS are shown in Fig. 4.4. It is observed that the diffraction pattern of the synthesized nHaP is found to be matched with (JCPDS No. 74-0566) and the crystallite size of nano HaP obtained from the Williamson-Hall plot method is found to be 65 nm. It is also confirmed that there are no impurities present in the synthesized HaP particles.

4.5.2 Mechanical Testing

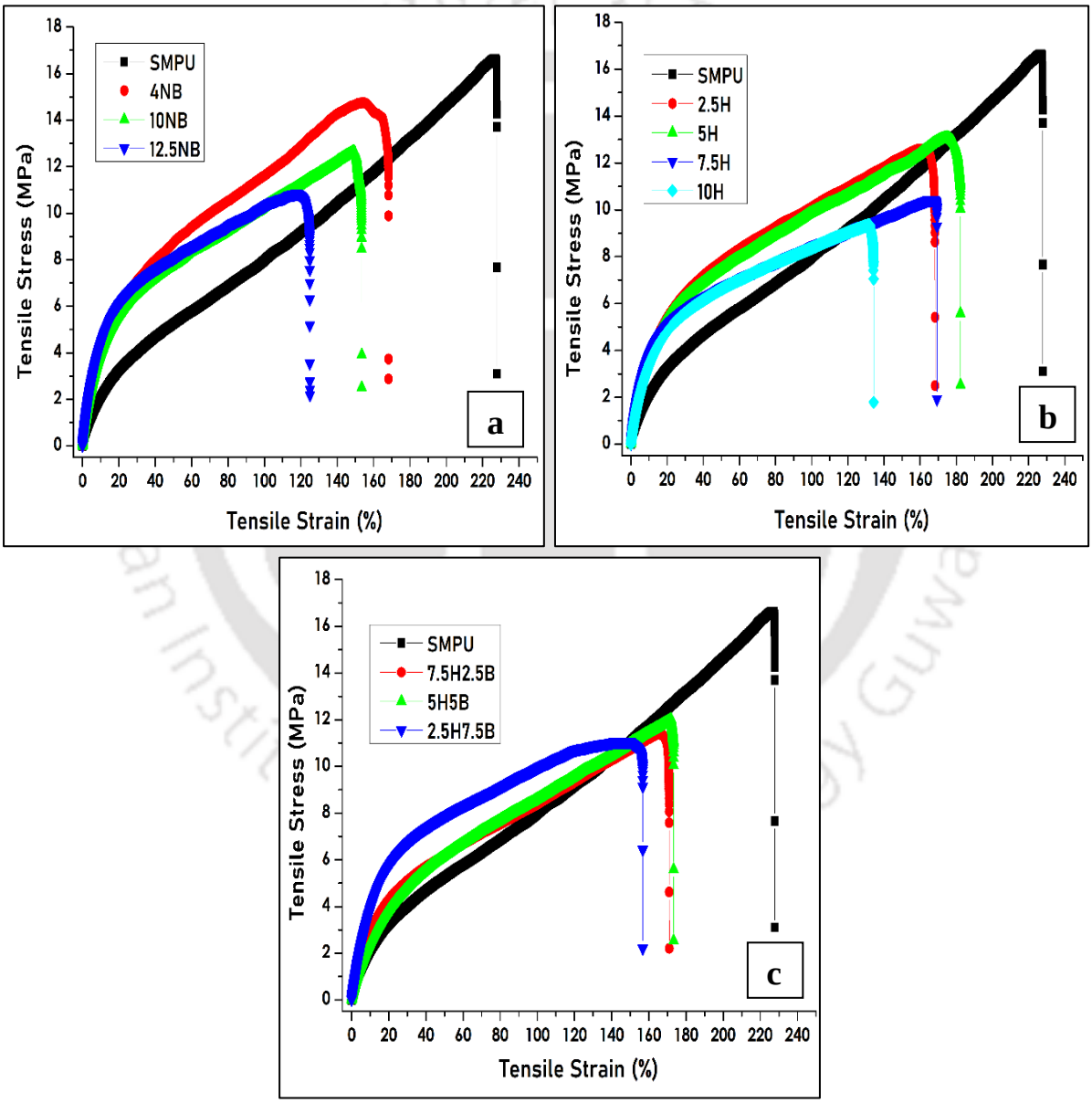

Fig. 4.5. Typical stress-strain curve of SMPU and its composites: (a) SMPU-n$BaSO_4$ composites, (b) SMPU-nHaP composites, (c) hybrid composites

The typical stress-strain curves of the composites namely SMPU-nBaSO$_4$, SMPU-nHaP and hybrid composites obtained from the uniaxial tensile test at room temperature are shown in Fig. 4.5 (a), (b), and (c), respectively. As the SMPU and its composites at room temperature are observed to be above their glass transition temperature, all the samples followed the same pattern and deformed uniformly till fracture after the initial elastic region, which is typical of

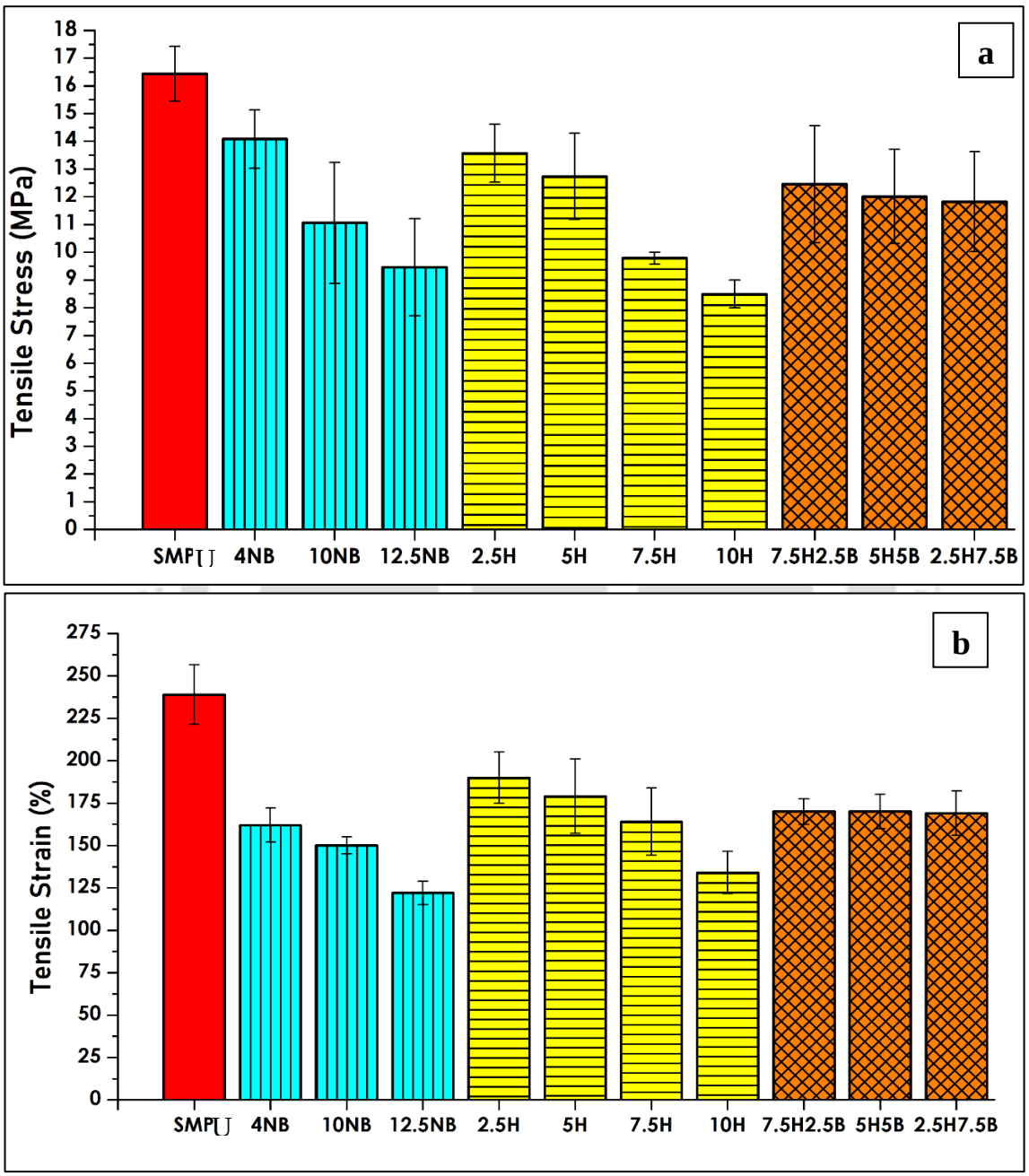

Fig. 4.6. (a) Ultimate tensile strength and (b) failure strain of the SMPU and its composite samples

a polymer in a rubbery state. The tensile strength of the composites is decreased irrespective of types of fillers and their concentration. The ultimate tensile strength and failure strain of the SMPU and its composites calculated from the uniaxial tensile test are shown in Fig. 4.6 (a) and 4.6 (b), respectively. The ultimate tensile strength of SMPU is observed to be decreased by 14%, 32%, and 42% by the addition of 4%, 10%, and 12.5 wt% of $nBaSO_4$, respectively. The tensile strength of the nano-hydroxyapatite composites having the nHaP concentration of 2.5%, 5%, 7.5%, and 10 wt% is decreased by 17.5%, 22.5%, 40.5%, and 48.5%, respectively, in comparison to that of pure SMPU. The reduction of the tensile strength of hybrid composites irrespective of the individual concentration of fillers is found to be in the range of 24-28% in comparison to pure SMPU. The tensile strength of the hybrid composites is not found to be influenced significantly by the individual concentration of the filler as the results are found to be within the limit of experimental deviation. The 7.5H2.5B composite exhibited 27% and 46% improvement in the tensile strength in comparison to that of 7.5H and 10H composites, respectively. In the case of 5H5B composite, it showed enhanced mechanical strength of 8% and 41% compared to that of 10NB and 10H, respectively, while the 2.5H7.5B composite exhibited the corresponding enhancement of 7% and 39%.

It is observed from Fig. 4.6 (b) that the fracture strain of SMPU is 239±17%, and the reduction of failure strain of 4NB, 10NB, and 12.5NB composites is calculated to be 32%, 37%, and 48%, respectively, in comparison to that of pure SMPU. The reduction of strain at failure of the hydroxyapatite composites having the concentration of 2.5 wt%, 5 wt%, 7.5 wt%, and 10 wt% is observed to be 20.5%, 25.1%, 31.4%, and 43.9%, respectively, in comparison to that of pure SMPU. The failure strain of hybrid composites irrespective of the concentration of individual filler is observed to be 169±13%, and the results are found to be within the experimental deviation. A decreasing trend in failure strain is noted for all types of composites with an increase of filler content. It is also observed that the trend noticed on the fracture strain

is same as that of the tensile strength of the composites. The reason behind observing the above trends can be inferred from the study of fracture surface, which is done in the following section.

4.5.2.1 Morphological studies

The morphological features of the SMPU, and the fractured specimens of SMPU, and its composites after the tensile test are shown in Fig. 4.7. The cross-sectional view of the SMPU cut with a knife is shown in Fig. 4.7 (a). It is observed that the surface of the SMPU is smooth, and no impurities or pores are noticed. From the fractured sample of SMPU after the tensile test as shown in Fig. 4.7 (b), the tearing of SMPU along the multiple planes is observed. The direction of crack propagation is found to be along the converging direction of the crack planes. The morphology of the fractured surface of the 10H composite is shown in Fig. 4.7 (c,d), where several local crack growth planes and voids are observed. The nano-hydroxyapatite particle agglomerations having a size of up to 40 µm are also noticed in Fig. 4.7 (d). In addition, a wide cavity in the range of 20 µm is also seen between the polymer matrix and nano-hydroxyapatite after debonding. As the wetting of nHaP particles by the polymer matrix is observed to be incomplete, a wide gap between the polymer and nHaP particles is noticed. It is also observed that the local crack planes flow over the agglomerated particles, which act as an initiator for the fracture and also aid in their propagation. Similar observations are also noticed in the 12.5NB composite, and its morphological features are shown in Fig. 4.7 (e,f). It is observed that the $nBaSO_4$ particles are well dispersed on the SMPU. Agglomerated $nBaSO_4$ particles of size < 20 µm, small pores, and the interfacial gap of about 2 µm are also observed in the cross-section of the said composite. The filler particles act as a point of initiation of the crack and aid in the crack propagation, which are confirmed by the presence of particles over the crack growth direction as shown in Fig. 4.7 (f). The interfacial gap noticed between the polymer matrix and the filler irrespective of nHaP or $nBaSO_4$ is an indicative of the low interfacial

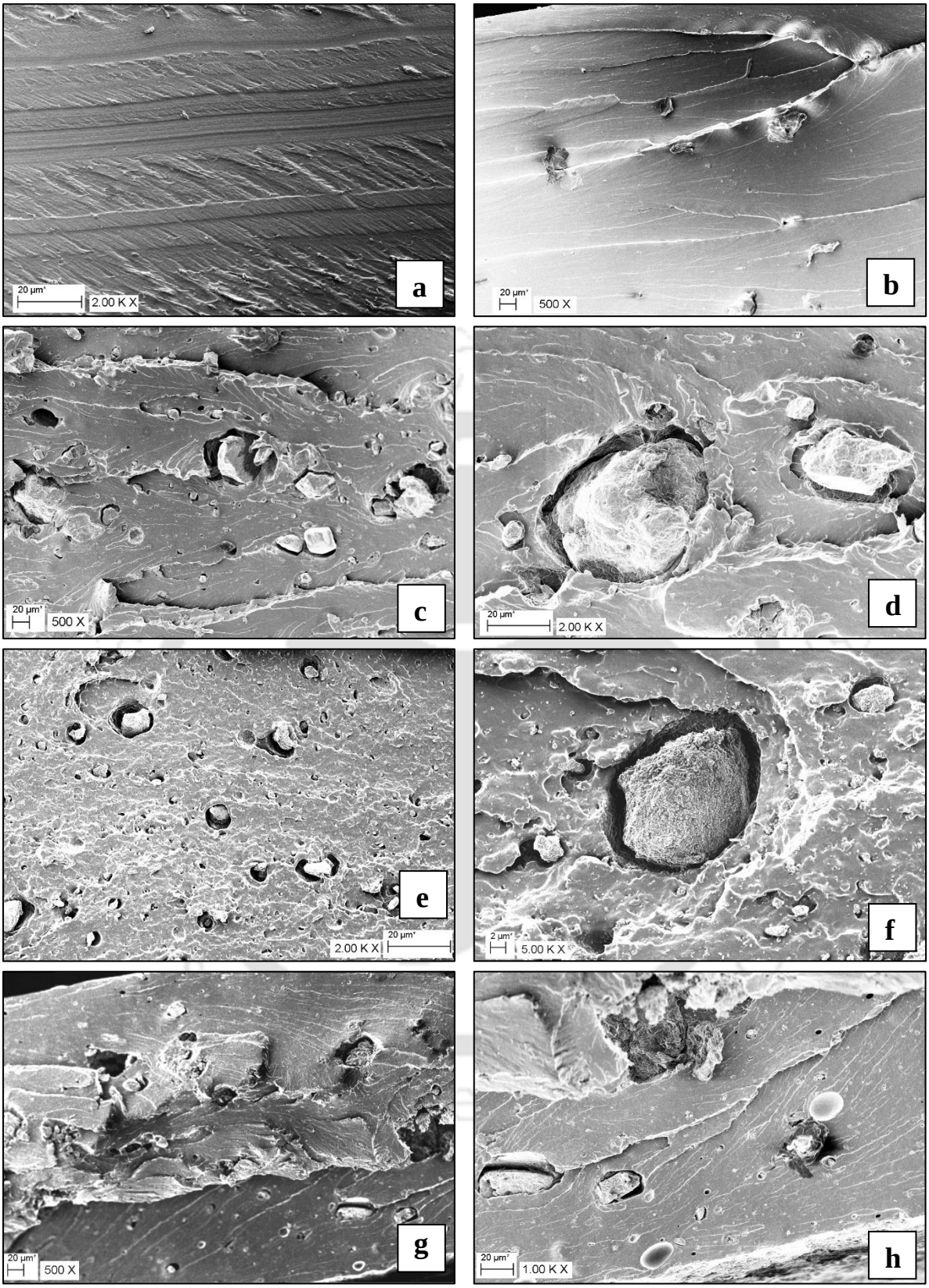

Fig. 4.7. Morphological features of SMPU and it composites after fracture: (a) pure SMPU cut by knife (Magnification= 2000x), (b) pure SMPU (500x), (c) 10H (Magnification= 500x), (d) 10H (Magnification= 2000x), (e) 12.5NB (2000x), (f) 12.5NB (5000x), (g) 7.5H2.5B (500x), (h) 7.5H2.5B (1000x)

adhesion and no chemical bonding between them. The fractured surface of 7.5H2.5B is represented in Fig. 4.7 (g,h), where multiple fracture planes, agglomerated nHaP particles on the crack line, and voids are observed. The fracture of SMPU under tensile load is found to be in the form of tearing. It is noted that the mechanical strength of n$BaSO_4$ composites is decreased in comparison to that of pure SMPU, and the fillers are found to assist the failure of composites. The agglomerated nanoparticles and the weak interfacial adhesion between the polymer and the nanoparticles led to decrease in the tensile strength of composites as they act as a source of crack and its propagation in the composites. With an increase of the concentration of filler, the nanoparticles start to aggregate due to van der Waals's force of attraction, leading to the reduction of the mechanical properties of the composites[129].

The above-discussed reasons are also applicable to the nanohydroxyapatite composite for the reduction of mechanical strength. Further, additional decrease in the mechanical strength in comparison to that of nano barium sulphate based composites could be due to its larger particle size [130], i.e., crystallite size of nano-hydroxyapatite particles is about 65 nm, whereas the same for the nano $BaSO_4$ is about 4 nm. In addition, the agglomeration of about <20 µm and <50 µm is observed for the nano barium sulphate and nano-hydroxyapatite composites, respectively, due to van der Waals force of attraction. As the hydroxyapatite (3.5 g/cm^3) has a lower density in comparison to that of barium sulphate (4.5 g/cm^3), the higher volume of HaP for the same weight fraction reduced the volume of polymer matrix, and it also led to the reduction of complete wetting of the fillers. The above phenomenon is expected to increase the number of defects, causing the reduction in the mechanical properties of the composites. In addition, the interfacial adhesive strength between the hydroxyapatite and the polymer matrix is observed to be further reduced in comparison to that of the nano barium Sulphate composites due to the increased interfacial gap noticed between the polymer and the filler.

In case of hybrid composites, where nHaP and nBaSO$_4$ nanoparticles are used to prepare the 10wt% composites, the total filler concentration of the composites played a vital role in the mechanical strength of the composites rather than the individual concentration of the constituents. As the failure criteria for both the fillers are same, there was no synergetic effect on the mechanical strength of the hybrid composites. The mechanical properties of all the composites are decreased by the addition of the nanoparticles of HaP and BaSO$_4$ compared to pure SMPU. Though the reduction of tensile strength and fracture strain noticed in the present study is found to be significant in comparison to that of pure SMPU, the composite material meets the requirement of the proposed application as the shear stress generated within the arteries due to blood flow is observed to be about 1-7 Pa, as reported by Paszkowiak *et al.* [131]. Thus, the reduced strength of the fabricated composites is not found to restrict its application and can be explored as embolic agents.

4.5.3 Thermomechanical studies

In this experiment, the samples are directly tested after keeping them in the open environment in order to study the effect of moisture on the glass transition temperature of the samples. Yang *et al.* [132] and Yu *et al.* [133] have reported that the presence of moisture in the samples decreased the glass transition temperature of SMPU. As the samples will be in contact with blood after its implantation, the effect of water on the developed SMPC is required to be studied.

The storage modulus of SMPU and its composites is shown in Fig. 4.8 and it is observed that the storage modulus of all the test samples in the glassy state started to decrease linearly with an increase of temperature, as confirmed through an inset (a). When the sample is further heated, it approaches the rubbery state, and there is a reduction of the storage modulus by two orders of magnitude, which is then converged into a plateau in the order of few MPa

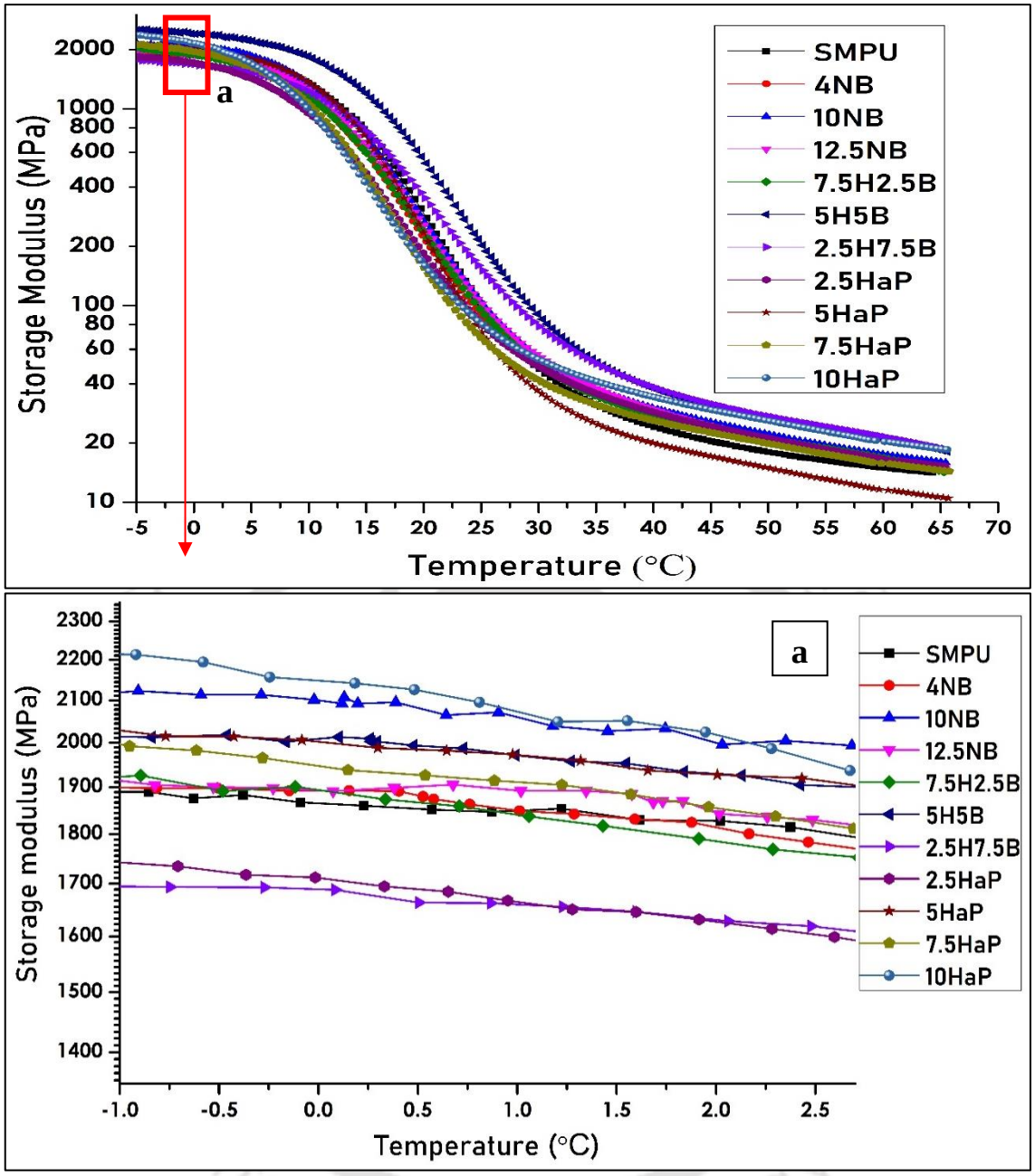

Fig. 4.8. Storage modulus of SMPU and its composites; (a) figure inset

irrespective of the type of sample tested in the present study. It is also noted that the addition of filler to the pure SMPU increased the storage modulus of the tested samples in the glassy state except for 2.5H and 2.5H7.5B composites. The highest storage modulus of the composites in the glassy state at -1ºC is observed to be 2209, 2119, and 2014 MPa for 10H, 10NB, and 5H5B composites, respectively.

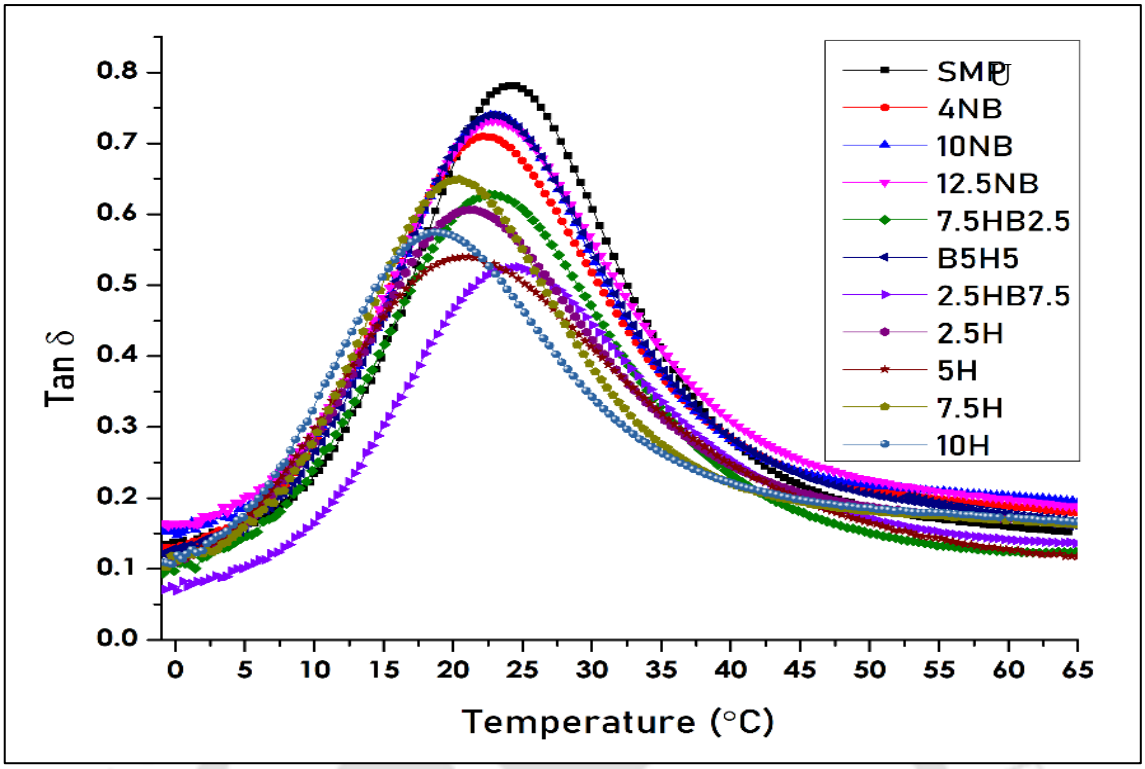

Fig. 4.9. Tan δ of SMPU and its composites

Table 4.3. Glass transition temperature, storage modulus at -1ºC, and peak height of tan δ of the SMPC

Sample	Glass Transition Temperature (°C)	Storage modulus (-1ºC) (MPa)	Peak height of tan δ
SMPU	24.0	1886	0.78
4NB	22.1	1897	0.71
10NB	22.7	2119	0.74
12.5NB	22.8	1903	0.73
2.5H	21.5	1737	0.61
5H	21.1	2017	0.54
7.5H	20.4	1985	0.65
10H	18.6	2209	0.57
7.5H2.5B	22.6	1921	0.63
5H5B	22.8	2014	0.74
2.5H7.5B	24.3	1694	0.53

The Tan δ or damping ratio of different samples tested in the present study is shown in Fig. 4.9. Tan δ denotes the ratio of loss modulus to storage modulus, and the peak position of tan δ represents the temperature of the phase change, i.e., glassy to rubbery state. The glass transition temperature of three different groups of composites and the pure polymer is noted from the peak value of the tan δ curve. The glass transition temperature, storage modulus at -1ºC and the peak value of tan δ are presented in Table 4.3.

The glass transition temperature of SMPU is observed to be 24ºC, whereas the manufacturer certified T_g is reported to be 35ºC. It is noted that the nano barium sulphate filler has little effect on the glass transition temperature of the SMPC as it is found to be in the range of 22.1-22.8°C for all concentrations of $nBaSO_4$ composites tested in the present study. However, a linearly decreasing trend is noticed in the T_g of the nano-hydroxyapatite composites with an increase of filler concentration, and a significant reduction of T_g is noticed for 10H composite, which is reported to be 18.6°C. The hybrid composites having 10 wt% filler irrespective of the individual filler concentrations showed the T_g in the range of 22.6-24.3°C, which is very close to that of the pure SMPU. It is observed from Fig. 4.9 and Table 4.3 that the height of the tan δ peak at glass transition temperature of the nanocomposites is decreased in comparison to that of pure SMPU. In case of nano barium sulphate composites, 4NB sample showed the highest decrease in tan δ, and the addition of filler increased the tan δ peak. Similarly, the peak of the nano-hydroxyapatite composites decreased compared to SMPU. Among the hybrid composites, 2.5H7.5B composite showed the least value of tan δ at the glass transition temperature.

The increase in storage modulus of the nanocomposites in the glassy state can be attributed to the filler, which acts as a hindrance for the movement of the polymer matrix. In the rubbery state, the polymer chains are mobile due to which the fillers cannot create much interferences in the flow of the polymer chains. This confirms the earlier findings that there is a weak

interfacial adhesion between the filler and the matrix as no load is transferred to the fillers. This is in accordance with our earlier finding on the mechanical properties.

The decrease in the peak of tan δ of the composites is due to decrease in the volume fraction of the polymer matrix by incorporating the fillers [134]. The nano-hydroxyapatite composites showed a decreased tan δ peak in comparison to that of the nano barium sulphate composites. This might be due to the higher volume fraction of hydroxyapatite in the composites compared to the barium sulphate, which prevented the movement of polymer chains.

As confirmed from the morphological studies, the nano barium sulphate composites have neither chemical bonding nor strong interfacial adhesion between the polymer and filler. Thus, the glass transition temperature of said composites is not found to be affected by the filler content. In case of nHaP composites, the decrease in glass transition temperature can be attributed to the low or no interfacial adhesion between the polymer and the filler, i.e., the SMPU has not wetted the nano-hydroxyapatite filler surface thoroughly, as confirmed from the microscopic studies. The presence of filler particles does not reduce the mobility of polymer chains, and on the contrary, it is increased with the presence of defects in the sample, leading to decrease in the T_g of composites as reported by Ash *et al.* [135]. The nanoparticles without bonding with the polymer acted like voids in the polymer matrix, leading to a void/polymer interface between the matrix and filler. These void/polymer interfaces act as s very highly mobile liquid- interaction zone. Thus, the composite exists as a porous system with a more mobile surface-like region around each nanoparticle. These mobile regions are expected to overlap with adjacent mobile regions with an increase of concentration of nanoparticles, which increases the mobility of bulk polymer leading to the reduction of T_g. The nano-hydroxyapatite particles acted as voids in the polymer matrix creating an effective void/polymer interface. As the concentration of nano-hydroxyapatite is increased in the polymer matrix, the voids/polymer interface between the polymer and nHaP are also increased leading to decrease in the T_g further.

It is observed that the filler concentration does not significantly influence the glass transition temperature of the hybrid composites. The presence of nano barium sulphate in the polymer matrix restricted the formation of an interfacial gap between the polymer-filler interface, even though nHaP particles were present. As the mobility of polymer chain is prevented significantly due to the combined effect of $nBaSO_4$ and nHaP in the composites, the T_g of 10wt% hybrid composites is found to be retained irrespective of the individual concentrations of the fillers.

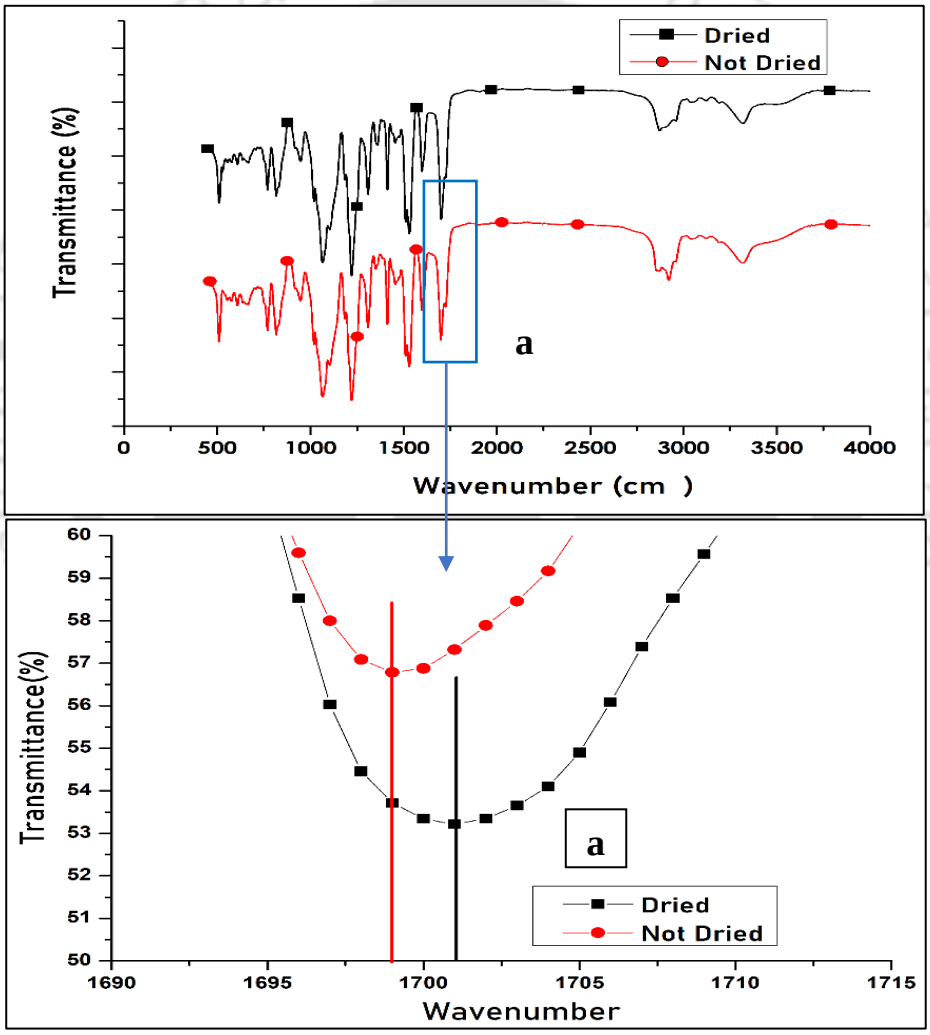

Fig. 4.10. FTIR spectroscopy of the dried and moisture absorbed SMPU samples

As the test samples are kept in an open environment before their testing, moisture absorption by the sample is expected to reduce its glass transition temperature, and it is also supported by Yang *et al.* [132] and Yu *et al.* [133]. Thus, the T_g of pure SMPU is observed to be lower than

the manufacturer's certified value. To validate the same, the SMPU sample, which is kept in an open environment, is dried at 140°C for 4 h and FTIR spectra of both the samples (dried and undried) are obtained, and these are shown in Fig. 4.10 in order to confirm the effect of moisture on the T_g of the test sample. The inset (a) of Fig. 4.10 shows that the C=O stretching region of the dried sample is shifted to a higher wavenumber in comparison to that of the non-dried sample. It is due to the fact that the absorbed water molecules reacted to form a double hydrogen bond with the hydrogen-bonded C=O groups [132]. This weakens the hydrogen bonding of the polymer resulting in decrease of the glass transition temperature of the composites.

4.5.4 Shape Recovery Studies

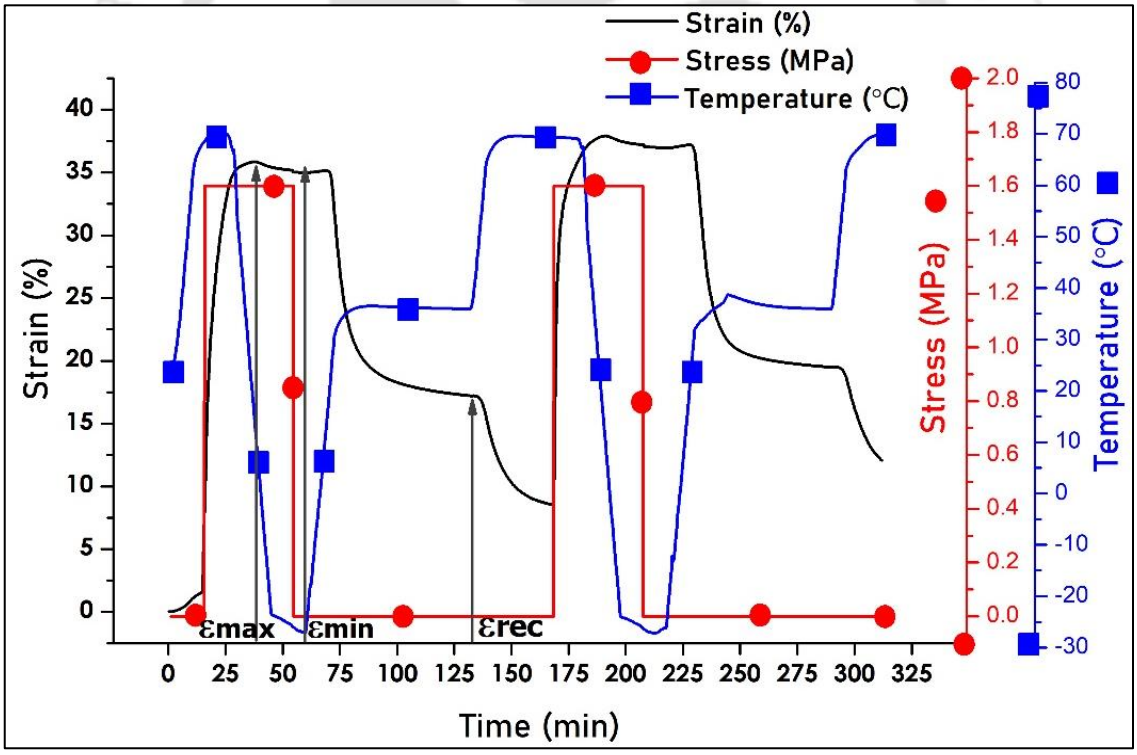

Fig. 4.11. Shape recovery studies on pure SMPU

A typical shape memory curve of an SMPU for the previously described thermal cycle is shown in Fig. 4.11. An initial elongation, i.e., expansion of the polymer, is observed after heating the sample to 70ºC. The polymer sample is further elongated when it is subjected to

the tensile force of 4N at the programming temperature of 70ºC leading to a maximum strain of ε_{max}. The sample temperature is retained for 5 min to reach its equilibrium condition. The sample is cooled to -20°C for fixing the secondary shape, and then the applied stress is removed. The polymer recovered marginally after unloading, and it is recorded as ε_{min}. Subsequently, the polymer is allowed to recover its permanent shape at 37°C and held for 1h. The strain in the sample at this stage is considered as ε_{rec}, and the sample is further heated to 70°C and held for 30 min. It is observed that a complete recovery of the SMPU is not achieved at 37°C and the sample is required to be heated till 70°C to increase its recovery. The above discussed steps are repeated for a second cycle. The shape fixity and shape recovery characteristics of all the test samples at 37°C and 70°C at different time intervals are recorded and showed in Fig. 4.12 and. Fig 4.13, respectively.

The shape fixity characteristics of the SMPU and its composites during 1st and 2nd cycle are shown in Fig. 4.12 and it is observed that the shape fixity of the samples obtained from both the cycles are at par with pure SMPU. It is inferred that the types of filler and their concentration irrespective of individual or combined form have minimal or no effect on the shape fixity of the composites except at 7.5H composite. This is due to the fact that the soft segments/switching segments of the SMPU, which is responsible for shape fixity is not affected by the addition of the fillers. However, the shape fixity of 7.5H composites is observed to be decreased significantly in comparison to that of pure SMPU. It might be due to the high concentration of the nano-hydroxyapatite fillers, which act as impurities due to the weak interfacial bonding with the polymer matrix, and it is also confirmed through the morphological studies. The said composite is further weakened during the loading cycle due to the elongation. The same is also observed in the fractured specimen of 10H composite during the initial elongation. Thus, the shape fixity and shape recovery characteristics of the 10H samples could not be studied and reported.

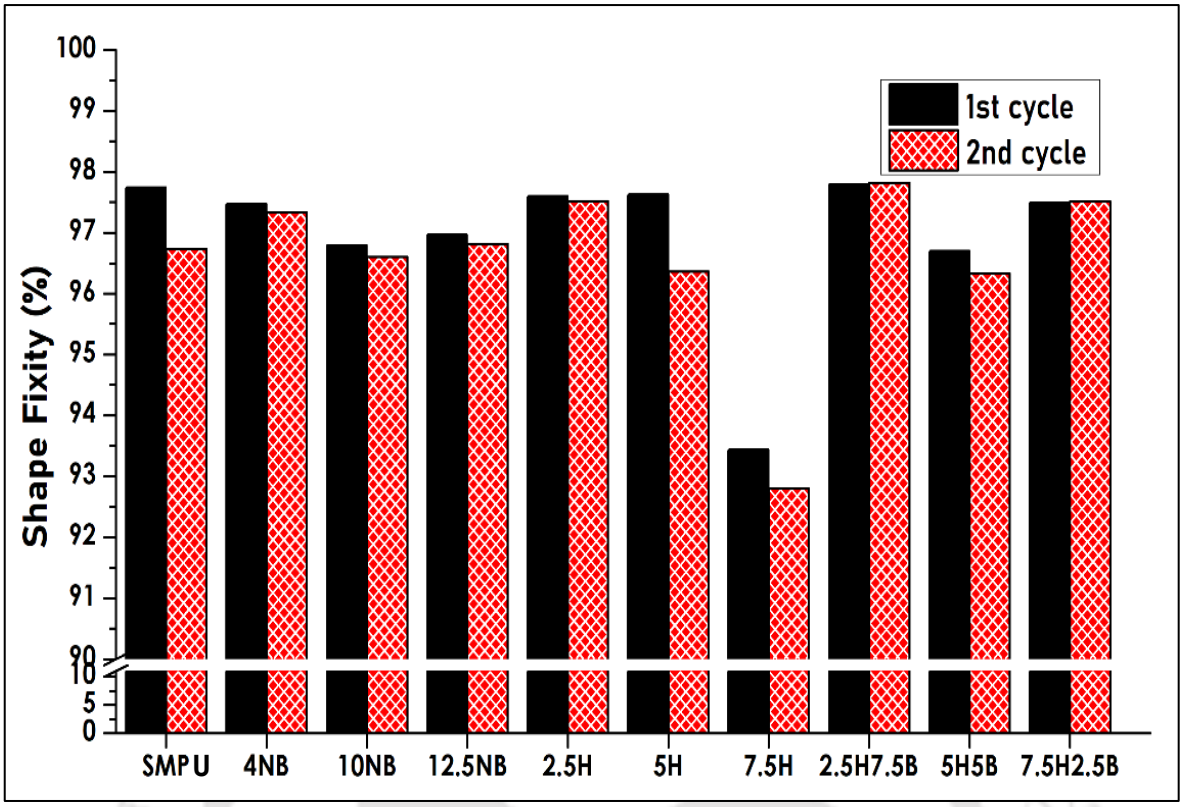

Fig. 4.12. Shape fixity characteristics of SMPU and its composites

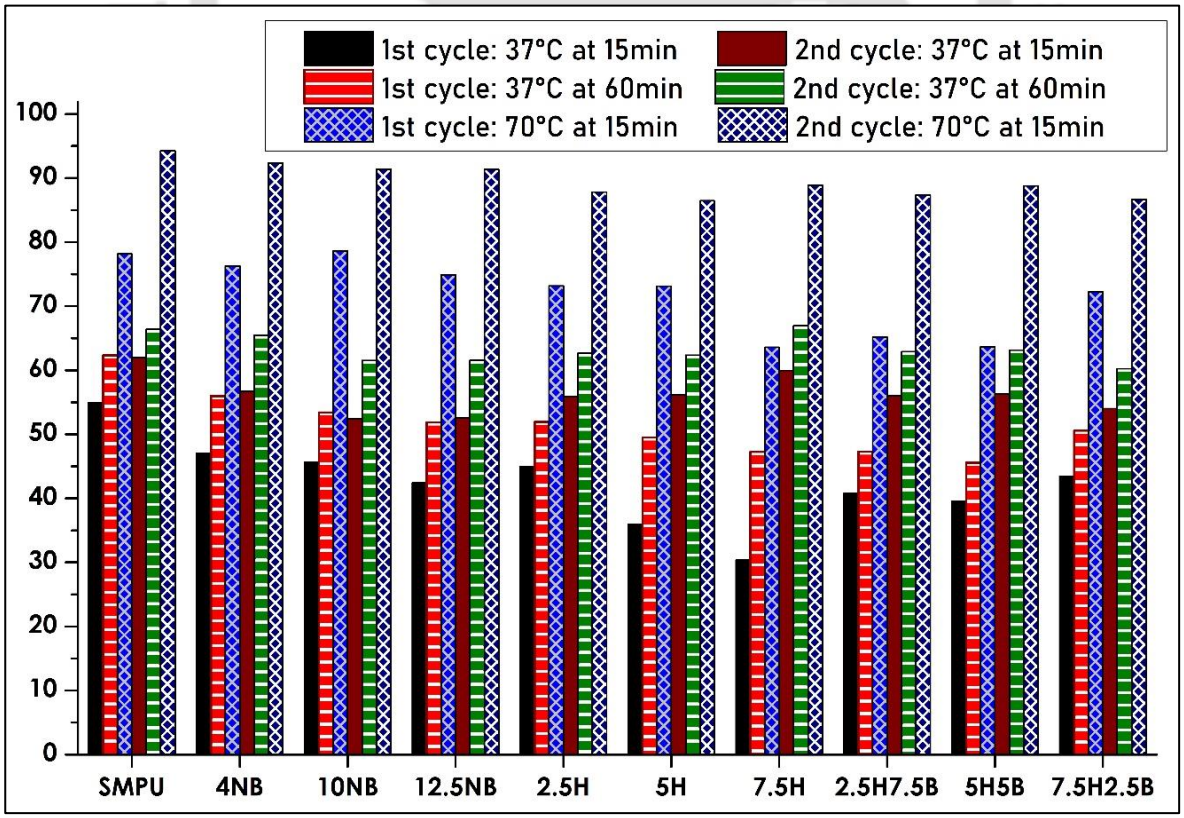

Fig. 4.13. Shape recovery characteristics of SMPU and its composites during the 1st and 2nd cycle

Fig. 4.13 shows the shape recovery characteristics of the SMPU and its composites, where a similar kind of trend in the shape recovery characteristics is observed for all the composites tested in the present study. It is observed from Fig. 4.13 that all the test samples recovered quickly during the initial 15min, and the recovery rate is drastically reduced with an increase of time. It is also noted that heating the sample to 70ºC increased the recovery of the polymer. The shape recovery during the second cycle is observed to have increased for all samples in comparison to the 1st cycle. The pure SMPU is observed to have the best shape recovery characteristics, and the addition of fillers is found to reduce the same. The shape recovery of the pure SMPU is observed to be 62.3% at 37°C after 1 h during the 1st cycle, which is increased to 78.2% at 70ºC after 15 min, and the respective values are increased to 66.4% and 94.3% during the 2nd heating cycle.

The shape recovery characteristics of the nano barium sulphate composites are decreased with an increase of filler concentration. The shape recovery of 4NB, 10NB, and 12.5NB samples at 37ºC after 1 h during the 1st cycle is decreased to 55.9%, 53.4%, and 51.9%, respectively, in comparison to 62.3% in case of SMPU and their corresponding shape recovery is increased to 76.3%, 78.6%, and, 74.9% at 70ºC after 15 min. The enhancement in shape recovery of samples during the 2nd cycle in comparison to their 1st cycle is observed to be 9.5%, 8.1%, and 9.7% for 4NB, 10NB, and 12.5NB, respectively at 37ºC for 1h and the corresponding enhancements at 70ºC after 15 min are observed to be 16.0%, 12.7%, and 16.5%.

A similar trend is observed for the nano-hydroxyapatite composite samples as their shape recovery during the 1st cycle at 37ºC after 1h is 52%, 49.5%, and 47.3% for 2.5H, 5H, and 7.5H, respectively, and the corresponding values in 2nd cycle are increased by 10.7%, 12.8%, and 19.7% to 73.2%, 73.1%, and 63.6%, when the samples are kept at 70ºC. The shape recovery of the above samples after being kept at 70ºC for 15 min in the 1st cycle is observed

to be 73.2%, 73.1%, and 63.6%, and these values are increased by 14.6%, 13.3%, and 25.3%, respectively in 2nd cycle. The shape recovery studies on the 10H composite could not be completed due to the generation of cracks and their propagation during the loading process leading to failure of the sample which is caused by the weak interfacial bonding between the matrix and the filler.

The hybrid composites showed improved shape recovery characteristics compared to that of the nano-hydroxyapatite composites and inferior characteristics compared to that of the $nBaSO_4$ composites. The shape recovery of 10wt% hybrid composites during the 1st cycle is observed to be 47.3%, 45.6%, and 50.6% at 37ºC after 1 h, and the corresponding values are increased to 65.2%, 63.4% and 72.2% at 70ºC after 15 min for 2.5H7.5B, 5H5B, and 7.5H2.5B composite samples, respectively. During the 2nd cycle, an improvement in shape recovery is observed to be 15.6%, 17.6% and 9.7% at 37ºC for 1h and 22.2%, 25.1%, and 14.5% at 70ºC after 15 min for the 2.5H7.5B, 5H5B, and 7.5H2.5B composites, respectively, in comparison to that of 1st cycle characteristics.

The decrease in shape recovery effect of the $nBaSO_4$ composites is due to the fact that the fillers acted as a hindrance during the polymer matrix recovery. As the concentration of filler is increased in the polymer, the magnitude of interference is increased, and also, the concentration of polymer matrix is reduced, which decreases the shape recovery characteristics of the composites [136]. A similar reason can also be attributed to decrease in shape recovery characteristics of the nano-hydroxyapatite composites, and the reduction of shape recovery is observed to be higher in comparison to that of $nBaSO_4$ composites. The low density of hydroxyapatite in comparison to $BaSO_4$ led to a larger volume of fillers in the polymer matrix for the same weight fraction. Thus, the reduction in the volume of polymer matrix, which is responsible for the shape memory effect, due to the addition of filler material decreased the overall shape memory characteristics of the composites. Also, the larger agglomerates and

defects in the composites observed during the morphological studies have increased the hindrance leading to further decrease in shape recovery characteristics.

It is confirmed from the morphological studies that neither the $nBaSO_4$ nor the nano-HaP particles showed the interfacial bonding with the SMPU matrix. Both the filler particles acted as a hindrance, and they have not assisted the shape recovery process in the composites. A drastic increase in the shape recovery characteristics is observed for all the samples during the second cycle, which can be attributed to the orientation of the polymer chains along the loading direction, lesser plastic deformation and decrease in the hysteresis loss [137]. This phenomenon is called as "training effect" as reported by Tobushi *et al.*[119] and Ohki *et al.* [120] , where a constant strain recovery is noticed after several cycles of training.

As observed from Fig 4.13, the SMPU and its composites are not fully recovered at 37°C even after keeping the sample for 1h, though the glass transition temperature of the polymer as per the datasheet provided by the manufacturer is reported to be 35°C. Also, the shape recovery of all the test samples is observed to be increased when the samples are heated to 70°C. This partial recovery of the SMPU and its composites at 37°C can be attributed to their programming temperature of 70°C. This phenomenon is also observed by Xie [138], who labeled it as multistage recovery and attributed to the wide range of the transition temperature. The SMPU MM3520 has a broad thermal phase transition ranging from 0°C to 60°C as observed from Fig. 4.9. The broad thermal transition can be regarded as the collective contribution of numerous infinitely sharp transition regions continuously distributed in the broad temperature range. Each of these sharp transitions regions can be viewed as an individual memory elements (IMEs) corresponding to an infinitely sharp transition temperature. Thus, at any programming temperature, only the IMEs with their T_{sw} below the particular programming temperature are activated for the shape memory function. Thus, in our case at recovery temperature of 37°C, only the IMEs below that particular temperature are activated leading to the partial recovery.

Finally, on reaching the recovery temperature of 70°C, all the IMEs are activated, which leads to increased recovery of the SMPU and its composites.

In summary, the filler materials added in the SMPU are found to decrease the recovery of SMPC from its original shape as they restrict the free movement of polymer chains during the heating process. The test material is observed to have higher recovery during the 2nd heating cycle in comparison to 1st heating cycle. During the 2nd heating cycle, the SMPC has a higher tendency to return to its original dimension, which increases the reliability of the SMPU and its composites to return to a predetermined shape.

4.5.4.1 Effect of programming temperature on the shape recovery of the SMPU

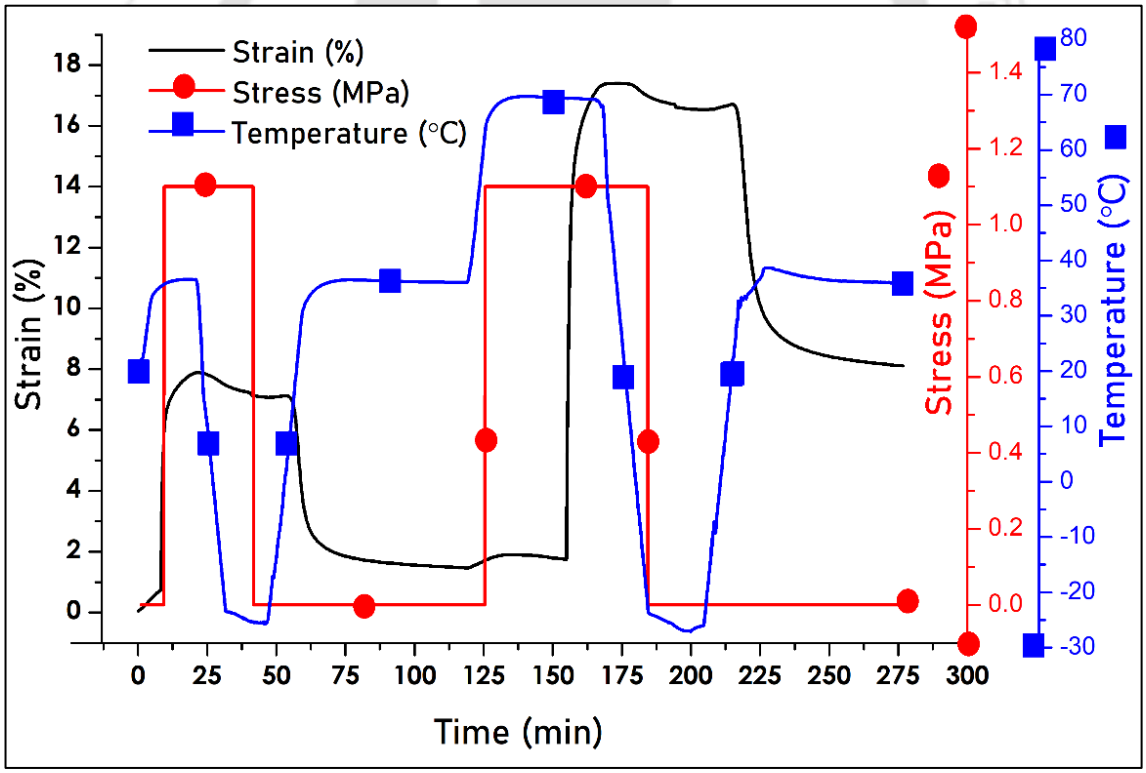

Fig. 4.14. Shape recovery characteristics of SMPU at the programming temperature of 37°C

As evident from the previous study, programming temperature plays an important role in the shape recovery of the SMPU and its composites. In order to study the macroscopic effect of programming temperature on the shape recovery characteristics of SMPU and its

composites, the programming temperature of 37°C and 70°C is chosen, and the shape recovery characteristics are studied in detail. The programming temperature of 37°C is chosen to keep it identical to recovery temperature, which is the normal body temperature. Fig. 4.14 shows the shape recovery characteristics of SMPU at the programming temperature of 37°C. It is observed that the recovery of the SMPU is completed at 37°C, and no further recovery is noticed with an increase of temperature, when the programming temperature is kept at 37°C. On the contrary, the expansion of the polymer is observed with a rise in temperature. However, the SMPU and its composites recover in stages, when the programming temperature is maintained at 70°C.

The effect of the programming temperature on the recovery time of the test sample is shown in Fig. 4.15, where the recovery of the SMPU at 37°C at different intervals of time for the programming temperature of 37°C and 70°C is shown. The recovery of SMPU is observed to be 31% and 1.6% at the programming temperature of 37°C and 70°C, respectively, while heating the sample to 37°C at 5°C/min. The recovery after 5 min at 37°C is observed to be an additional 34% for the SMPU with the programming temperature of both 37°C and 70°C. The corresponding recovery is observed to be decreased to 5.9% and 13.2% during the next 5 min. During the 10 to 15 min time interval, the recovery of the SMPU for the programming temperature of 37°C and 70°C is 2.8% and 5%, respectively. The better recovery of the SMPU for the programming temperature of 37°C in comparison to 70°C at same recovery temperature of 37°C can be explained by the IME theory as reported by Xie [138]. The IMEs which are activated at the programming temperature of 37°C, recover completely at the recovery temperature of 37°C, whereas the elements which are activated at programming temperature of 70°C, could not recover at 37°C.

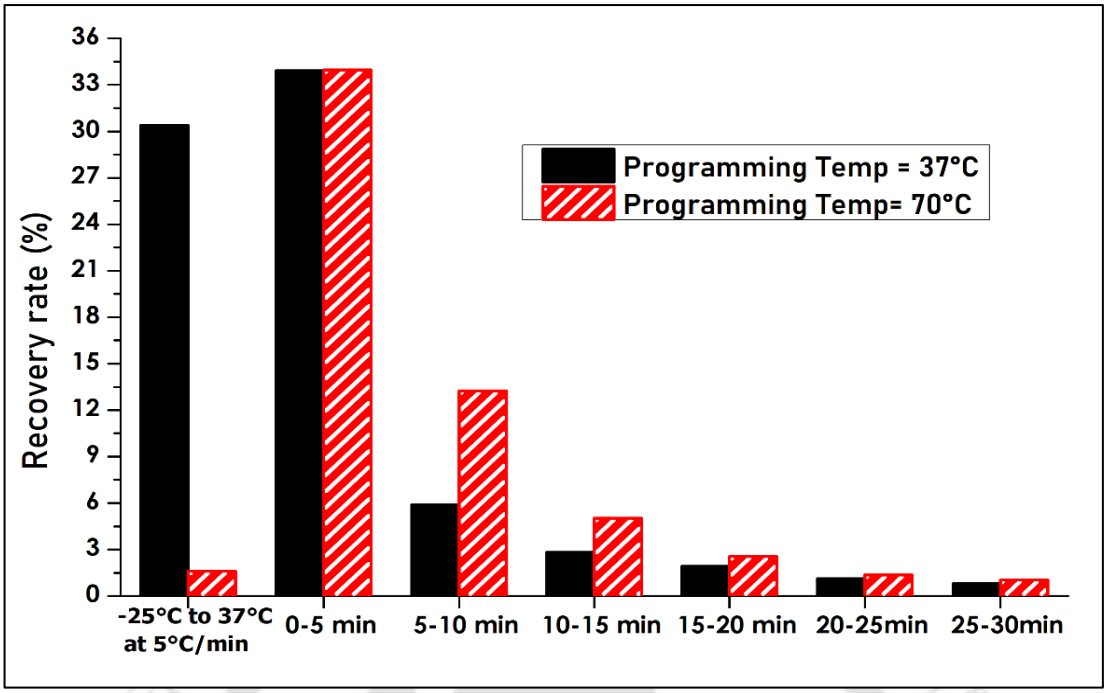

Fig. 4.15. Recovery of SMPU at 37°C for the programming temperature of 37°C and 70°C during the 1st cycle at different time intervals

The faster rate of recovery of the SMPU at the programming temperature of 37°C than at 70°C may be related to recovery stress, where the higher recovery stress leads to a faster recovery of the SMPU. Xie [138] also reported that the maximum recovery stress appears at a temperature roughly the same as the corresponding programming temperature. As the recovery temperature is equal to the programming temperature of 37°C, a faster recovery is observed.

The lower programming temperature increased the total recovery of the sample, and it also leads to a higher recovery at a lower temperature. The faster recovery rate might be a cause of concern during the medical procedure. Thus, the recovery of the test sample might be delayed by the higher programming temperature for the proposed application while compromising on the total recovery of the sample. It is noted from the results that the programming temperature can be tuned to increase the recovery rate of the sample, i.e., whenever the time required for recovery is to be decreased, the programming temperature may be lowered or vice versa.

4.5.5 Radiopacity Studies

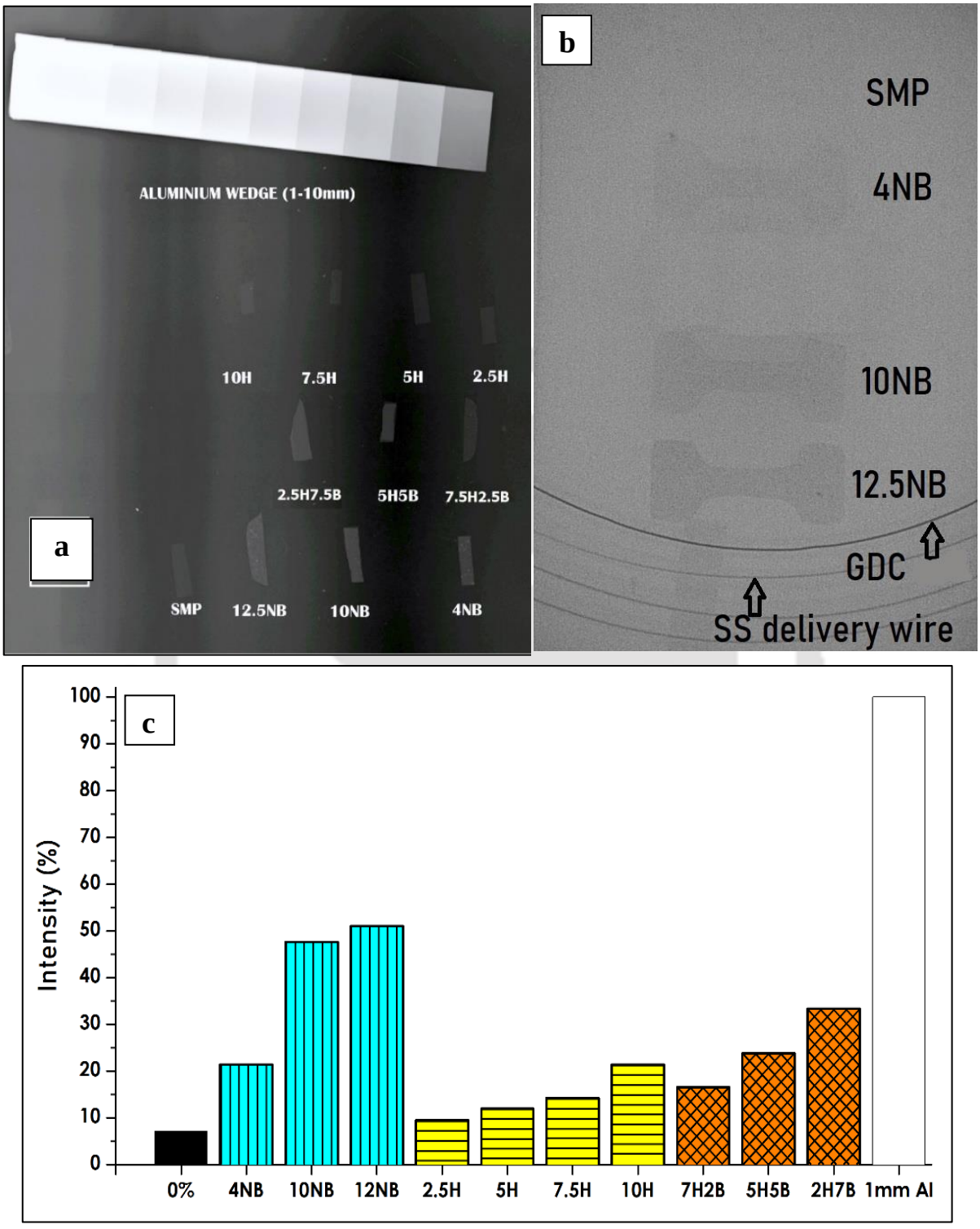

Fig. 4.16. (a) Radiograph of the tested samples with Aluminum wedge; (b) Radiograph of the tested samples with GDC; (c) Intensity of radiopacity of different materials tested in the present study in comparison to 1mm thick Aluminum wedge

The radiographic image of the tested samples in comparison to Aluminum wedge is shown in Fig. 4.16 (a). The $nBaSO_4$ composites in comparison to GDC on a digital subtracted angiography (DSA) are presented in Fig. 4.16 (b). It is observed from Fig. 4.16 (b) that the 10NB and 12.5NB samples are adequately radiopaque, visible, and produce intensity identical to stainless steel delivery wire, which is not as bright as the GDC. The SMPU is not visible under DSA. The pixel intensity of the samples against 1mm Aluminum wedge is shown in Fig. 4.16 (c). It is observed that the radiopacity of composites is increased with the concentration of filler materials irrespective of type or combination of reinforcements used. The nano barium sulphate composites showed the highest increase in intensity, while hydroxyapatite composites showed the least. The hybrid composites showed increased opacity with an increase of nano barium sulphate concentration.

The increase in radiopacity is related to the higher atomic number of Barium and specific weight of barium sulphate (4.5g/cc) in comparison to that of hydroxyapatite (3.16g/cc). The radiopacity of the hybrid composite depends on the concentration of the nano barium sulphate as it played a dominant role in the radiopacity. Though the weight concentration of hydroxyapatite and barium sulphate is the same in case of 5H5B, its X-ray attenuation is similar to that of 4wt.% nano barium sulphate. This can be attributed to the higher X-ray attenuation characteristics of barium sulphate, which overshadows that of hydroxyapatite. The increased radiopacity of the SMPC makes it suitable for use as an embolic agent for interventional radiology techniques.

4.6 SUMMARY

In summary, the SMPU-$nBaSO_4$, SMPU-nHaP, and hybrid composites containing $nBaSO_4$, and nHaP as filler are fabricated. The mechanical, thermal, shape memory characteristics and radiopacity of the composites are studied and compared with that of pure SMPU. Though the

addition of the fillers degraded the mechanical properties and shape recovery characteristics of the SMPU, these are not restricting to explore the composites for the proposed applications. The 10wt% and 12.5wt% nano barium sulphate SMPC have adequate radiopacity, which are proposed to be used for minimally invasive surgeries. However, the mechanical properties of 10wt% nano $BaSO_4$ composite are better than 12.5wt% composite. Further, to ensure interconnectivity among the pores and complete salt leaching, the least amount of filler should be added to keep the maximum amount of porogen in the polymer matrix. Hence, the 10wt% of nano barium sulphate is selected as the appropriate concentration for the substitution of tungsten in the novel processing technique discussed in previous chapter. The advantages of adding nanohydroxyapatite fillers in the SMPU need to be evaluated based on biocompatibility studies before they are projected for potential applications.

CHAPTER 5: PRELIMENARY BIOCOMPATIBILITY EVALUATION OF THE SHAPE MEMORY POLYMER COMPOSITES

5.1 INTRODUCTION

The newly developed embolic material must be tested according to ISO 10993 [9] to ensure their biocompatibility and efficacy as embolic agents, which are classified as permanent and blood-contacting implant devices. This classification has the highest number of criteria on different biological effects (cytotoxicity, sensitization, irritation, acute systemic toxicity, pyrogenicity, subchronic toxicity, genotoxicity, implantation, hemocompatibility, and carcinogenicity) that are required to be tested before they can be considered for testing in animals followed by human beings. In this chapter, the preliminary biocompatibility studies on the developed embolic agents are reported. Among the recommended tests, cytotoxicity is preferred as a pilot test as it is an important indicator on the effect of the medical device on the body cells. The cytotoxicity test is a screening test that uses tissue cells to observe the cell growth and reproduction of the same to evaluate the toxicity of the material. The test is simple, fast, and has high sensitivity. It is performed under *in vitro* conditions and without the requirement of any direct material from animals or human beings. There are three types of cytotoxicity tests, as stated in ISO 10993-18 [9]: extract, direct contact, and indirect contact tests. In general, the extract test or MTT assay test is the most commonly used test, and it is highly accurate. It is suitable for detecting the toxicity of soluble substances of medical devices and is usually consistent with the results of animal toxicity tests [139]. The direct contact assay is the most sensitive for testing the cytotoxicity of the medical devices. However, it is unsuitable for some medical devices and less dense devices as they are expected to float on the medium[140]. The indirect contact test consists of the agar overlay assay and molecular filtration method. Agar overlay assay is suitable for the medical devices that can leach toxic

substances, but this is a semi-quantitative method and is susceptible to subjective factors [139]. The molecular filtration method is simple, rapid, sensitive, and reliable for evaluating the toxic components of small molecular weight medical devices but it has few shortcomings. In this work, the cytotoxicity of the materials is evaluated on human lung cell line, L132 and human keratinocyte cell line, HaCaT using a 3-[4,5-dimethylthiazole-2-yl]-2,5-diphenyl tetrazolium bromide (methyl thiazolyl tetrazolium; MTT) assay.

The interaction of blood with a material triggers a complex series of events starting with protein adsorption that can catalyze, mediate, or moderate the subsequent biological responses of platelet adhesion and activation, coagulation, and thrombosis. An important parameter used to evaluate the hemocompatibility of a material is the adsorption of blood plasma proteins on the surface. Blood contains hundreds of proteins with a wide range of biological functions and activity, and are present in vastly different concentrations. Albumin, immunoglobulins, and fibrinogen are the most abundant proteins in blood. Albumin adsorption on a surface inhibits thrombus formation, while fibrinogen plays a central role in the processes of hemostasis and thrombosis by facilitating the adhesion and aggregation of platelets. Therefore, a higher ratio of albumin to fibrinogen (A:F) is highly desirable for a lower platelet adhesion, which reduces the tendency for thrombus formation. In order to evaluate the thrombus formation due to the embolic agents, the adsorption of albumin and fibrinogen on the surface of the material is studied and reported.

5.2 MATERIALS and METHODS

5.2.1 Sample Selection

The samples selected for the biocompatibility test are SMPU, 10H, 12.5NB, 5H5B, and 3D printed porous Tungsten composite and their fabrication details have been already discussed

in chapter 3 and chapter 4. The polymer composite with highest concentration of the fillers is chosen for testing.

5.2.2 Cell Culture

The human lung cell line L132 and human keratinocyte cell line HaCaT are procured from National Centre for Cell Science, Pune, India and cultured in Dulbecco's Modified Eagle Medium (DMEM) media (M/s Gibco, Mumbai, India; Cat No:121000-046, 10X1L) supplemented with 10% fetal bovine serum (FBS) (M/s Gibco Mumbai, India; Cat No: 10270106) and 1% Pen Strep (M/s Gibco, Mumbai, India; Cat No: 15140122). The cells are maintained at 37°C in a CO_2 regulated incubator in a humidified 95% air/5% CO_2 atmosphere.

5.2.3 MTT Assay

MTT assay is performed to assess the effect of SMPU, and its composites on the proliferation of cells. Samples are disinfected by soaking them in 70% ethanol solution and exposure to UV light (10 min on each side). The polymer samples are dissolved in DMSO with the desired quantity to produce the required concentration of samples (1, 5, 10 µg/ml). The L132 and HaCaT cells are harvested using 0.05% trypsin-0.02% EDTA solution (Gibco, Mumbai, India; Cat No: 25200072) and seeded in 96-well plates (2000 cells/100µl in each well). After 24h of incubation, the cells are treated with various concentrations of polymers (0, 1, 5, 10 µg/ml). MTT assay (M/s Sigma Aldrich, Bengaluru, India, Cat No: M2128-5G) is performed at 0 h, 24 h, 48 h, and 72 h. The 10 µl of 5 mg/ml MTT solution is added to each well and incubated for 2h. Following the incubation, the culture media is removed, and 100 µl of DMSO (M/s Merck Life Science Pvt. Ltd., Bengaluru, India) is added to all the wells and incubated at RT for 1 h to dissolve the MTT-formazan product. Finally, the absorbance of the colored solution is measured with a microplate reader (Make: Infinite 200 PRO multimode reader, Make: M/s Tecan, Männedorf, Switzerland) at 570 nm. Inhibition of proliferation is

calculated after normalizing with 0 h absorbance, keeping the absorbance of untreated control as 100%.

5.2.4 Quantification of fibrinogen and albumin adsorption: Micro bicinchoninic acid (mBCA) assay

In this assay, the adsorption of two human blood proteins, namely human fibrinogen (>95% purity, affinity-purified) and human serum albumin (>98% purity, lyophilized) procured from M/s Sigma-Aldrich (Bengaluru, India), on the developed SMPC is studied. Stock proteins are prepared at 10% (albumin 4.4 mg/ml; fibrinogen 0.25 mg/ml) of the proteins' approximate human plasma concentrations (albumin 35 – 50 mg/ml; fibrinogen 1.5 - 4.5 mg/ml). In addition, an albumin and fibrinogen concentration of 2.5 mg/ml each is prepared to compare albumin and fibrinogen adsorption at equal concentrations. Uncoated silicon and tissue-culture polystyrene (TCPS) are also included as controls to ensure that the components of the testing platform did not elicit an unfavorable blood response. All materials are cut into 14 mm x 14 mm squares, except the TCPS well-plate controls. The above dimension is chosen to perfectly fit them into 24-well tissue-culture polystyrene (TCPS) plates. The samples are disinfected by soaking in 70% ethanol solution and exposure to UV light (10 min on each side) and then rinsed in sterile PBS. After placing them in the 24-well plate, the samples are incubated in distilled water using an orbital shaker incubator at 37℃ for 1 h, rinsed twice with distilled water, and blown dry with nitrogen. Then, each sample is incubated in 0.5 ml of protein solution for 24 hours on an orbital shaker incubator at 37℃. After incubation, the samples are rinsed with calcium, magnesium-free phosphate-buffered saline (CMF-PBS) to remove non-adsorbed proteins, and the protein adsorption is measured using the micro BCA (bicinchoninic acid) kit (M/s ThermoFischer Scientific, Mumbai, India Cat No. 23225) as per the manufacturer's protocol. Protein adsorption is calculated using standard calibration curves prepared using fibrinogen and human serum albumin protein standards. For a given

experiment, three samples of all test materials are studied at each protein dilution. Statistical differences between the materials are evaluated separately for albumin and fibrinogen.

5.2.5 Statistical analysis

The experimental data are analyzed for statistical significance by one-way analysis of variance in probability. The data are considered to be significant if a p-value is less than 0.05. The data are denoted as mean ± SD (n = 3).

5.3 RESULTS & DISCUSSION

5.3.1. Cytotoxicity test

Fig. 5.1 shows the results of the cytotoxicity test on SMPU, 12.5NB, 10H, 5H5B, and 3D printed porous Tungsten composite using MTT cell proliferation assay in L132, and HaCat cells. It is well known that the cellular proliferation is decreased significantly compared to control if the materials exerted any cytotoxicity. The proliferation of the L132 cell line in different concentrations of SMPU and its composites (1µg/ml, 5µg/ml, and 10µg/ml) incubated for 24, 48, and 72 hours are presented in Fig. 5.1 (a-c), and the corresponding data for HaCat cell are shown in Fig. 5.1 (d-f). Each sample is compared with a control at the same conditions, whose proliferation is taken as 100%. The samples, which have been found to have a statistically significant difference from the control, have been marked with a star.

It is observed from Fig 5.1 (a) that the cell proliferation in the SMPU (1µg/ml) is increased with time, and the highest proliferation of 126.8% is seen at 48 hours, which is decreased to 108% after incubating for 72 hours. However, the cell viability is above the proliferation of control and is found to be not statistically significant. Similar results are also observed for the SMPC with an increased proliferation after 24 and 48-hour studies compared to SMPU. However, it is decreased after 72 hours. The 12.5NB composite exhibited the highest increase

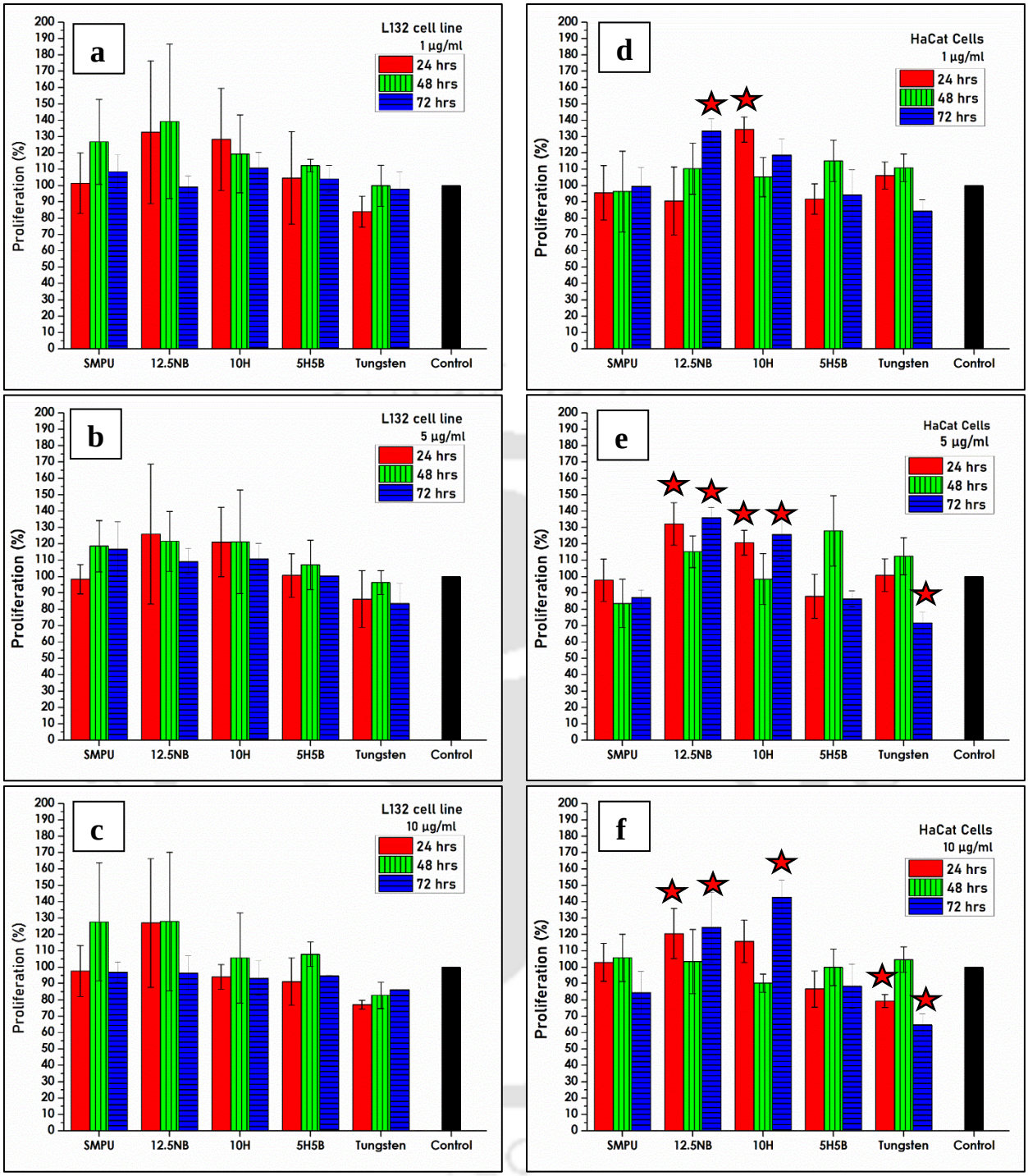

Fig. 5.1. Proliferation (%) of L132 and HaCaT cells at 24, 48, and 72 hr in presence of different extract concentrations of SMP, 12.5NB, 10H, and 5H5B using MTT assay: L132 cells (a) 1µg/ml, (b) 5 µg/ml, (c) 10 µg/ml; HaCat (d) 1µg/ml, (e) 5 µg/ml, (f) 10 µg/ml. Values represent mean ± SD from experiments performed.

(★: $p < 0.05$ is a significant change in cell proliferation compared to control)

in proliferation of 132.7% and 139.2% for 24 and 48 hours, respectively. However, the 3D printed porous Tungsten composite showed the least proliferation of 84.0%, 99.95%, and 98.0% at 24, 48, and 72 hours, respectively, but these are judged to be insignificant during the statistical analysis. Thus, the SMPU MM3520 at a concentration of 1 µg/ml showed excellent cell viability. Further, the addition of nano barium sulfate, nano-hydroxyapatite, and a mixture of the same nanoparticles did not affect the cells. A similar trend is also observed in the sample concentrations of 5 µg/ml and 10 µg/ml in L132 cell lines, as seen from Fig. 5.1 (b) and Fig. 5.1 (c), respectively. An increase in the cell proliferation at 5µg/ml is observed in nano barium sulphate and nano-hydroxyapatite filled composites by 27.5% and 22.7%, respectively, compared to SMPU at 24 hours and the corresponding values at 48 hours are 3% and 2.7%. The proliferation at 72 hours is decreased to 109.3%, 110.9%, and 100.3% for 12.5NB, 10H, and 5H5B, respectively, compared to 116.7% in SMPU. Again, the tungsten composites showed a decrease in cell survival at 86.3%, 96.4%, and 83.54% at 24, 48, and 72 hours, respectively. In general, an improved proliferation is noticed at 10 µg/ml concentration by 20.3%, 4.4%, 0.13%, 6.5% and 10.1% in SMPU, 12.5NB, 10H, 5H5B, and porous Tungsten composite, respectively, in 48 hours in comparison to that of 24 hours. The cell viability in SMPU, 12.5NB, 10H, 5H5B, and porous Tungsten composite after 72 hours compared to 24 hours is changed by +18.3%, -16.67%, -10.2%, -0.35%, and -2.8%, respectively. It is also noted that the porous Tungsten composite has lower cell viability than the control sample in all the cases with a minimum of 83.5% at 72 hours. The MTT assay revealed no cytotoxicity by the exposure of different concentrations (0, 1, 5, 10 µg/ml) of polymers at different periods, i.e., 24, 48, and 72 h in L132 cells. Although, in some cases, change in percentage of proliferation compared to control is observed, but it is not found to be significantly high or low in any of the conditions. All the samples are not found to elicit any cytotoxic response under any experimental conditions. It indicates that these test samples can be considered to be

biocompatible and may be tested in animals before they can be explored for the desired application.

The cytotoxicity studies on the HaCat cell lines showed a similar trend, as can be seen from Fig. 5.1 (d-f). At 1 µg/ml of polymer concentration, the cell proliferation after 24 hours in SMPU is 95.5%, which is decreased to 90.6%, and 91.9% in 12.5NB and 5H5B, respectively, but increased significantly to 134.3% and 106.1%, respectively, for 10H and porous Tungsten composite. At 48 hours, the SMPU, 12.5NB, 5H5B, and porous Tungsten composite showed increased cell proliferation compared to 24 hours by 0.8%, 9.7%, 13.4%, and 4.2%, respectively, while it is decreased in 10H by 29.4%. The least cell viability of 84.3% at 72 hours is observed in porous Tungsten composite, while a significant increase in proliferation is noted in 12.5NB. The 5 µg/ml concentration of 12.5NB, and 10H composites after 24 hours showed statistically significant cell growth of 132.1, and 120.7%, respectively, and the corresponding values are increased to 135.8%, and 125.8% after 72 hours, as observed from Fig. 5.1 (e). After 72 hours of incubation in HaCat cells, the porous Tungsten composite showed a statistically significant decrease of 28.3% in the cell numbers compared to control. The cell proliferation at the sample concentration of 10 µg/ml, as presented in Fig. 5.1(f), followed the same trend as observed in 5 µg/ml. The 12.5NB and 10H composites after 24 hours showed cell proliferation of 120.5% and 115.9%, respectively, and the corresponding values are increased to 124.4% and 142.9%, respectively after 72 hours. The SMPU after 24 h, 48 h, and 72 h exhibited a cell growth of 103.0%, 105.7%, and 84.5%, respectively and the corresponding values for 5H5B are 86.6%, 99.9%, and 88.4%, respectively. The composites 12.5NB, 10H, and 5H5B showed a better proliferation after 72 hours compared to 24 hours by 3.8%, 27%, and 1.8%, respectively. A significant decrease in the cell viability of 79.3% and 64.7% is observed in the porous Tungsten composite at 24 and 72 hours,

respectively. A proliferation within 83.5-105.7% is observed for SMPU in the MTT assay test in HaCat cells.

It can be concluded that SMPU had no detrimental effects on the growth of HaCat cells. All the SMPC tested under the different types of experimental conditions showed no cytotoxic behavior and can be considered for the desired application after systematic animal studies as per the established protocol. However, the porous Tungsten composite was the only sample that showed a statistically significant decrease in cell viability and elicited cytotoxic characteristics at a higher concentration, which made it unfavorable for the proposed application at 7wt% Tungsten concentration.

The above results of SMPU MM3520 are expected and in agreement with the previous literature, where the cytotoxicity of the foamed cousin of MM3520, CHEM 3520, and CHEM 5520 after plasma sterilization is tested on L929 cells by MTT colorimetric assay, and they are found to have good response [84]. Similar results are also observed in the cytocompatibility test of MM-4520, which is from the same family as MM 3520 evaluated using the human osteosarcoma cell line MG63 (ECACC No. 86051601) [141] and others. The addition of nano barium sulphate is not found to cause any cytotoxic response as expected. Barium sulphate is a tried and tested inert, and biocompatible material, which is already being clinically used. Further, there was no reaction between the SMPU and the nano barium sulphate to form any toxic residuals. Similar insight can also be drawn for the nano-hydroxyapatite composites. Hydroxyapatite is a biocompatible material, and as expected, it did not create any hindrance to cell growth. Though tungsten is being used in many medical devices, corrosion of implanted tungsten devices under *in vivo* conditions has been observed in many instances [142]. A similar response is observed in this study, and hindering its use in the present work.

5.3.2 Quantification of fibrinogen and albumin adsorption: micro bicinchoninic acid (mBCA) assay:

Fig. 5.2 shows the results of the micro BCA (bicinchoninic acid) protein assay used to determine the albumin and fibrinogen adsorption on the SMPU and its composites. Albumin adsorption on the samples at protein concentrations of 4.4 vs. 2.5 mg/ml is presented in Fig. 5.2 (a). The adsorption of albumin concentration at 2.5 mg/ml for SMP, 12.5NB, 10H, and

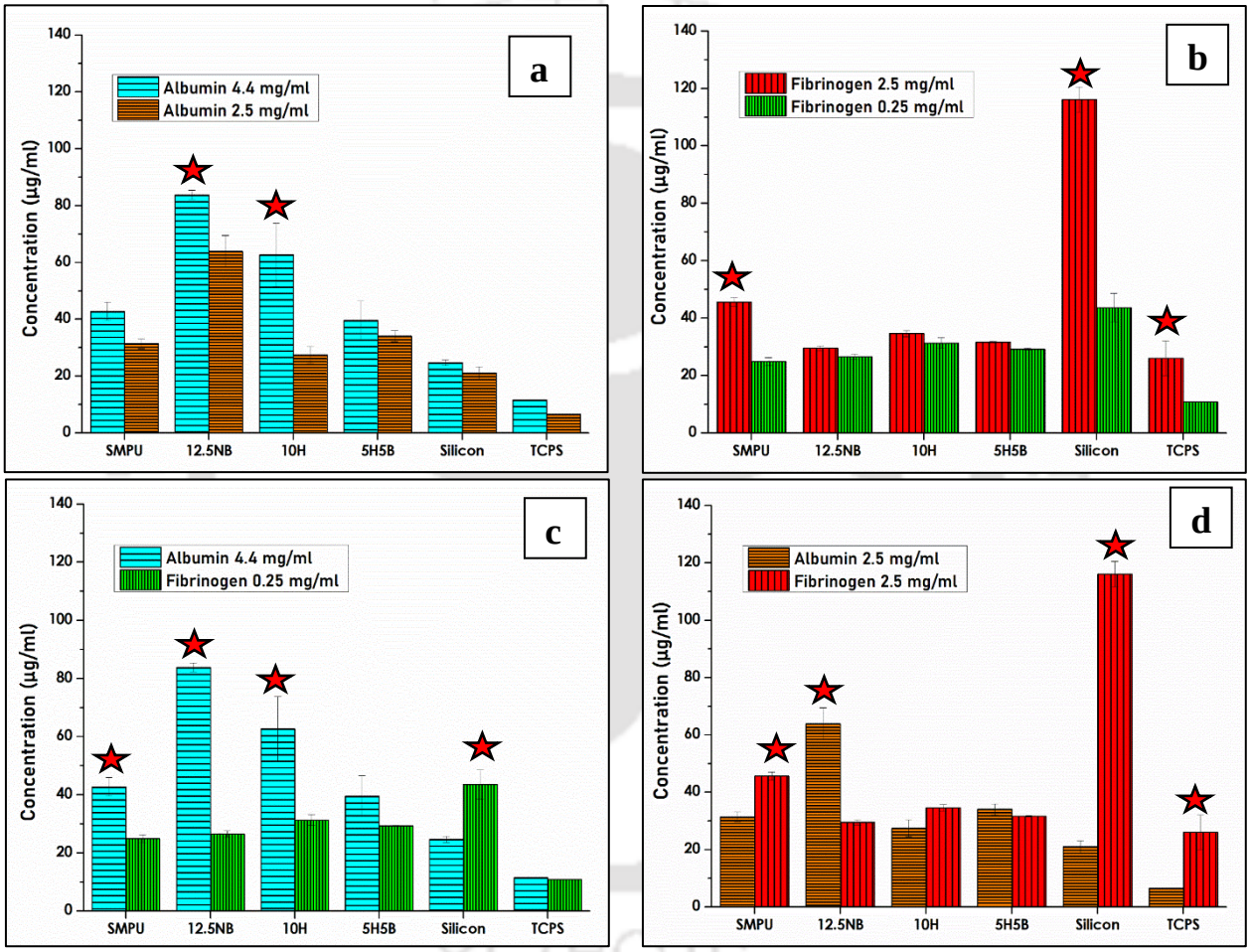

Fig. 5.2. Protein adsorption on the surface of the SMPC: (a) albumin adsorption with respect to protein concentration (4.4 mg/ml, 2.5 mg/ml), (b) fibrinogen adsorption with respect to protein concentration (2.5 mg/ml, 0.25 mg/ml), (c) comparison of albumin and fibrinogen adsorption at approximate 10% of human plasma concentrations (albumin 4.4 mg/ml, 0.25 mg/ml), and (d) comparison of albumin and fibrinogen adsorption at equal concentrations (2.5 mg/ml). Values represent mean ± SD from experiments performed

(★: $p < 0.05$ is a significant change in cell proliferation compared to control)

5H5B are observed to be 31.4 ± 1.7 µg/ml, 63.9 ± 5.6 µg/ml, 27.5 ± 2.9 µg/ml, and 34.1 ± 2.0 µg/ml, respectively and the corresponding values at the level of 4.4 mg/ml are observed to be 42.8 ± 3.2 µg/ml, 83.8 ± 1.6 µg/ml, 62.7 ± 11.1 µg/ml, and 39.6 ± 7.0 µg/ml. A statistically significant difference in adsorption is observed in the 12.5NB and 10H samples at the higher concentration compared to the lower concentration. The control samples, silicon and TCPS, exhibited the lowest adhesion of albumin within the range of 6.6 ± 0.1 µg/ml to 24.7 ± 1.1 µg/ml. The adsorption of fibrinogen at the concentrations of 2.5 mg/ml and 0.25 mg/ml by the tested samples are presented in Fig. 5.2 (b). The fibrinogen adsorption at the concentration of 2.5 mg/ml are 45.6 ± 1.4 µg/ml, 29.5 ± 0.9 µg/ml, 34.6 ± 1.1 µg/ml, and 31.6 ± 0.3 µg/ml for SMPU, 12.5NB, 10H, and 5H5B, respectively and the corresponding values at the concentration of 0.25 mg/ml are reported to be 24.9 ± 1.4 µg/ml, 26.5 ± 1.0 µg/ml, 31.3 ± 1.9 µg/ml, and 29.3 ± 0.3 µg/ml. The silicon sample showed the highest adsorption of the fibrinogen sample for 2.5 mg/ml and 0.25 mg/ml concentrations as 116.1 ± 4.4 µg/ml and 43.6 ± 5.0 µg/ml, respectively, while the corresponding values for TCPS are 26.0 ± 6.0 µg/ml and 10.9 ± 0.06 µg/ml, which are the lowest in this study. The SMPU, silicon, and TCPS exhibited a significant increase in the adsorption of fibrinogen at 2.5 mg/ml in comparison to that of the 0.25 mg/ml concentration. In Fig. 5.2 (c), the albumin is compared with fibrinogen at 10% level of the proteins present in the human plasma approximately. A significant increase in adsorption of albumin is observed in SMPU, 12.5NB, and 10H in comparison to that of fibrinogen, whereas a statically significant decrease is observed in case of silicon sample. The albumin to fibrinogen ratio (A:F) at 10% of the proteins level present in the human plasma for SMP, 12.5NB, 10H, 5H5B, Silicon, and TCPS are calculated to be 1.72:1, 3.16:1, 2:1, 1.35:1, 0.57:1, and 1.07:1, respectively. The adsorption of albumin and fibrinogen by the tested samples, when incubated in individual solutions at equal concentrations of 2.5 mg/ml, is

presented in Fig. 5.2 (d). SMPU, Silicon, and TCPS showed significant adsorption of fibrinogen compared to albumin, while an opposite trend is observed in case of 12.5NB sample.

The enhancement of albumin adhesion against fibrinogen is highly desirable for a successful functionalization of the hemocompatibility of implant materials. A higher albumin: fibrinogen (A:F) ratio indicates a lesser inclination towards blood coagulation and thrombus formation [143–145]. The hemocompatibility of polyurethane is quite well established, and it is being clinically used for manufacturing of implants having blood contact. The variation of the albumin and fibrinogen adsorption ratio is related to the associated surface energies since fibrinogen, being hydrophobic, preferentially adsorbs on hydrophobic surfaces, while albumin (having a hydrophilic nature) adsorbs on hydrophilic surfaces [146,147]. As the affinity of moisture towards SMP MM3520 has already been confirmed, it provides a more suitable surface for albumin adsorption. The higher A:F ratio of the nano barium sulphate and hydroxyapatite composite compared to SMPU predicts a lesser probability of thrombosis in the composites, which enhances its suitability as a blood-contacting medical implant. Thus, the addition of fillers potentially improved the characteristics of the SMPU for its application as an embolic agent. Of all the composites, the 5H5B showed the least A:F ratio, which might lead to a higher tendency for platelet adhesion and coagulation. However, the least amount of protein adsorption is also observed in case of the hybrid composite, which is a factor for decreased coagulation. Though the above study shows promising results for the nano barium sulphate and hydroxyapatite composites, more studies are required to be done to get a better knowledge on the coagulation characteristics of the composites.

5.4 SUMMARY

The SMPU and its composites did not show any cytotoxicity in L132 and HaCat cell line. However, the porous 3D printed Tungsten (7wt%) SMP composite elicited cytotoxic response

in the HaCat cells. Further, the nano $BaSO_4$, nano HaP and hybrid composites showed a lesser affinity for thrombosis or coagulation, making them suitable for blood-contacting implants. In summary, the nano $BaSO_4$, nano HaP and hybrid composites are found to be suitable based on the initial biocompatibility studies for the desired application as embolic agents.

INTENTIONALLY LEFT BLANK

CHAPTER 6: 3D PRINTED POROUS BARIUM SULPHATE SHAPE MEMORY POLYMER COMPOSITE AS AN EMBOLIC AGENT

6.1 INTRODUCTION

In this chapter, SMPC having the desired radiopaque filler and its concentration determined from the previous chapters is fabricated and tested. Based on the biocompatibility studies, nano $BaSO_4$, HaP, and hybrid composites exhibited the desired properties as they have no cytotoxicity and less protein adsorption pertaining to less thrombogenicity. Based on the mechanical, thermomechanical, and radiopaque characteristics, the 10wt% nano barium sulphate SMPC is found to be apt for the proposed application compared to other composites. Hence, the 10 wt% nano Barium sulphate composite has been fabricated by combining extrusion, FFF process and salt leaching process as discussed in chapter 3, and the material properties have been reported. Finally, the feasibility of the delivering the developed SMPC in an aneurysm is tested on a simulator developed to mimic the blood flow through the human circulatory system.

6.2 MATERIALS AND METHODS

6.2.1 Materials

The SMPU, NaCl and nano barium sulphate used in this study are already described in the chapters 3 and 4.

6.2.2 Fabrication of nano barium sulphate SMPC

The filaments for FFF is manufactured by the extrusion process, as discussed in chapter 3. The sodium chloride (NaCl) and nano barium sulphate are mixed in acetone and sonicated in a bath sonicator (Model: Ultra Met 2002 Ultrasonic Cleaner, Make: M/s Buehler, Germany) to

disperse and deagglomerate the nanoparticles. The mixture is also magnetically stirred to disperse the heavier salt particles and is poured on the SMPU pellets and manually mixed to have a uniform coating over the polymer. This mixture is kept in a hot air oven at 60°C for 12 h for the acetone to dry. The SMPU, NaCl, and $nBaSO_4$ are mixed in the ratio of 5:4:1 by weight.

The dried pellets are put in an extruder in order to obtain the salt filled $nBaSO_4$ dispersed SMPC filaments. These filaments are used in a 3D printer to get two rectangular samples having a thickness of 0.5 mm and 1.2 mm for characterization. The complete processing technique and parameters used to obtain the filaments and test samples have been described in detail in chapter 3. The salt is leached out of the samples by the same process as discussed earlier.

6.3 CHARACTERIZATION OF 3D PRINTED SAMPLES

6.3.1 Studies on porosity, density, radiopacity and morphological features of the 3D printed samples

The porosity, density, radipacity and morphological features of the test samples are studied as per the methodology described in Chapter 3.

6.3.2 Thermomechanical study

The thermomechanical test is conducted on a dynamic mechanical analyzer (Model: MCR 702 multidrive, Make: M/s AntonPaar GmbH, Graz, Austria). Solid rectangular specimen of approximately 3 mm x 2 mm x 0.5 mm is cut from the 3D printed samples using a sharp knife. The specimens are tested in tensile mode and run from -10°C to 60°C and heated at a rate of 3°C/min. The temperature sweep was conducted at a frequency of 1 Hz with a peak to peak

amplitude of 0.5%. A compression-molded SMPU sample is also tested for reference. The samples are dried in a hot air oven at 110°C for 4 hours to remove moisture.

6.4 DEVELOPMENT OF AN ANEURYSM SIMULATOR MIMICKING THE BLOOD PRESSURE AND FLOW IN THE ARTERY

Shape memory polymers have not yet been tested as embolic agents for endovascular embolization in humans, and thus, the practicality of delivering the embolic agent on the desired site is required to be studied. Further, a simulator will help the clinicians to get more comfortable with delivering the implants and get accustomed to the unforeseen issues with delivery of embolic agents. This simulator can also be used to study the dynamics of fluid flow in the aneurysm after implantation. Thus, an aneurysm model with pulsatile flow mimicking the human circulatory system has been developed to test the feasibility of delivering the SMPC into the aneurysm.

The conceptual model is based on the principle of arterial expansion and contraction during the systemic circulation of the blood, and it is shown in Fig 6.1. The blood is pumped out from the heart at a pressure that maintains the circulation of the blood. The two main phases of blood circulation in the body are the systolic and diastolic phases. During the systolic phase, the blood is pumped out from the ventricle to the aorta. Due to the aorta's elasticity, the incoming blood will produce stresses on the aortic wall leading to its expansion [148,149]. This helps the aorta in storing the blood during the systolic phase. During the diastolic phase, the aortic valve is closed, and the ventricle is in its filing period. The aorta is a low compliant system that brings the aorta back to its original dimension and releasing the stored blood. Thus, even during the ventricle filling phase, the blood will be continuously circulated to the rest of the organs resulting in the systemic circulation. The expansion and contraction of the aorta are directly related to the pressure with which the ventricle pumps the blood. The same pattern of storing

and releasing the blood is done by the larger arteries. The aortic valve is responsible for the generation of pulsatile flow in the arteries. These pulsations continuously create the arterial movement for the proper systemic circulation. In the vascular system, the left ventricle contraction time for pumping out the blood into the aorta is 0.27s, and the ventricle relaxation time when the aortic valve remains closed to fill the left ventricle is 0.53s. Thus, the total opening and closing time of the aortic valve is 0.8s, which generates one heartbeat, and the average number of heartbeats per minute is 72-75 [150].

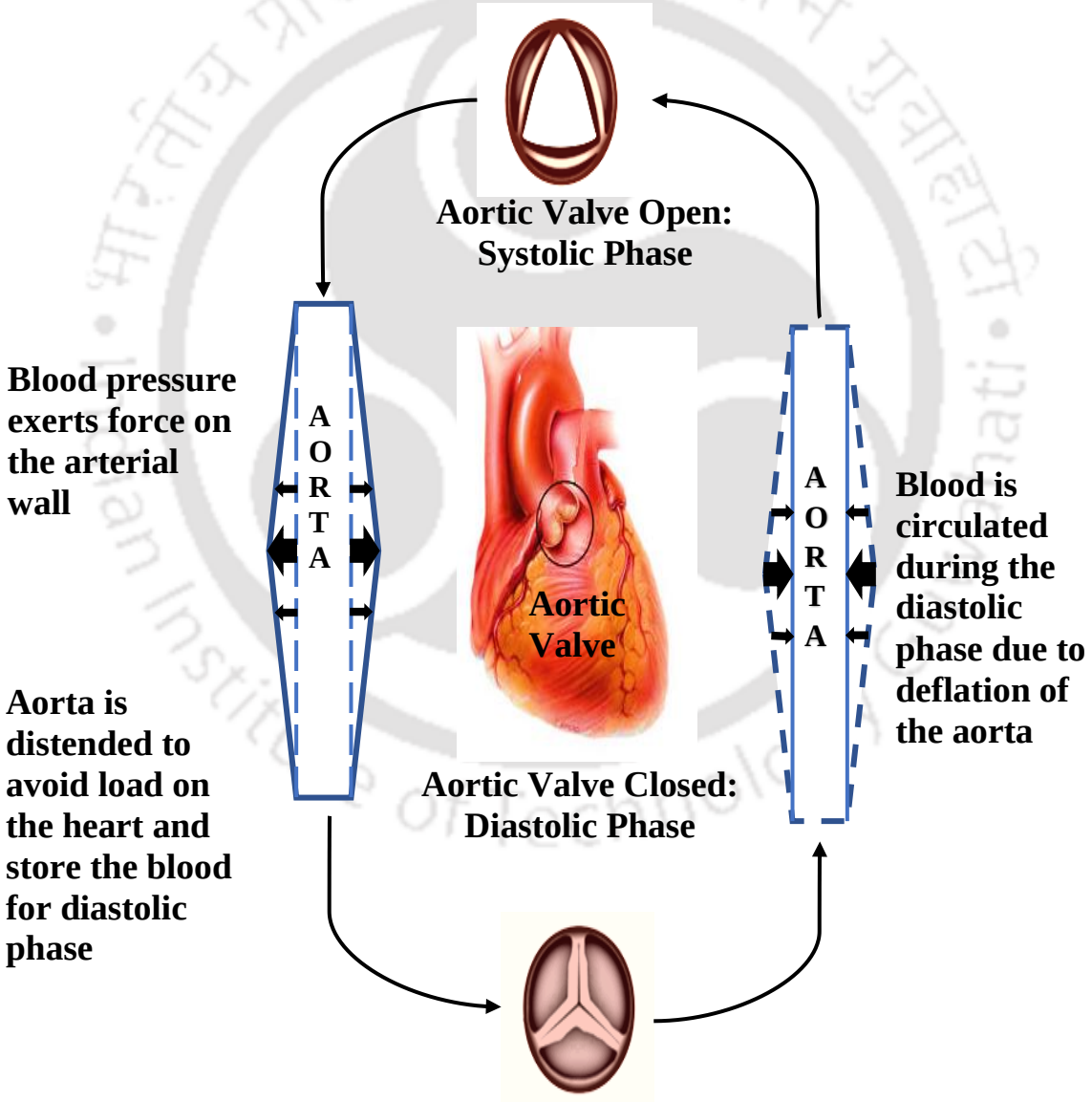

Fig 6.1. Schematic diagram of the working principle of the proposed simulator

In this simulator, distilled water is chosen as an alternative to blood. Due to the complex chemistry of blood and the possibility of coagulation, the use of blood is avoided during the present study. The aneurysm model chosen for this specific study is a saccular shaped aneurysm and the arterial section is chosen to mimic the femoral artery, which is the most commonly used insertion point of the catheter in endovascular embolization.

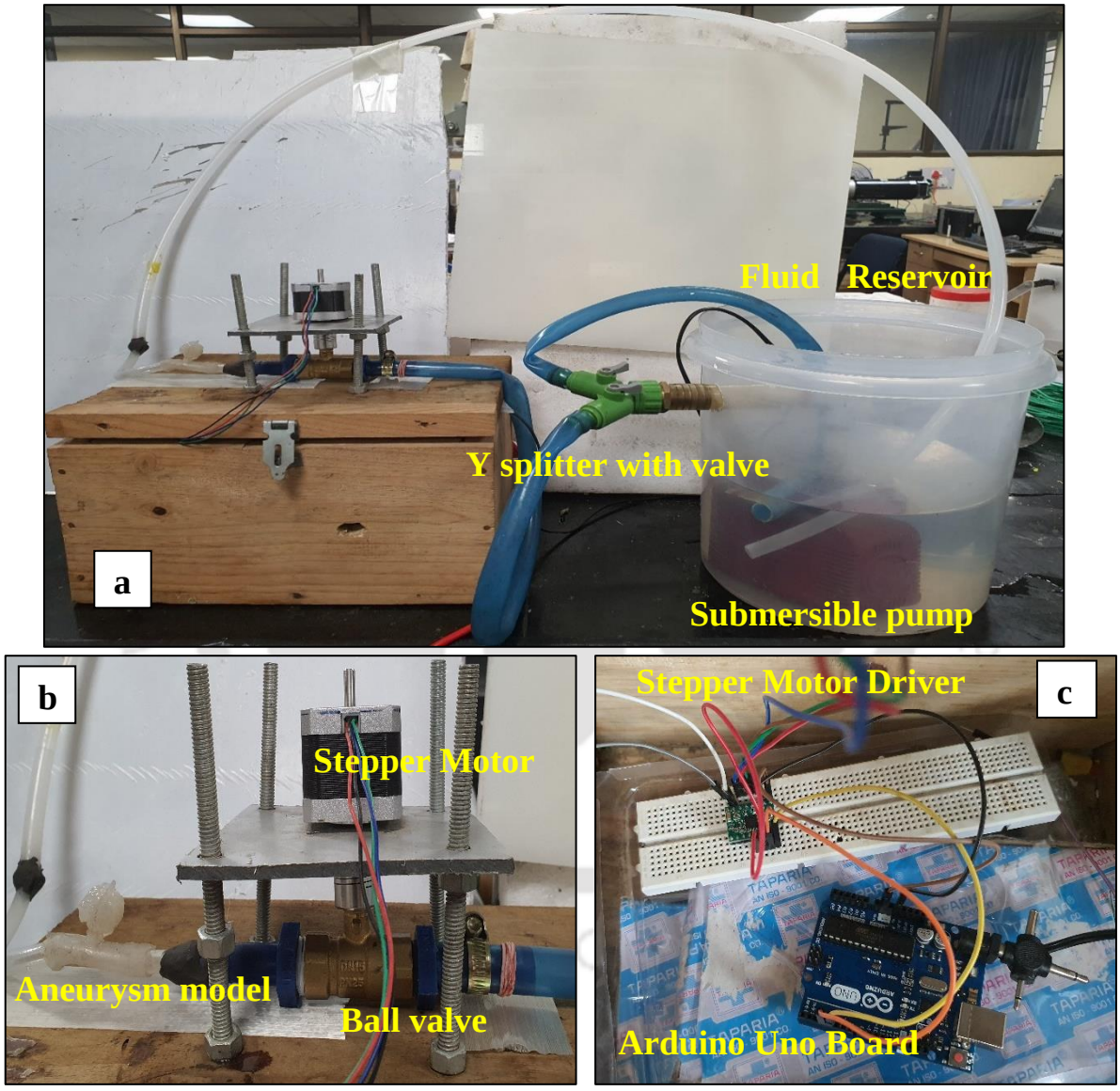

Fig. 6.2. Photographic view of the (a) aneurysm simulator setup; (b) stepper motor, ball valve, and aneurysm model; (c) electronic circuit for control

The photographic view of the aneurysm model setup having the pulsatile flow is shown in Fig. 6.2 (a). The pulsatile flow in the developed simulator is generated by using a mechanical

valve that is programmed to open and close at a regular interval. This mechanism is actuated by a programmable stepper motor, which can precisely rotate the valve for a specific period of time. The setup consists of a fluid (water) reservoir, pump, Y-splitter with valves, brass ball valve, stepper motor, an aneurysm model, and a microcontroller board, as shown in Fig. 6.2 (b,c).

Different pumps such as centrifugal pump, reciprocating pump and peristaltic pump are considered on the basis of flow rate, pressure head, and cost for this study. However, some of the issues with the pumps are very high flow rate (100L/min) or very low flow rate (2L/min), high pressure head and cost, which made them inappropriate for the present work. Based on the inherent advantages and the requirements, a submersible pump (Amicikart AK-SMPP-TY-40 Pump) with a flow rate of 53 litres/minute and pressure head of 200 mmHg is selected considering that the maximum cardiac output of a human heart can go up to 40 litres per minute and the blood pressure to 160 mmHg [151].

The Y splitter valve is used to control the pressure and flow rate following the working parameters of the human heart. The flow rate and pressure in the system are controlled by positioning the two valves of the splitter and attaching pipes with different diameters ranging from 5 to 25 mm. The smaller diameter pipes help to retain the fluid inside the arterial model, thus maintaining the diastolic pressure inside the artery. The pressure at the output of the aneurysm model is measured using a bourdon type pressure gauge (M/s Excel instruments, New Delhi, India), and the valves of the Y-splitter are adjusted in order to get the required pressure and flow rate. The dimension of the Y splitter is 20 mm inlet and 16 mm outlet each. One side of the Y splitter carries the liquid to the valve, and the other side transfers the remaining liquid back into the reservoir.

The pulsatile flow of the circulatory system is generated by the motor-operated ball valve and the stepper motor, as shown in Fig. 6.2 (b). A regular brass ball valve with a diameter of

1/2 inch is used in the simulator, which is connected to the stepper motor. During the selection of the motor for this simulator, other commercially available motors such as DC motors, servo motor, stepper motors are considered. However, precise position control and good holding torque of the stepper motor made it as an ideal candidate for generating the pulsatile flow. The stepper motor used for the aneurysm simulator is NEMA 17 (National Electrical Manufacturers Association), where 17 indicates the motor's face size of 1.7 * 1.7 inches. NEMA 17 stepper motor is a bipolar stepper motor with two phases and gives 200 steps in each revolution with a step angle of 1.8°. The holding torque of the motor is 2 kg*cm. Unlike servo motors, this motor operates in an open circuit that requires a feedback mechanism to move in a particular direction. As it is a bipolar motor, it requires a stepper motor driver having two H-Bridge circuits.

The stepper motor driver used for this model is A4988, which limits the requirement of current at each phase in order to have smooth functioning of the motor, and it is controlled using microcontroller Arduino Uno. The Arduino Uno microcontroller board, stepper motor driver, and other electrical components used for control are shown in Fig. 6.2 (c). The control signal from the microcontroller interacts with the stepper motor driver, which in turn runs the stepper motor. The Arduino Uno is a microcontroller board based on the ATmega328. It has 14 digital input/output pins (of which 6 can be used as pulse width modulation outputs), 6 analog inputs, a 16 MHz crystal oscillator, a USB connection, a power jack, an ICSP header, and a reset button. The ATmega328 has 32 KB of flash memory for storing code, 2 KB of SRAM, and 1 KB of EEPROM. Each of the 14 digital pins on the Uno can be used as an input or output. The Uno has 6 analog inputs, each of which provides 10 bits of resolution.

The valve is attached to the stepper motor with the help of a coupler and it is shown in Fig. 6.2 (b). The stepper motor is mounted on a wooden box using bolts to support the motor and valve fixation. The digital signal from the Arduino Uno directs the stepper motor driver to control the speed and direction of the motor. The motor speed is programmed in such a way

that it gives 60 rotations (beats) anticlockwise direction. The clockwise and anticlockwise movement results in the ball valve opening and closing mechanism, respectively. This precise programming for the direction control of clockwise and anticlockwise rotation of the ball valve gives the opening time of ball valve of 0.3s and the closing time of 0.5s. This part represents the aortic valve of the anatomical circulation system. The aneurysm model is attached to the valve and it is shown in Fig. 6.2 (b).

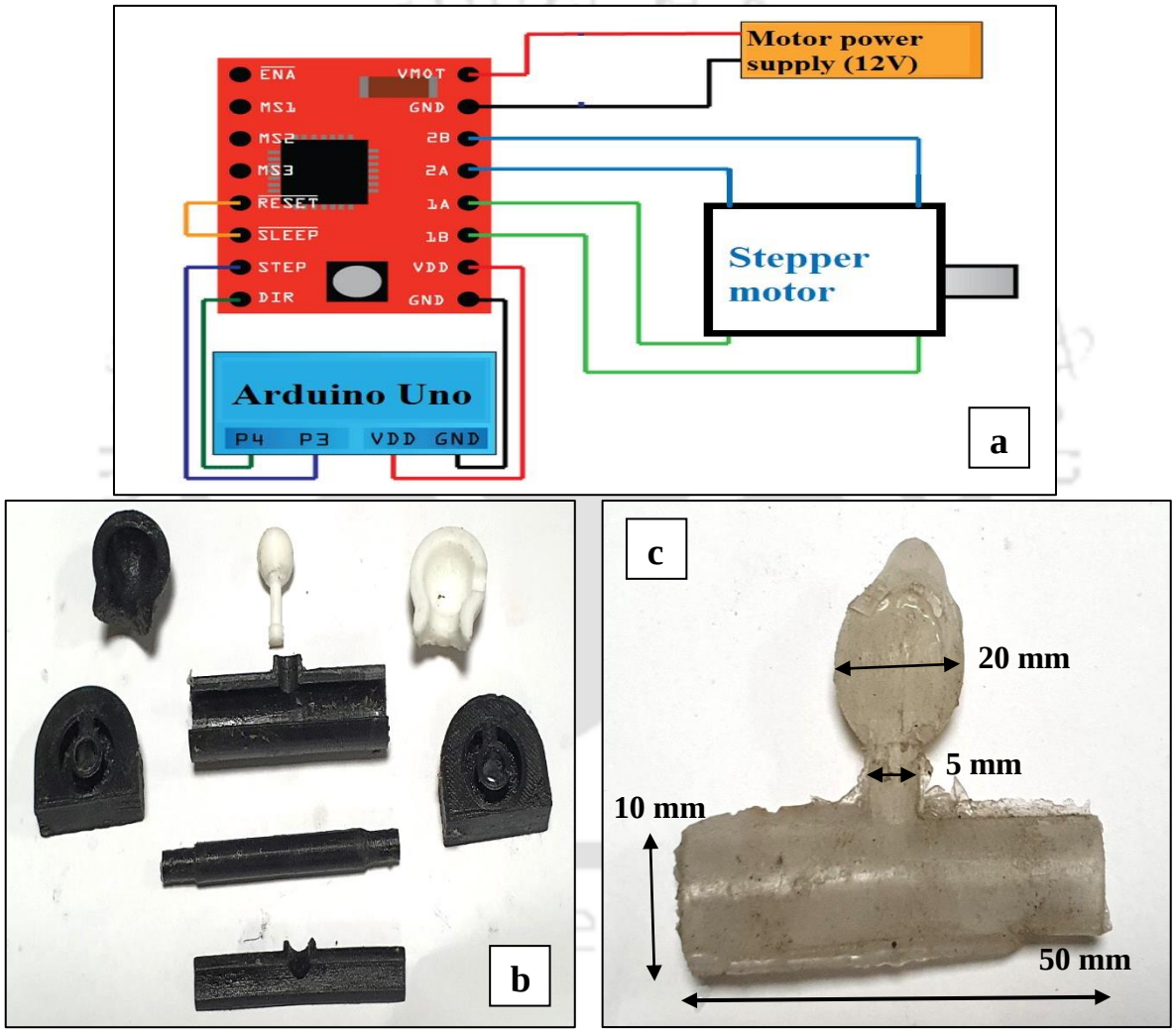

Fig. 6.3. (a) schematic view of the stepper motor control circuit; (b) 3D printed mould used for making the aneurysm; (c) Aneurysm model made from silicone

The schematic diagram of the stepper motor driver, Arduino Uno, and its connection to the stepper motor is shown in Fig. 6.3 (a). The aneurysm model is made from a 3D printed mold,

and it is shown in Fig. 6.3 (b). The outer diameter of the artery portion is 10 mm, and the thickness is 1 mm. The inner diameter of the neck portion of the aneurysm is 3 mm, and the outer diameter of the aneurysm is 20 mm with a wall thickness of 1 mm. Murtisil Silicone Rubber RTV (M/s Aditya Genuine products, New Delhi, India) is poured into the mold and kept overnight to have complete curing, and the final product obtained is shown in Fig. 6.3 (c).

6.4.1 Shape memory test in the Aneurysm simulator

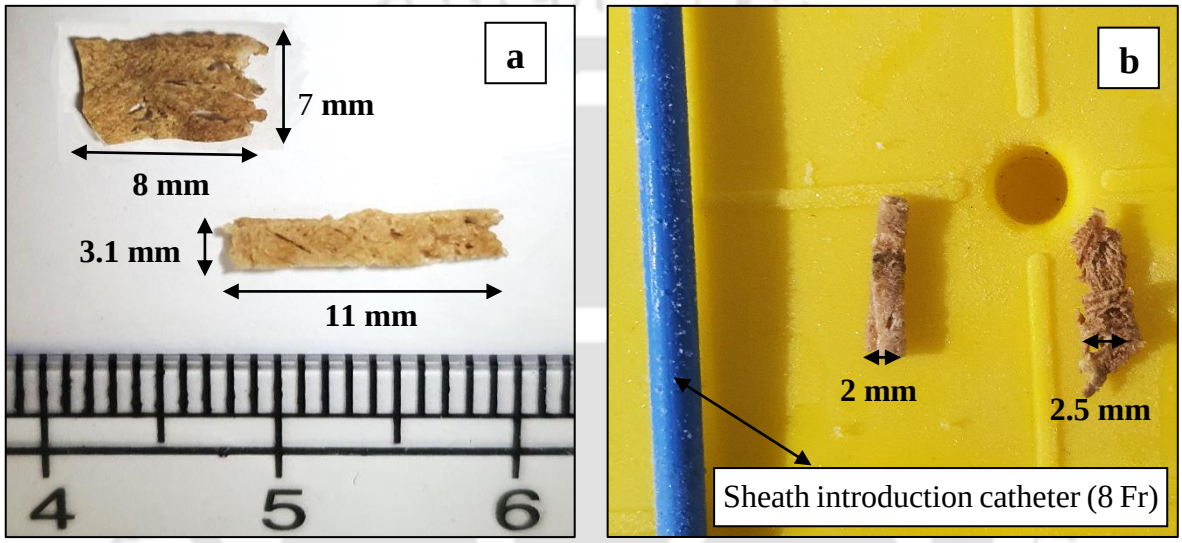

Fig. 6.4. (a) Initial shape of the porous nano $BaSO_4$ SMPCs; (b) programmed shape of the samples

The sheath introduction catheters (AVANTI®+ Sheath Introducer, Cordis, California, USA) of size 7 & 8 Fr are used for pushing the temporary shape of porous barium sulphate SMPC samples into the aneurysm. As shown in Fig. 6.4 (a), samples of different shapes are used to fill the aneurysm. The top sample of Fig. 6.4 (a) is 3D printed, and the bottom sample is cut from a 3D printed samples after leaching of the sample is completed.

The samples are heated to 70°C in a hot air oven and rolled to get the secondary shape (smaller footprint) as shown in Fig. 6.4 (b) and cooled to -10°C in a household refrigerator. The rolled SMPC (programmed shape) is loaded into the sheath introduction catheter manually, as seen in Fig. 6.5 (a, b). An incision is made on the artery section of the aneurysm, and the

catheter is pushed into the neck of the aneurysm, as shown in Fig. 6.5 (c). The samples are delivered into the aneurysm, and the final shape of the expanded sample is observed by cutting the aneurysm.

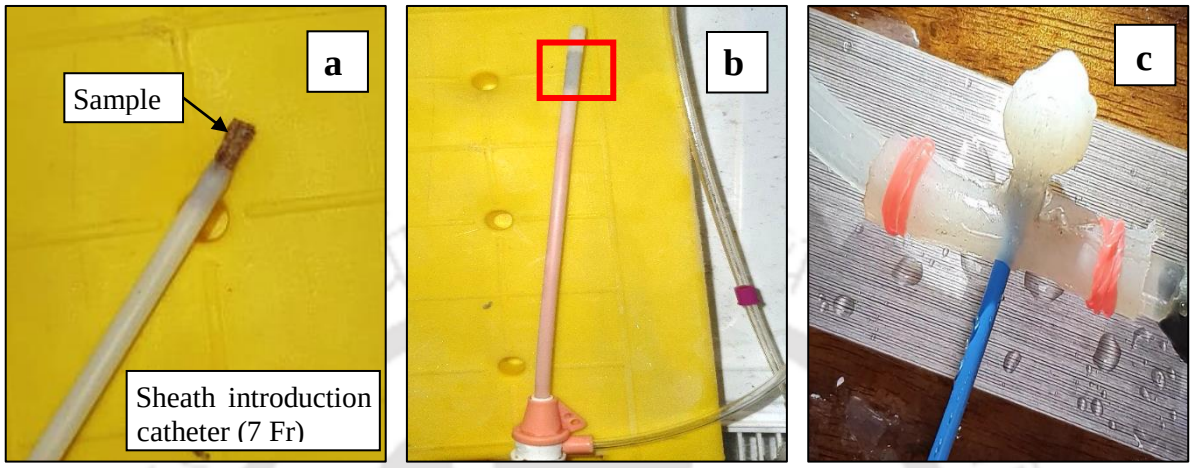

Fig. 6.5. (a) sample in programmed shape being inserted into the catheter; (b) programmed sample fully inserted in the catheter; (c) the catheter inserted into the aneurysm

6.5 RESULTS AND DISCUSSION

6.5.1 Morphological Studies

The FESEM image of the cross-sectional view of the nano $BaSO_4$ SMPC after salt leaching is shown in Fig. 6.6. It is observed that no salt particles are present in the sample after leaching. As expected from the earlier studies, the pores in the porous nano $BaSO_4$ SMPC are unevenly spaced, inhomogeneous, and have different sizes and shapes. The pore sizes are observed to be varied from a few µm to about 200 µm. Further, a large number of small pores are also observed within the larger and deeper pores confirming their interconnected porous network. A wide range of pore size can be attributed to the non-homogeneous size of the salt particles used for pore generation, agglomeration of the salt particles, and their random distribution during the fabrication process. The salt particles are expected to be completely leached out due to the interconnected network of pores.

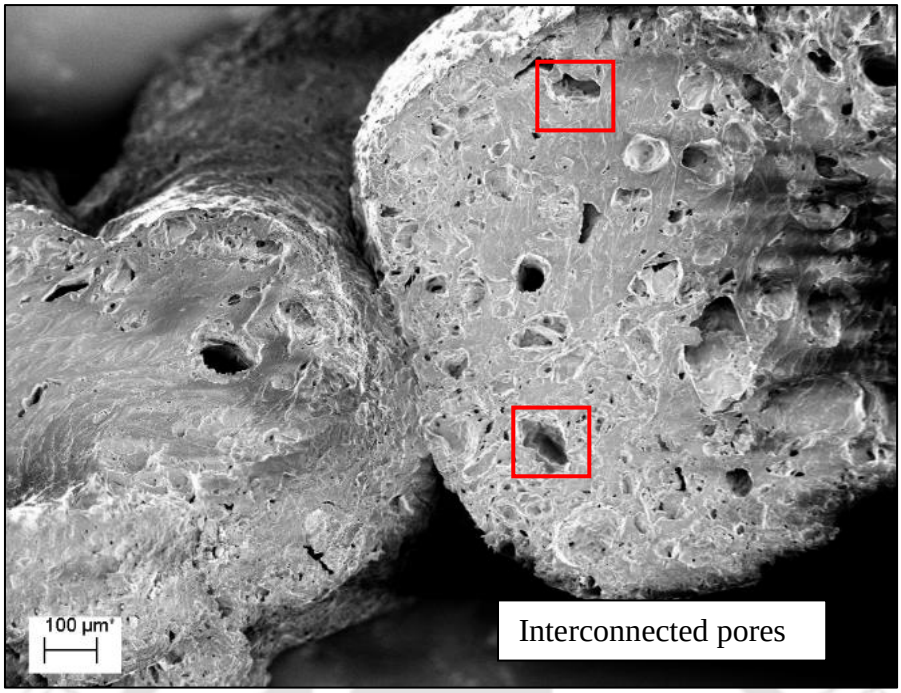

Fig. 6.6. Surface morphology of cross-sectional view of porous nano $BaSO_4$ SMPC

6.5.2 Porosity and density studies

Table 6.1. Density of the samples and their porosity

S No.	Sample	Density of the sample after leaching (g/cm^3)	Theoretical density of fully leached sample using Eq 3.1 (g/cm^3)	Theoretical porosity (%) considering full leaching	Porosity (%) based on weight loss of the sample
1	Porous $BaSO_4$ SMPC	0.86 ± 0.014	0.89	30.5	29.5 ± 0.4
2	Porous SMPU	0.72 ± 0.013	0.79	36.5	36.05±0.15
3	3D printed SMPU	1.20 ± 0.008	NA	NA	NA

The density and porosity of the nano $BaSO_4$ SMPC obtained after the leaching process is reported in Table 6.1. It is compared with the 3D printed SMPU, and porous SMPU obtained from chapter 3. The density of the porous nano $BaSO_4$ is observed to be 0.86 ± 0.014 $g/cm^{3,}$ and the porosity based on the weight loss obtained from leaching is calculated to be 29.5%. Also, the experimental results on the porosity of the said composites are observed to be very close to that of the theoretical porosity of 30.5%.

The decrease in porosity of the nano $BaSO_4$ SMPC in comparison to that of porous SMPU is due to the less concentration (40wt%) of NaCl in comparison to 50 wt% NaCl in the porous SMPU. As NaCl is responsible for the pore formation, a lesser quantity of NaCl decreased the porosity. It is noted that the NaCl is completely leached out from the samples, and it is further confirmed from the FESEM images shown in Fig. 6.6. Since $BaSO_4$ is insoluble in water, it is not expected to leach out from the samples. The variation between the theoretical and experimental results of the density and porosity can be attributed to the FFF process, inhomogeneous salt distribution, and a very few unleached salt particles, which are trapped in the closed pores.

6.5.3 Thermomechanical Studies

Fig. 6.7 (a) shows the storage modulus of the molded SMPU and porous $BaSO_4$ SMPC in the range of -10°C to 60°C. The moulded SMPU is chosen for comparison as it does not contain any random pores or defects during the processing as evident with 3D printed samples, which can affect the test results. It is observed from Fig. 6.7 (a) that the storage modulus of test samples started to decrease slowly, which is followed by a drastic decrease in the storage modulus by two orders of magnitude, and then converged into a plateau in the order of a few MPa. The storage modulus of the samples in the glassy state at -1°C and the glass transition temperature of the test samples are reported in Table 6.2. The storage modulus of the porous nano $BaSO_4$ SMPC is observed to be decreased by 59% in comparison to that of the molded SMPU. The storage modulus of the porous nano $BaSO_4$ SMPC in rubbery state is observed to be 2.48 MPa. Fig. 6.7 (b) shows the damping factor (tan δ) of molded SMPU and porous $BaSO_4$ SMPC in the temperature range of -10°C to 60°C. The temperature corresponding to the peak value of tan δ is specified as the glass transition temperature of the sample, and the results are reported in Table 6.2. The glass transition temperature of molded SMPU and porous $BaSO_4$ SMPC are observed to be 32°C and 29.35°C, respectively.

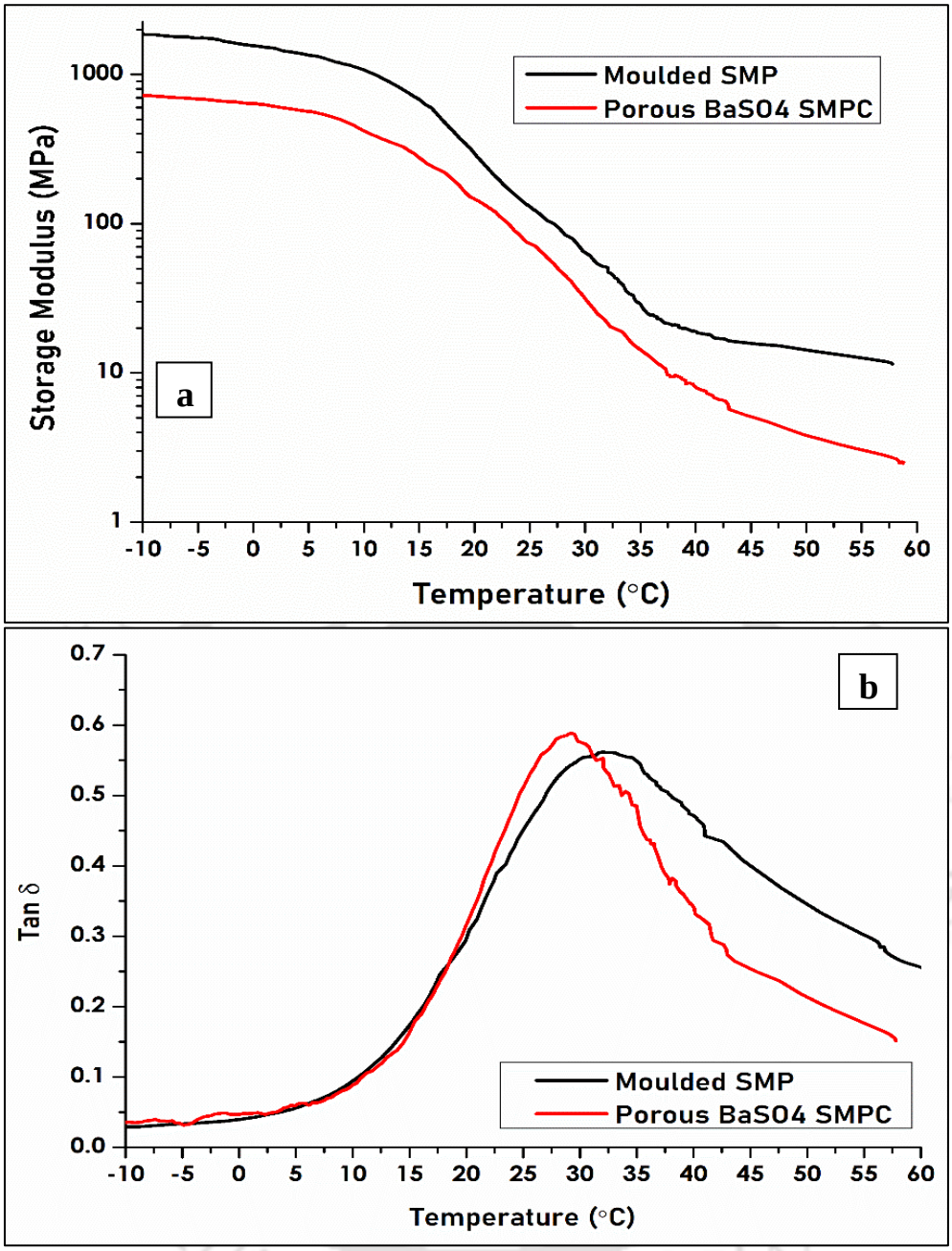

Fig. 6.7. (a) Storage modulus and (b) tan δ curves of molded SMPU and porous $BaSO_4$ SMPC

Table 6.2. Storage modulus at -1°C and glass transition temperature of the samples

Sample	Density (gm/cm^3)	Storage modulus (MPa)	Glass transition (°C)
Molded SMPU	1.25	1590	32.05
Porous $BaSO_4$ SMPU	0.86 ± 0.014	647	29.35

The decrease in the storage modulus of the SMPC is expected due to its porous structure in comparison to that of the solid molded sample. The porous nano $BaSO_4$ SMPC had a higher storage modulus than the porous SMPU due to a lower pore volume of 30.5% compared to 36.5%. No significant difference between the glass transition temperature of both porous SMPC and solid SMPU is observed. As expected from the earlier experiments, the glass transition temperature of the test material is not influenced by the processing techniques such as extrusion, compression molding, FFF processing, and salt leaching as there was no change in the polymer structure during these processes. Also, the glass transition temperature is not affected by the porosity and density of the samples. The storage modulus of the test sample in rubbery state is very close to the elastic modulus of the wall of the abdominal aortic aneurysm, i.e., 1.5 - 4 MPa, which makes it well-suited to be used as an embolic agent [152].

6.5.4 Radiopacity Test

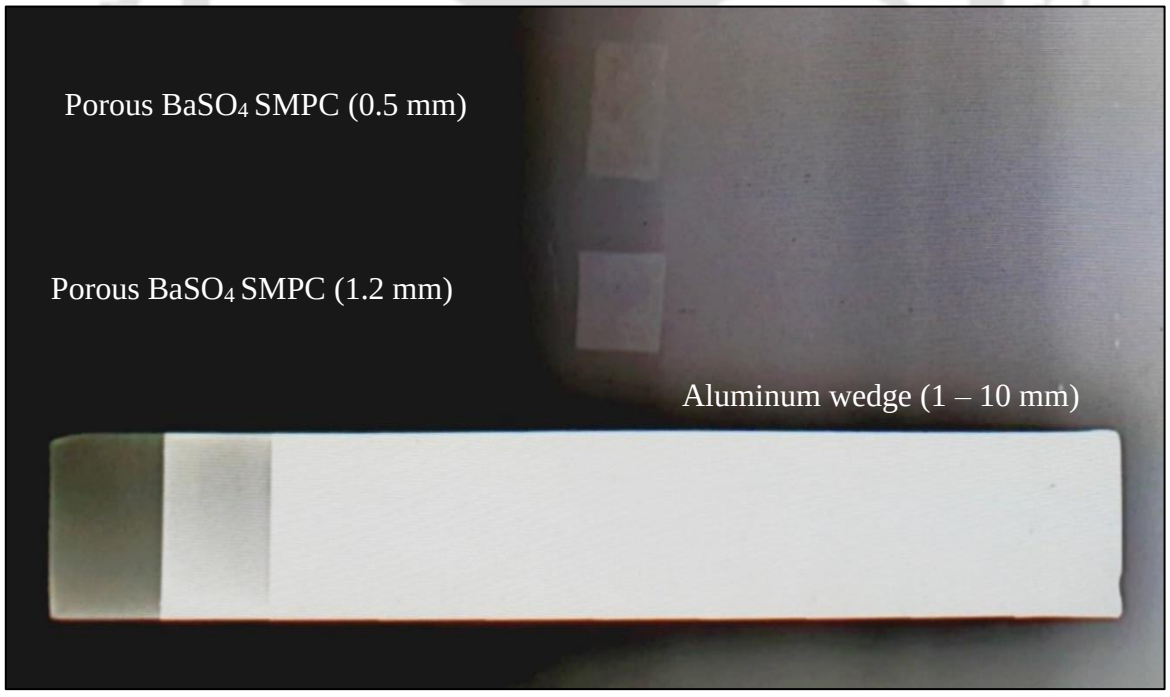

Fig. 6.8. X-ray image of the porous $BaSO_4$ SMPC with an Aluminium wedge (1-10mm) as standard

The radiograph of the 3D printed porous $BaSO_4$ SMPC along with the Aluminium wedge is presented in Fig. 6.8, and the quantitative values of intensity of test samples after subtracting its background are reported in Table 6.3. The intensity of the test samples is compared with Porous SMPU and compression-molded 10 wt% nano Barium Sulphate SMPC, where the results are obtained from the previous chapters while taking 1mm Aluminium as the standard. It is observed that the reported intensity is increased with increasing thickness of the sample. The intensity of porous barium sulphate SMPC is observed to be higher than the porous SMPU even though it is thinner by 33%. The compression-molded sample for the same concentration and thickness showed a better radiopacity than the porous sample.

Table 6.3. Pixel intensity of the 3D printed porous nano $BaSO_4$ samples

Sample along with its thickness	Pixel Intensity	Intensity % relative to 1 mm Al
1mm Aluminum	40.134 ± 5.826	100
Porous $BaSO_4$ SMPC (1.2 mm)	28.050 ± 4.036	69.89
Porous $BaSO_4$ SMPC (0.5 mm)	14.168 ± 4.404	35.30
Porous SMPU (0.75mm)	-	31.64
Compression moulded 10 wt% nano $BaSO_4$ SMPC (0.5 mm)	-	47.6

Radiopacity is a function of material thickness, physical density, electron density, elemental composition, and X-ray photon energy [153]. The compression molded solid sample can absorb more X-rays than the porous structure of the 3D printed sample. The addition of 10 wt% $BaSO_4$ increased the radiopacity of the SMPU, which makes it better suited for its application in interventional radiology techniques.

6.5.5 Feasibility studies on shape recovery of shape memory polymer composites in an aneurysm simulator

The aneurysm simulator pumped about 60 ml of fluid at every beat i.e. opening of the valve, which added up to about 3.6 l/min at a pressure of 1.5 psi (77.5 mmHg) to 2.5 psi (129 mmHg). The pressure is measured using a pressure gauge at the end of the aneurysm model. The weaker portion of the aneurysm model ballooned up during the systolic phase and deflated during the diastolic phase, and both are shown in Fig. 6.9 (a,b). The inflation and the deflation of the aneurysm model followed the cycle of opening and closing of the valve.

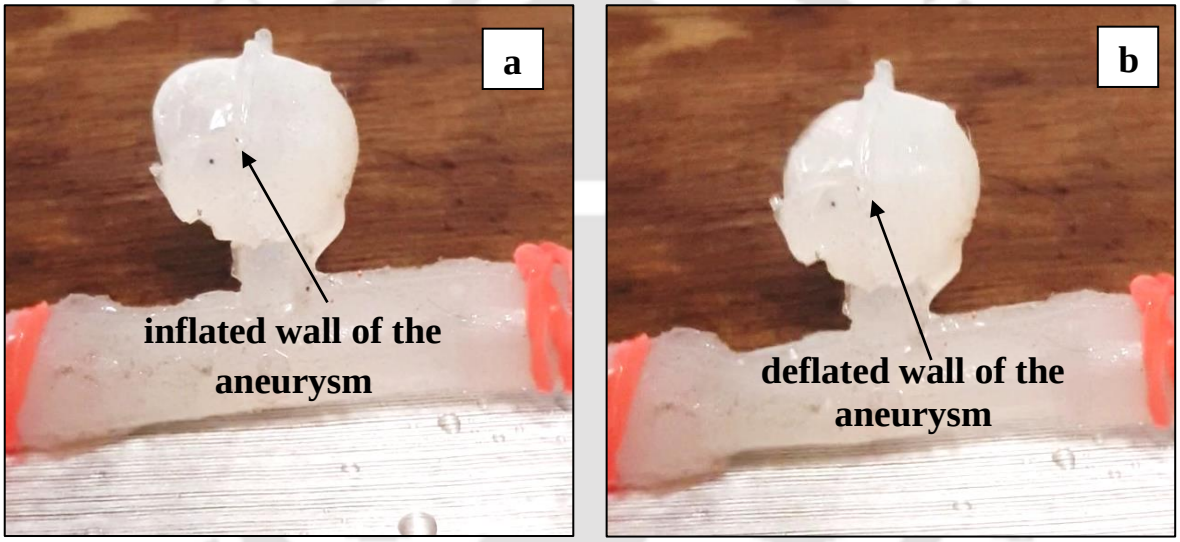

Fig 6.9. Aneurysm model in the simulator: (a) systolic phase, (b) diastolic phase

The shape recovery of the samples from the temporary/programmed shape to the final recovered shape is shown in Fig. 6.10. The recovered samples inside the aneurysm model are shown in Fig 6.10 (a) and can be seen as dark shadows on the wall of the aneurysm model. The cross-section of the aneurysm model is shown in Fig 6.10 (b). The samples recovered to their original shape inside the aneurysm and they partially filled the space in the aneurysm. Finally, the samples are taken out from the aneurysm to see their final recovered shape, which are shown in Fig 6.10 (c, d). It is observed that the samples have not recovered fully to their original permanent shape, as seen in Fig 6.4 (a). The samples have a bit of curvature compared to the

flat contour of the permanent shape. However, this shape might have been attained due to the shape of the aneurysm.

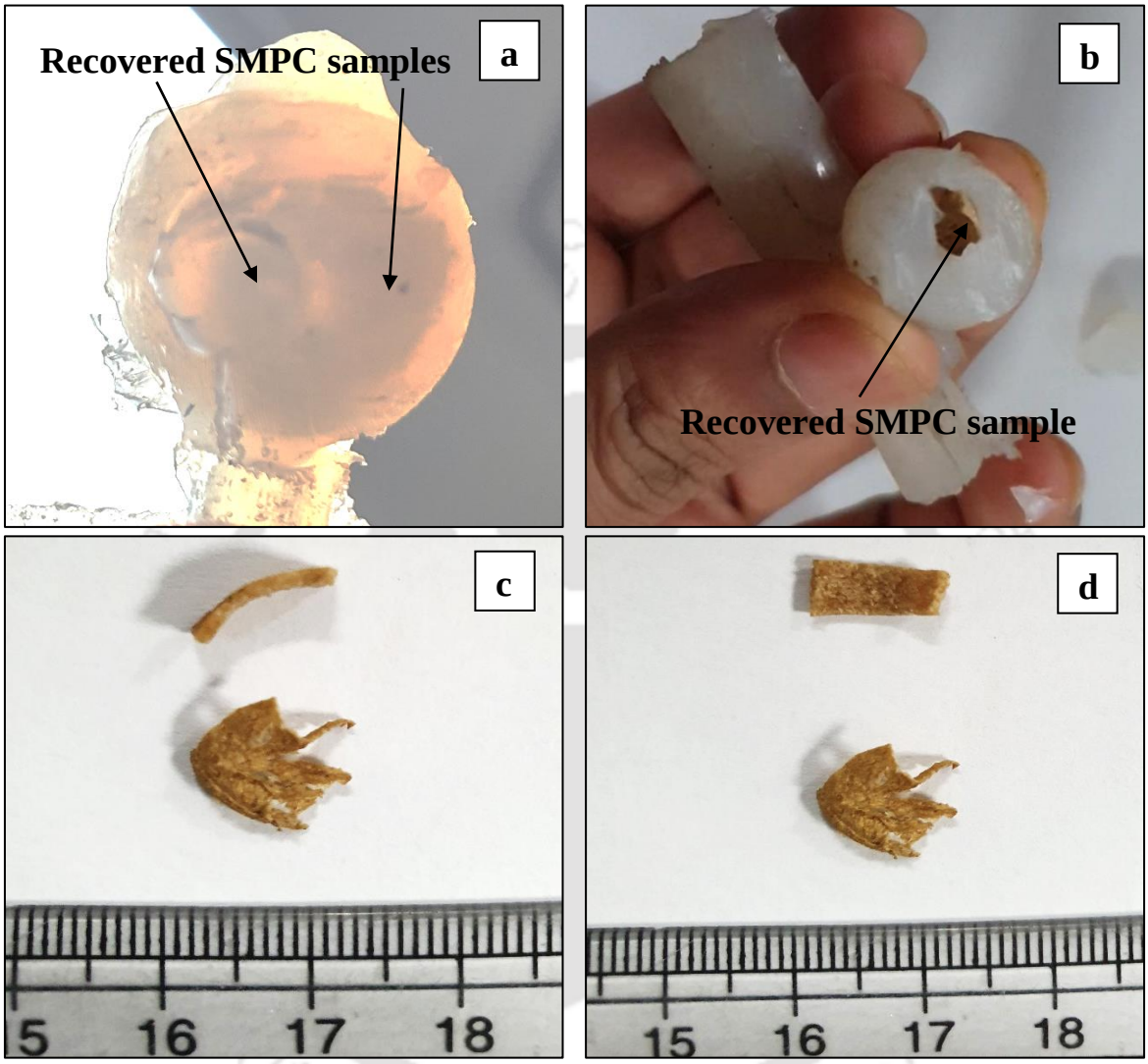

Fig 6.10. Shape recovery: (a) the recovered sample inside the aneurysm model; (b) cut cross-section of the aneurysm model; (c) final recovery shape of the samples (front view); (d) final recovered shape (top view)

The simulator successfully mimicked the *in vivo* conditions of an aneurysm, and the inflation and the deflation of the weaker section of the aneurysm wall is observed. The SMP based composites are successfully delivered into the aneurysm model with the help of a catheter, and they recovered inside the aneurysm by filling its volume. Hence, the feasibility

of the SMPC as an embolic agent for interventional radiology techniques has been successfully established in the aneurysm simulator.

6.6 SUMMARY

In summary, radiopaque porous 3D printed nano barium sulphate filled SMPC is fabricated by the novel processing technique combining extrusion, FFF and salt leaching process. Though the addition of 10wt% nano barium sulphate in the SMPU did not significantly affect its thermomechanical properties, its radiopacity is increased. Thus, the SMPC can be explored as an alternate embolic agent. The feasibility of using SMPC in interventional radiology technique has been proven in an in-house developed aneurysm simulator.

CHAPTER 7: SUMMARY AND CONCLUSIONS

In this work, a shape memory polymer (SMP) based embolizing agent has been developed for minimally invasive surgery that overcomes the limitations of the clinically used agents. A novel fabrication technique has been proposed by combining extrusion, fused filament fabrication (FFF), and salt leaching process to produce the porous composites. Subsequently, the radiopaque shape memory polymer composites with tungsten/ barium sulphate as a radiopaque filler material have been developed to complement the above-mentioned process. Initially, SMPC with tungsten (7wt%) as a radiopaque filler mixed with NaCl (43%) as a pore forming agent has been developed to complement the above-mentioned process process. Both tungsten and NaCl are dispersed in acetone and mixed with SMP MM 3520 to obtain the coated polymer, which is extruded to produce a filament to be used in FFF printing. After printing the desired shapes using FFF, the salt particles are leached out to produce the porous structure. During the shelf aging period, the tungsten used in the porous SMPC is oxidized, and cytotoxic behaviour of the said composite is observed during the biocompatibility studies. Thus, different possible materials namely, nano $BaSO_4$ and nano HaP and their combinations are explored for the proposed application instead of tungsten as a radiopaque material.

In this direction, hybrid radiopaque SMPU composites have been developed by adding barium sulphate for radiopacity and hydroxyapatite for embolization. Nano barium sulphate (4wt%, 10wt%, and 12.5wt%) SMPU composites, nanohydroxyapatite (2.5wt%, 5wt%, 7.5wt%, and 10wt%) SMPU composites, and hybrid composites (2.5wt%HaP/7.5wt%BaSO4, 5wt%HaP/5wt%BaSO4, 2.5wt%HaP/ 7.5wt%BaSO4) are fabricated by extrusion and compression molding process. Extrusion is done to ensure proper mixing between the different fillers and SMPU, and the extruded filaments are pelletized. These pellets are used to fabricate composite plates by compression molding technique for material characterization. Based on

the different characterization techniques followed and the initial biocompatibility studies, the barium sulphate (10wt%) is found to be a suitable radiopaque material to prepare 3D printed composites to overcome the deficiencies of other materials including that of tungsten. The viability of the deployment of SMPC in an aneurysm is successfully tested in an in-house developed simulator, which replicates the surgical procedure performed for the treatment of aneurysms. The important findings of the present work are reported below:

7.1 NOVEL PROCESSING TECHNIQUE: EXTRUSION + FFF (FUSED FILAMENT FABRICATION) + SALT LEACHING

1) Extrusion, FFF, and salt leaching processes are combined to fabricate the porous test samples having <200 μm pore size.
2) The volume of porosity in the test sample is directly proportional to the concentration of salt particles.
3) The size and shape of the pores on the samples are dependent on the size of the salt particles.
4) Salt particles are found to aggregate to produce larger pore sizes and interconnected porous network within the large pores present in the test samples.
5) Salt particles are leached out completely, or very minimal salt particles are trapped within the closed pores.

7.2 POROUS TUNGSTEN SMPC AS AN EMBOLIZATION AGENT

1) A porous tungsten (7wt%) SMPC is developed to be used as an embolic agent complementing the novel processing technique.
2) The porous tungsten SMPC is observed to have the same porosity level in comparison to that of theoretically estimated values.

3) During the leaching process, the radiopaque filler, tungsten, is not removed from the sample.

4) The pores observed in the tungsten SMPC are randomly distributed, and the composites have a wide range of shape and size of pores ranging from few microns to 250 µm.

5) The processing technique and the addition of tungsten are not found to affect the polymer structure of SMPU.

6) The shape fixity of the tungsten SMPC is not affected by the presence of the pores and processing technique.

7) The shape recovery of the porous tungsten composite was about 95% during the first recovery cycle, and it is increased to 100% during the 2nd shape recovery cycle.

8) The visibility of the porous 7wt% tungsten SMPC under X-ray fluoroscopy is at par with 1mm thick Aluminum plate.

7.3 SMPU COMPOSITES ($nBaSO_4$, nHaP, AND HYBRID) AS EMBOLIC AGENTS

1) Nano barium sulphate particles having the crystallite size of 2-5 nm and nano-hydroxyapatite particles of about 65 nm are successfully synthesized.

2) The shape fixity of pure polymer and its composites prepared through compression moulding technique is not influenced by the fillers and it is found to be in the range of 96-98%.

3) The shape recovery of all the samples is increased during the 2nd shape recovery cycle compared to the 1st recovery cycle.

4) The shape recovery of the composites is decreased with increasing concentration of the fillers.

5) The nano $BaSO_4$ composite showed a better shape recovery than the hydroxyapatite and hybrid composites at the same weight fraction of fillers.

6) The volume and rate of shape recovery are significantly influenced by the programming temperature of the temporary shape of the product. A lower programming temperature favours a higher volume and rate of recovery.

7) Irrespective of the filler and its concentration, the addition of filler is found to decrease the mechanical properties of SMPU composites.

8) The glass transition temperature of the nano $BaSO_4$ and hybrid composites is not found to be significantly influenced by the fillers.

9) The presence of moisture significantly influences the T_g of the SMPU MM 3520 and its composites.

10) The 10 wt% and 12.5 wt% nano $BaSO_4$ composite showed radiopacity at par with 1mm thick Aluminium plate, confirming their suitability for medical applications.

11) The 10wt% nano $BaSO_4$ composite is found to be ideal choice to fabricate as an embolic agent through the novel processing technique.

7.4 PRELIMINARY BIOCOMPATIBILITY STUDIES

1) The SMPU and its composites tested in the present study have not shown any cytotoxicity in L132 and HaCat cell line. However, the porous 3D printed Tungsten (7wt%) SMP composite elicited cytotoxic characteristics at the concentration of 5 µg/ml and 10 µg/ml in the HaCat cells. Thus, the said composite is not desirable as an embolic agent using the proposed fabrication technique.

2) Higher albumin to fibrinogen adsorption ratio (A:F) of SMPU, nano Barium sulphate composite, nano-hydroxyapatite composite, and hybrid composites indicates a lesser

probability of thrombosis or coagulation, making them suitable for blood-contacting implants such as embolic agents.

7.5 3D PRINTED POROUS nBaSO$_4$ SMPC AS AN EMBOLIC AGENT FOR INTERVENTIONAL RADIOLOGY TECHNIQUES

1) The glass transition temperature of 3D printed porous nano $BaSO_4$ composites is found to be nearly the same as that of the compression-molded SMPU product.
2) The storage modulus of the nano $BaSO_4$ SMPC in the rubbery state is identical to that of the elastic modulus of the wall of an abdominal aortic aneurysm, and thus, it is safe to use the material for the proposed application.
3) The addition of 10wt% nano $BaSO_4$ to the SMPU increased its visibility under X-ray fluoroscopy, making it suitable for easy tracking during the embolization process.
4) The porosity of the 10wt% $BaSO_4$ SMPC obtained from the experimental studies and theoretically estimated values is found to be very close to each other, which confirmed that the porogen used while preparing the composites is completely removed during the leaching process.
5) The porous SMPC recovered within the aneurysm model after delivery and filled in the aneurysm sack in the in-house developed simulator model confirming the viability of SMPC to be used as an embolic agent for the endovascular embolization.

7.6 FUTURE SCOPE OF THE WORK

The findings obtained from the present work suggest further development of patient-specific SMPC as an alternate for the presently used embolic agents. An outline of the scope of future research for improving the product is given below:

1) The effect of different sterilization techniques and irradiation dose on the material characteristics including that of shape memory effect of SMP and its composites is required to be studied.
2) The effect of the long-term contact to blood/body fluids on the material properties of the developed SMPC is required to be studied.
3) The shape recovery, recovery stress, and shape recovery rate at different programming temperatures are needed to be studied on SMPC before and after the sterilization process for better control during delivery of the embolic agent.
4) An alternate material to substitute NaCl as a porogen may be explored.
5) The effects of long-time storage and polymer degradation on the mechanical, thermomechanical, and shape memory characteristics of 3D printed SMPC are required to be studied.
6) A complete biocompatibility study according to the ISO 10993, followed by *in vivo* studies in animals and human beings, is required to be performed.

REFERENCES

[1] Medical Device-Full Definition, WHO Med. Device Tech. Ser. (2020). https://www.who.int/medical_devices/full_deffinition/en/ (accessed September 28, 2020).

[2] P. Stephanie Allen, D.R. Hammett, E. de Vettori, L. Purdy, Z. Qun, S. Krolop, C. Sehgal, Y. Wada, M. Van Bergen, A. Suboh, D.W.C. Loke, S. Siegel, S. Burrill, 2019 Global health care outlook: Shaping the future, 2019. https://www2.deloitte.com/content/dam/Deloitte/global/Documents/Life-Sciences-Health-Care/gx-lshc-hc-outlook-2019.pdf.

[3] Medical Devices Market Global Opportunities And Strategies, (2020). https://www.thebusinessresearchcompany.com/report/medical-devices-market (accessed July 26, 2020).

[4] Indian Healthcare Industry Analysis, (2020). https://www.ibef.org/industry/healthcare-presentation (accessed February 1, 2020).

[5] BT Buzz: Make in India flops for medical devices; domestic firms shutting shops to import, (2019). https://www.businesstoday.in/bt-buzz/news/bt-buzz-make-in-india-flops-for-medical-devices-domestic-firms-shutting-shops-to-import/story/365885.html (accessed February 1, 2020).

[6] J. Sharma, M. Gupta, N. Bharadwaj, J. Raj, Medical devices: Manufacturing in India A sunrise, (2016). http://www.bls.gov/fls/india.htm.

[7] Biomaterials - Journal - Elsevier, (2020). https://www.journals.elsevier.com/biomaterials (accessed October 13, 2020).

[8] D.F. Williams, On the mechanisms of biocompatibility, Biomaterials. 29 (2008) 2941–2953. https://doi.org/10.1016/j.biomaterials.2008.04.023.

[9] ISO 10993-1:2018(en), Biological evaluation of medical devices — Part 1: Evaluation and testing within a risk management process, (n.d.). https://www.iso.org/obp/ui#iso:std:iso:10993:-1:ed-5:v2:en (accessed April 9, 2021).

[10] Wilhelm Conrad Röntgen - Biographical, (n.d.). https://www.nobelprize.org/prizes/physics/1901/rontgen/biographical/ (accessed August 1, 2020).

[11] L.M. Allen, A.M. Fowler, C. Walker, C.P. Derdeyn, B. V. Nguyen, A.N. Hasso, B. V. Ghodke, G.J. Zipfel, D.T. Cross, C.J. Moran, Retrospective review of cerebral mycotic aneurysms in 26 patients: Focus on treatment in strongly immunocompromised patients with a brief literature review, Am. J. Neuroradiol. 34 (2013) 823–827. https://doi.org/10.3174/ajnr.A3302.

[12] D.O. Wiebers, J. Whisnant, J.I. Huston, I. Meissner, R.J. Brown, D. Piepgras, G. Forbes, K. Thielen, D. Nichols, W. O'Fallon, J. Peacock, L. Jaeger, N. Kassell, G. Kongable-Beckman, J. Torner, Unruptured intracranial aneurysms: Natural history, clinical outcome, and risks of surgical and endovascular treatment, Lancet. 362 (2003) 103–110. https://doi.org/10.1016/S0140-6736(03)13860-3.

[13] Cerebral Aneurysm – Symptoms, Diagnosis and Treatments, (2020). https://www.aans.org/en/Patients/Neurosurgical-Conditions-and-Treatments/Cerebral-Aneurysm (accessed October 13, 2020).

[14] Statistics and Facts - Brain Aneurysm Foundation, (2020). https://bafound.org/about-brain-aneurysms/brain-aneurysm-basics/brain-aneurysm-statistics-and-facts/ (accessed October 13, 2020).

[15] Abdominal aortic aneurysms: Triple A, double trouble, Harvard Men Heal. (n.d.). https://www.health.harvard.edu/heart-health/abdominal-aortic-aneurysms-triple-a-double-trouble (accessed October 14, 2020).

[16] D.P.J. Howard, A. Banerjee, J.F. Fairhead, A. Handa, L.E. Silver, P.M. Rothwell, Population-Based Study of Incidence of Acute Abdominal Aortic Aneurysms With Projected Impact of Screening Strategy, J. Am. Heart Assoc. 4 (2015) e001926. https://doi.org/10.1161/JAHA.115.001926.

[17] E.M. Isselbacher, Thoracic and abdominal aortic aneurysms, Circulation. 111 (2005) 816–828. https://doi.org/10.1161/01.CIR.0000154569.08857.7A.

[18] A. Kurtelius, N. Väntti, B. Rezai Jahromi, O. Tähtinen, H. Manninen, J. Koskenvuo, R. Tulamo, S. Kotikoski, H. Nurmonen, O.P. Kämäräinen, T. Huttunen, J. Huttunen, M. von Und Zu Fraunberg, T. Koivisto, J.E. Jääskeläinen, A.E. Lindgren, Association of Intracranial Aneurysms With Aortic Aneurysms in 125 Patients With Fusiform and 4253 Patients With Saccular Intracranial Aneurysms and Their Family Members and Population Controls, J. Am. Heart Assoc. 8 (2019) e013277. https://doi.org/10.1161/JAHA.119.013277.

[19] K.C. Kent, Abdominal aortic aneurysms, N. Engl. J. Med. 371 (2014) 2101–2108. https://doi.org/10.1056/NEJMcp1401430.

[20] S.B. Carr, G. Imbarrato, R.E. Breeze, C.C. Wilkinson, Clip ligation for ruptured intracranial aneurysm in a child with Loeys-Dietz syndrome: Case report, J. Neurosurg. Pediatr. 21 (2018) 375–379. https://doi.org/10.3171/2017.10.PEDS17193.

[21] M.M. Taha, I. Nakahara, T. Higashi, Y. Iwamuro, M. Iwaasa, Y. Watanabe, K. Tsunetoshi, T. Munemitsu, Endovascular embolization vs surgical clipping in treatment of cerebral aneurysms: morbidity and mortality with short-term outcome, Surg. Neurol. 66 (2006) 277–284. https://doi.org/10.1016/j.surneu.2005.12.031.

[22] A.J. Molyneux, R.S. Kerr, L.M. Yu, M. Clarke, M. Sneade, J.A. Yarnold, P. Sandercock, International Subarachnoid Aneurysm Trial (ISAT) of neurosurgical clipping versus endovascular coiling in 2143 patients with ruptured intracranial aneurysms: A randomised comparison of effects on survival, dependency, seizures, rebleeding, subgroups, and , Lancet. 366 (2005) 809–817. https://doi.org/10.1016/S0140-6736(05)67214-5.

[23] G. Guglielmi, History of endovascular endosaccular occlusion of brain aneurysms: 1965-1990, Interv. Neuroradiol. 13 (2007) 217–224. https://doi.org/10.1177/159101990701300301.

[24] R. Loffroy, B. Guiu, J.-P. Cercueil, D. Krause, Endovascular Therapeutic Embolisation: An Overview of Occluding Agents and their Effects on Embolised Tissues, Curr. Vasc. Pharmacol. 7 (2009) 250–263. https://doi.org/10.2174/157016109787455617.

[25] M.T. Lawton, W.C. Rutledge, H. Kim, C. Stapf, K.J. Whitehead, D.Y. Li, T. Krings, K. TerBrugge, D. Kondziolka, M.K. Morgan, K. Moon, R.F. Spetzler, Brain arteriovenous malformations, Nat. Rev. Dis. Prim. 1 (2015) 1–21. https://doi.org/10.1038/nrdp.2015.8.

[26] J.J. Leyon, T. Littlehales, B. Rangarajan, E.T. Hoey, A. Ganeshan, Endovascular Embolization: Review of Currently Available Embolization Agents, Curr. Probl. Diagn. Radiol. 43 (2014) 35–53. https://doi.org/10.1067/j.cpradiol.2013.10.003.

[27] Y. Wei, S. Cotin, J. Allard, L. Fang, C. Pan, S. Ma, Interactive blood-coil simulation in real-time during aneurysm embolization, Comput. Graph. 35 (2011) 422–430. https://doi.org/10.1016/j.cag.2011.01.010.

[28] C. Gianturco, J.H. Anderson, S. Wallace, Mechanical device for arterial occulsion, Am.

J. Roentgenol. Radium Ther. Nucl. Med. 124 (1975) 428–435. https://doi.org/10.2214/ajr.124.3.428.

[29] J.B. White, C.G.M. Ken, H.J. Cloft, D.F. Kallmes, Coils in a nutshell: A review of coil physical properties, Am. J. Neuroradiol. 29 (2008) 1242–1246. https://doi.org/10.3174/ajnr.A1067.

[30] S. Ramakrishnan, Vascular plugs - A key companion to Interventionists - "Just Plug it," Indian Heart J. 67 (2015) 399–405. https://doi.org/10.1016/j.ihj.2015.07.001.

[31] C.M. Hassan, N.A. Peppas, Structure and applications of poly(vinyl alcohol) hydrogels produced by conventional crosslinking or by freezing/thawing methods, in: Biopolym. · PVA Hydrogels, Anionic Polym. Nanocomposites, Adv. Polym. Sci., Springer, Berlin, Heidelberg, 2000: pp. 37–65. https://doi.org/10.1007/3-540-46414-x_2.

[32] E.A. Stewart, S.K. Laughlin-Tommaso, W.H. Catherino, S. Lalitkumar, D. Gupta, B. Vollenhoven, Uterine fibroids, Nat. Rev. Dis. Prim. 2 (2016). https://doi.org/10.1038/nrdp.2016.43.

[33] M. Guimaraes, D. Arrington, T. MacFall, R. Yamada, C. Schonholz, Does Material Matter ?, Endovasc. Today. 54 (2013) 70–74. https://doi.org/10.1051/epjconf/201714016003.

[34] A. Poursaid, M.M. Jensen, E. Huo, H. Ghandehari, Polymeric materials for embolic and chemoembolic applications, J. Control. Release. 240 (2016) 414–433. https://doi.org/10.1016/j.jconrel.2016.02.033.

[35] Harry Coover | Lemelson, (n.d.). https://lemelson.mit.edu/resources/harry-coover (accessed April 10, 2021).

[36] A. Prashar, S. Butt, N. Shaida, Introducing phil (Precipitating hydrophobic injectable liquid) – A new embolic agent for the body interventional radiologist, Diagnostic Interv. Radiol. 26 (2020) 140–142. https://doi.org/10.5152/dir.2019.19063.

[37] J. Hu, H. Albadawi, B.W. Chong, A.R. Deipolyi, R.A. Sheth, A. Khademhosseini, R. Oklu, Advances in Biomaterials and Technologies for Vascular Embolization, Adv. Mater. 1901071 (2019) 1–52. https://doi.org/10.1002/adma.201901071.

[38] C.L. Ventola, Medical Applications for 3D Printing: Current and Projected Uses., P T. 39 (2014) 704–711. https://doi.org/10.1016/j.infsof.2008.09.005.

[39] A.A. Giannopoulos, D. Mitsouras, S.-J. Yoo, P.P. Liu, Y.S. Chatzizisis, F.J. Rybicki, Applications of 3D printing in cardiovascular diseases, Nat. Rev. Cardiol. 13 (2016) 701–718. https://doi.org/10.1038/nrcardio.2016.170.

[40] ASTM International, Standard Terminology for Additive Manufacturing Technologies, ASTM Stand. F2792 − 12 (2012) 1–3. https://doi.org/10.1520/F2792-12A.2.

[41] EPO - Charles W. Hull (USA), (n.d.). https://www.epo.org/news-events/events/european-inventor/finalists/2014/hull.html (accessed April 10, 2021).

[42] Wohlers Associates, (n.d.). http://www.wohlersassociates.com/press65.html (accessed February 16, 2021).

[43] M. Attaran, The rise of 3-D printing: The advantages of additive manufacturing over traditional manufacturing, Bus. Horiz. 60 (2017) 677–688. https://doi.org/10.1016/j.bushor.2017.05.011.

[44] S. Ambekar, Need for brain aneurysm treatment registry of India: How effectively are we treating intracranial aneurysms in India?, Neurol. India. 63 (2015) 290. https://doi.org/10.4103/0028-3886.156322.

[45] G.A. Kuzmik, A.X. Sang, J.A. Elefteriades, Natural history of thoracic aortic aneurysms, J. Vasc. Surg. 56 (2012) 565–571. https://doi.org/10.1016/j.jvs.2012.04.053.

[46] M. Lubarsky, C.E. Ray, B. Funaki, Embolization agents-which one should be used when? Part 1: Large-vessel embolization, Semin. Intervent. Radiol. 26 (2009) 352–357. https://doi.org/10.1055/s-0029-1242206.

[47] F. Zhou, L. Chen, Q. An, L. Chen, Y. Wen, F. Fang, W. Zhu, T. Yi, Novel Hydrogel Material as a Potential Embolic Agent in Embolization Treatments, Sci. Rep. 6 (2016) 1–11. https://doi.org/10.1038/srep32145.

[48] K.C. Liu, D. Ding, R.M. Starke, S.R. Geraghty, M.E. Jensen, Intraprocedural retrieval of migrated coils during endovascular aneurysm treatment with the Trevo Stentriever device, J. Clin. Neurosci. 21 (2014) 503–506. https://doi.org/10.1016/j.jocn.2013.10.012.

[49] E.H. Brilstra, G.J.E. Rinkel, Y. Van Der Graaf, W.J.J. Van Rooij, A. Algra, Treatment of intracranial aneurysms by embolization with coils: A systematic review, Stroke. 30 (1999) 470–476. https://doi.org/10.1161/01.STR.30.2.470.

[50] H.J. Cloft, D.F. Kallmes, Cerebral aneurysm perforations complicating therapy with Guglielmi detachable coils: A meta-analysis, Am. J. Neuroradiol. 23 (2002) 1706–1709.

[51] W. Brinjikji, D.F. Kallmes, R. Kadirvel, Mechanisms of healing in coiled intracranial aneurysms: A review of the literature, Am. J. Neuroradiol. 36 (2015) 1216–1222. https://doi.org/10.3174/ajnr.A4175.

[52] K.H. Barth, J.D. Strandberg, S.L. Kaufman, R.I. White, Chronic vascular reactions to steel coil occlusion devices, Am. J. Roentgenol. 131 (1978) 455–458. https://doi.org/10.2214/ajr.131.3.455.

[53] D. Fiorella, F.C. Albuquerque, C.G. McDougall, Durability of aneurysm embolization with matrix detachable coils, Neurosurgery. 58 (2006) 51–58. https://doi.org/10.1227/01.NEU.0000194190.45595.9E.

[54] W.J. Van Rooij, A.N. De Gast, M. Sluzewski, Results of 101 aneurysms treated with polyglycolic/polylactic acid microfilament nexus coils compared with historical controls treated with standard coils, Am. J. Neuroradiol. 29 (2008) 991–996. https://doi.org/10.3174/ajnr.A1021.

[55] B. Gory, F. Turjman, Endovascular treatment of 404 intracranial aneurysms treated with nexus detachable coils: Short-term and mid-term results from a prospective, consecutive, European multicenter study, Acta Neurochir. (Wien). 156 (2014) 831–837. https://doi.org/10.1007/s00701-014-2047-3.

[56] H.J. Cloft, HydroCoil for Endovascular Aneurysm Occlusion (HEAL) Study: Periprocedural Results, Am. J. Neuroradiol. 27 (2006) 289–292.

[57] H.J. Cloft, HydroCoil for Endovascular Aneurysm Occlusion (HEAL) Study: 3–6 Month Angiographic Follow-Up Results, Am. J. Neuroradiol. 28 (2007) 152–154.

[58] S.H. Im, M.H. Han, B.J. Kwon, C. Jung, J.E. Kim, D.H. Han, Aseptic meningitis after embolization of cerebral aneurysms using hydrogel-coated coils: Report of three cases, Am. J. Neuroradiol. 28 (2007) 511–512.

[59] S. Vaidya, K.R. Tozer, J. Chen, An overview of embolic agents, Semin. Intervent. Radiol. 25 (2008) 204–215. https://doi.org/10.1055/s-0028-1085930.

[60] A.K. Wakhloo, M.J. Gounis, F. Massari, A.S. Puri, Endovascular Treatment of Cerebral Aneurysms, in: J. Grotta, G. Albers, J. Broderick, S. Kasner, E. Lo, D. Mendelow, R. Sacco, L. Wong (Eds.), Stroke Pathophysiol. Diagnosis, Manag., Sixth Edit, Elsevier,

2002: pp. 1071-1088.e6. https://doi.org/10.1016/B978-0-323-29544-4.00066-9.

[61] M. Sluzewski, W.J. Van Rooij, G.N. Beute, P.C. Nijssen, Balloon-assisted coil embolization of intracranial aneurysms: Incidence, complications, and angiography results, J. Neurosurg. 105 (2006) 396–399. https://doi.org/10.3171/jns.2006.105.3.396.

[62] J.E. Lopera, The Amplatzer Vascular Plug: Review of Evolution and Current Applications, Semin. Intervent. Radiol. 32 (2015) 356–369. https://doi.org/10.1055/s-0035-1564810.

[63] S. Tadavarthy, J. Moller, K. Amplatz, Polyvinyl Alcohol (Ivalon)- A new embolic material, Am. J. Roentgenol. 125 (1975) 609–616. https://doi.org/10.2214/ajr.125.3.609.

[64] B.L. Vernon, C. Riley, Vascular applications of injectable biomaterials, in: B.L. Vernon (Ed.), Inject. Biomater., Elsevier BV, 2011: pp. 183–201. https://doi.org/10.1533/9780857091376.2.183.

[65] X.J. Lu, Y. Zhang, D.C. Cui, W.J. Meng, L.R. Du, H.T. Guan, Z.Z. Zheng, N.Q. Fu, T.S. Lv, L. Song, Y.H. Zou, W.L. Lu, T.Y. Fan, Research of novel biocompatible radiopaque microcapsules for arterial embolization, Int. J. Pharm. 452 (2013) 211–219. https://doi.org/10.1016/j.ijpharm.2013.05.001.

[66] A. Gruber, P.R. Mazal, G. Bavinzski, M. Killer, H. Budka, B. Richling, Repermeation of partially embolized cerebral arteriovenous malformations: A clinical, radiologic, and histologic study, Am. J. Neuroradiol. 17 (1996) 1323–1331.

[67] A. Casasco, E. Houdart, A. Biondi, H.S. Jhaveri, D. Herbreteau, A. Aymard, J.J. Merland, Major Complications of Percutaneous Embolization of Skull-Base Tumors, Am. J. Neuroradiol. 20 (1999) 179–181.

[68] J.S. Pollak, J. White, The use of cyanoacrylate adhesives in peripheral embolization, J. Vasc. Interv. Radiol. 12 (2001) 907–913. https://doi.org/10.1016/S1051-0443(07)61568-1.

[69] G.J. Velat, J.F. Reavey-Cantwell, C. Sistrom, D. Smullen, G.L. Fautheree, J. Whiting, S.B. Lewis, R.A. Mericle, C.S. Firment, B.L. Hoh, Comparison of N-butyl cyanoacrylate and onyx for the embolization of intracranial arteriovenous malformations: Analysis of fluoroscopy and procedure times, Neurosurgery. 63 (2008) 73–80. https://doi.org/10.1227/01.NEU.0000320136.05677.91.

[70] O. Henrikson, H. Roos, M. Falkenberg, Ethylene vinyl alcohol copolymer (Onyx) to seal type 1 endoleak. A new technique, Vascular. 19 (2011) 77–81. https://doi.org/10.1258/vasc.2010.oa0257.

[71] R. Müller-Wille, P. Heiss, T. Herold, E.M. Jung, A.G. Schreyer, O.W. Hamer, J. Rennert, P. Hoffstetter, C. Stroszczynski, N. Zorger, Endovascular treatment of acute arterial hemorrhage in trauma patients using ethylene vinyl alcohol copolymer (Onyx), Cardiovasc. Intervent. Radiol. 35 (2012) 65–75. https://doi.org/10.1007/s00270-011-0134-x.

[72] Y. Murayama, F. Vinuela, S. Tateshima, J. Vinuela F., Y. Akiba, Endovascular treatment of experimental aneurysms by use of a combination of liquid embolic agents and protective devices, Am. J. Neuroradiol. 21 (2000) 1726–1735.

[73] Y. Murayama, F. Viñuela, A. Ulhoa, Y. Akiba, G.R. Duckwiler, Y.P. Gobin, H. V. Vinters, R.J. Greff, Nonadhesive liquid embolic agent for cerebral arteriovenous malformations: Preliminary histopathological studies in swine rete mirabile, Neurosurgery. 43 (1998) 1164–1172. https://doi.org/10.1097/00006123-199811000-00081.

[74] H.S. Cekirge, I. Saatci, M.H. Ozturk, B. Cil, A. Arat, M. Mawad, F. Ergungor, D. Belen, U. Er, S. Turk, M. Bavbek, Z. Sekerci, E. Beskonakli, O.E. Ozcan, T. Ozgen, Late angiographic and clinical follow-up results of 100 consecutive aneurysms treated with Onyx reconstruction: Largest single-center experience, Neuroradiology. 48 (2006) 113–126. https://doi.org/10.1007/s00234-005-0007-6.

[75] J.J. Leyon, S. Chavda, A. Thomas, S. Lamin, Preliminary experience with the liquid embolic material agent PHIL (Precipitating Hydrophobic Injectable Liquid) in treating cranial and spinal dural arteriovenous fi stulas : technical note, (2015) 1–8. https://doi.org/10.1136/neurintsurg-2015-011684.

[76] P. Singhal, W. Small, E. Cosgriff-Hernandez, D.J. Maitland, T.S. Wilson, Low density biodegradable shape memory polyurethane foams for embolic biomedical applications, Acta Biomater. 10 (2014) 67–76. https://doi.org/10.1016/j.actbio.2013.09.027.

[77] D.J. Maitland, W. Small, J.M. Ortega, P.R. Buckley, J. Rodriguez, J. Hartman, T.S. Wilson, Prototype laser-activated shape memory polymer foam device for embolic treatment of aneurysms, J. Biomed. Opt. 12 (2007) 030504. https://doi.org/10.1117/1.2743983.

[78] W. Small IV, P.R. Buckley, T.S. Wilson, W.J. Benett, J. Hartman, D. Saloner, D.J. Maitland, Shape memory polymer stent with expandable foam: A new concept for endovascular embolization of fusiform aneurysms, IEEE Trans. Biomed. Eng. 54 (2007) 1157–1160. https://doi.org/10.1109/TBME.2006.889771.

[79] T.L. Landsman, R.L. Bush, A. Glowczwski, J. Horn, S.L. Jessen, E. Ungchusri, K. Diguette, H.R. Smith, S.M. Hasan, D. Nash, F.J. Clubb, D.J. Maitland, Design and verification of a shape memory polymer peripheral occlusion device, J. Mech. Behav. Biomed. Mater. 63 (2016) 195–206. https://doi.org/10.1016/j.jmbbm.2016.06.019.

[80] M.D. Hager, S. Bode, C. Weber, U.S. Schubert, Shape memory polymers: Past, present and future developments, Prog. Polym. Sci. 49–50 (2015) 3–33. https://doi.org/10.1016/j.progpolymsci.2015.04.002.

[81] T. Xie, Recent advances in polymer shape memory, Polymer (Guildf). 52 (2011) 4985–5000. https://doi.org/10.1016/j.polymer.2011.08.003.

[82] A. Lendlein, R. Langer, Biodegradable, elastic shape-memory polymers for potential biomedical applications, Science (80-.). 296 (2002) 1673–1676. https://doi.org/10.1126/science.1066102.

[83] A. Metcalfe, A.C. Desfaits, I. Salazkin, L. Yahia, W.M. Sokolowski, J. Raymond, Cold hibernated elastic memory foams for endovascular interventions, Biomaterials. 24 (2003) 491–497. https://doi.org/10.1016/S0142-9612(02)00362-9.

[84] L. De Nardo, R. Alberti, A. Cigada, L. Yahia, M.C. Tanzi, S. Farè, Shape memory polymer foams for cerebral aneurysm reparation: Effects of plasma sterilization on physical properties and cytocompatibility, Acta Biomater. 5 (2009) 1508–1518. https://doi.org/10.1016/j.actbio.2008.11.017.

[85] L. De Nardo, S. Bertoldi, M.C. Tanzi, H.J. Haugen, S. Farè, Shape memory polymer cellular solid design for medical applications, Smart Mater. Struct. 20 (2011) 035004. https://doi.org/10.1088/0964-1726/20/3/035004.

[86] P. Singhal, J.N. Rodriguez, W. Small, S. Eagleston, J. Van De Water, D.J. Maitland, T.S. Wilson, Ultra low density and highly crosslinked biocompatible shape memory polyurethane foams, J. Polym. Sci. Part B Polym. Phys. 50 (2012) 724–737. https://doi.org/10.1002/polb.23056.

[87] P. Singhal, A. Boyle, M.L. Brooks, S. Infanger, S. Letts, W. Small, D.J. Maitland, T.S.

Wilson, Controlling the Actuation Rate of Low-Density Shape-Memory Polymer Foams in Water, Macromol. Chem. Phys. 214 (2013) 1–7. https://doi.org/10.1038/jid.2014.371.

[88] J.N. Rodriguez, F.J. Clubb, T.S. Wilson, M.W. Miller, T.W. Fossum, J. Hartman, E. Tuzun, P. Singhal, D.J. Maitland, In vivo response to an implanted shape memory polyurethane foam in a porcine aneurysm model, J. Biomed. Mater. Res. - Part A. 102 (2014) 1231–1242. https://doi.org/10.1002/jbm.a.34782.

[89] W. Hwang, P. Singhal, M.W. Miller, D.J. Maitland, In vitro study of transcatheter delivery of a shape memory polymer foam embolic device for treating cerebral aneurysms, J. Med. Devices, Trans. ASME. 7 (2013) 6–7. https://doi.org/10.1115/1.4024338.

[90] J.N. Rodriguez, Y.J. Yu, M.W. Miller, T.S. Wilson, J. Hartman, F.J. Clubb, B. Gentry, D.J. Maitland, Opacification of shape memory polymer foam designed for treatment of intracranial aneurysms, Ann. Biomed. Eng. 40 (2012) 883–897. https://doi.org/10.1007/s10439-011-0468-1.

[91] J. Horn, W. Hwang, S.L. Jessen, B.K. Keller, M.W. Miller, E. Tuzun, J. Hartman, F.J. Clubb, D.J. Maitland, Comparison of shape memory polymer foam versus bare metal coil treatments in an in vivo porcine sidewall aneurysm model, J. Biomed. Mater. Res. - Part B Appl. Biomater. 105 (2017) 1892–1905. https://doi.org/10.1002/jbm.b.33725.

[92] S.M. Herting, Y. Ding, A.J. Boyle, D. Dai, L.D. Nash, S. Asnafi, D.R. Jakaitis, C.R. Johnson, L.M. Graul, C. Yeh, D.F. Kallmes, R. Kadirvel, D.J. Maitland, In vivo comparison of shape memory polymer foam-coated and bare metal coils for aneurysm occlusion in the rabbit elastase model, J. Biomed. Mater. Res. - Part B Appl. Biomater. 107 (2019) 2466–2475. https://doi.org/10.1002/jbm.b.34337.

[93] J. Ortega, D. Maitland, T. Wilson, W. Tsai, Ö. Savaş, D. Saloner, Vascular dynamics of a shape memory polymer foam aneurysm treatment technique, Ann. Biomed. Eng. 35 (2007) 1870–1884. https://doi.org/10.1007/s10439-007-9358-y.

[94] W. Hwang, B.L. Volk, F. Akberali, P. Singhal, J.C. Criscione, D.J. Maitland, Estimation of aneurysm wall stresses created by treatment with a shape memory polymer foam device, Biomech. Model. Mechanobiol. 11 (2012) 715–729. https://doi.org/10.1007/s10237-011-0345-8.

[95] J.M. Hampikian, B.C. Heaton, F.C. Tong, Z. Zhang, C.P. Wong, Mechanical and

radiographic properties of a shape memory polymer composite for intracranial aneurysm coils, Mater. Sci. Eng. C. 26 (2006) 1373–1379. https://doi.org/10.1016/j.msec.2005.08.026.

[96] A. Ricker, T.J. Webster, The influence of nano MgO and BaSO 4 particle size additives on properties of PMMA bone cement, Int. J. Nanomedicine. 3 (2008) 125–132. https://doi.org/10.2147/IJN.S2322.

[97] I.C. Romero-Ibarra, E. Bonilla-Blancas, A. Sánchez-Solís, O. Manero, Influence of the morphology of barium sulfate nanofibers and nanospheres on the physical properties of polyurethane nanocomposites, Eur. Polym. J. 48 (2012) 670–676. https://doi.org/10.1016/j.eurpolymj.2012.01.001.

[98] G.E. Aninwene II, D. Stout, Y. Zifan, T.J. Webster, Nano-BaSO 4 : a novel antimicrobial additive to pellethane, Int. J. Nanomedicine. 8 (2013) 1197–1205. https://doi.org/10.2147/IJN.S40300.

[99] J. Cui, K. Kratz, M. Heuchel, B. Hiebl, A. Lendlein, Mechanically active scaffolds from radio-opaque shape-memory polymer-based composites, Polym. Adv. Technol. 22 (2011) 180–189. https://doi.org/10.1002/pat.1733.

[100] A.C. Weems, J.E. Raymond, K.T. Wacker, T.P. Gustafson, B. Keller, K.L. Wooley, D.J. Maitland, Examination of radio-opacity enhancing additives in shape memory polyurethane foams, J. Appl. Polym. Sci. 132 (2015) 17–25. https://doi.org/10.1002/app.42054.

[101] S.M. Hasan, G. Harmon, F. Zhou, J.E. Raymond, T.P. Gustafson, T.S. Wilson, D.J. Maitland, Tungsten-loaded SMP foam nanocomposites with inherent radiopacity and tunable thermo-mechanical properties, Polym. Adv. Technol. 27 (2016) 195–203. https://doi.org/10.1002/pat.3621.

[102] X. Kuang, D.J. Roach, J. Wu, C.M. Hamel, Z. Ding, T. Wang, M.L. Dunn, H.J. Qi, Advances in 4D Printing: Materials and Applications, Adv. Funct. Mater. 29 (2019) 1–23. https://doi.org/10.1002/adfm.201805290.

[103] J. Wu, C. Yuan, Z. Ding, M. Isakov, Y. Mao, T. Wang, M.L. Dunn, H.J. Qi, Multi-shape active composites by 3D printing of digital shape memory polymers, Sci. Rep. 6 (2016) 24224. https://doi.org/10.1038/srep24224.

[104] Q. Ge, A.H. Sakhaei, H. Lee, C.K. Dunn, N.X. Fang, M.L. Dunn, Multimaterial 4D

Printing with Tailorable Shape Memory Polymers, Sci. Rep. 6 (2016) 31110. https://doi.org/10.1038/srep31110.

[105] Q. Zhang, D. Yan, K. Zhang, G. Hu, Pattern Transformation of Heat-Shrinkable Polymer by Three-Dimensional (3D) Printing Technique, Sci. Rep. 5 (2015) 24–27. https://doi.org/10.1038/srep08936.

[106] Y. Liu, W. Zhang, F. Zhang, X. Lan, J. Leng, S. Liu, X. Jia, C. Cotton, B. Sun, B. Gu, T.W. Chou, Shape memory behavior and recovery force of 4D printed laminated Miura-origami structures subjected to compressive loading, Compos. Part B Eng. 153 (2018) 233–242. https://doi.org/10.1016/j.compositesb.2018.07.053.

[107] S. Yuan, J. Bai, C. Kai Chua, K. Zhou, J. Wei, Characterization of Creeping and Shape Memory Effect in Laser Sintered Thermoplastic Polyurethane, J. Comput. Inf. Sci. Eng. 16 (2016) 041007. https://doi.org/10.1115/1.4034032.

[108] J.Z. Gul, M. Sajid, M.M. Rehman, G.U. Siddiqui, I. Shah, K.H. Kim, J.W. Lee, K.H. Choi, 3D printing for soft robotics–a review, Sci. Technol. Adv. Mater. 19 (2018) 243–262. https://doi.org/10.1080/14686996.2018.1431862.

[109] J. Raasch, M. Ivey, D. Aldrich, D.S. Nobes, C. Ayranci, Characterization of polyurethane shape memory polymer processed by material extrusion additive manufacturing, Addit. Manuf. 8 (2015) 132–141. https://doi.org/10.1016/j.addma.2015.09.004.

[110] Y. Yang, Y. Chen, Y. Wei, Y. Li, 3D printing of shape memory polymer for functional part fabrication, Int. J. Adv. Manuf. Technol. 84 (2016) 2079–2095. https://doi.org/10.1007/s00170-015-7843-2.

[111] H. Yang, W.R. Leow, T. Wang, J. Wang, J. Yu, K. He, D. Qi, C. Wan, X. Chen, 3D Printed Photoresponsive Devices Based on Shape Memory Composites, Adv. Mater. 29 (2017) 1–7. https://doi.org/10.1002/adma.201701627.

[112] H.P. Hentze, M. Antonietti, Porous polymers and resins for biotechnological and biomedical applications, Rev. Mol. Biotechnol. 90 (2002) 27–53. https://doi.org/10.1016/S1389-0352(01)00046-0.

[113] X. Mu, T. Bertron, C. Dunn, H. Qiao, J. Wu, Z. Zhao, C. Saldana, H.J. Qi, Porous polymeric materials by 3D printing of photocurable resin, Mater. Horiz. 4 (2017) 442–449. https://doi.org/10.1039/c7mh00084g.

[114] H. Shim, J.Y. Kim, A Study on Fabrication of 3D Dual Pore Scaffold by Fused Deposition Modeling and Salt-Leaching Method, Trans. Korean Soc. Mech. Eng. A. 39 (2015) 1229–1235. https://doi.org/http://dx.doi.org/10.3795/KSME-A.2015.39.12.1229.

[115] Shape Memory Polymer │ SMP Technologies Inc. │ DiAPLEX（ディアプレックス）, (n.d.). http://www2.smptechno.com/en/smp/index.html (accessed August 11, 2020).

[116] H. Janik, M. Marzec, A review: Fabrication of porous polyurethane scaffolds, Mater. Sci. Eng. C. 48 (2015) 586–591. https://doi.org/10.1016/j.msec.2014.12.037.

[117] O. Jordan, E. Doelker, D.A. Rüfenacht, Biomaterials used in injectable implants (liquid embolics) for percutaneous filling of vascular spaces, Cardiovasc. Intervent. Radiol. 28 (2005) 561–569. https://doi.org/10.1007/s00270-004-0238-7.

[118] S.D. Salman, Z.B. Leman, Physical, mechanical and ballistic properties of kenaf fiber reinforced poly vinyl butyral and its hybrid composites, Elsevier Ltd, 2018. https://doi.org/10.1016/B978-0-08-102160-6.00013-5.

[119] H. Tobushi, H. Hara, E. Yamada, S.S. Hayashi, T. H., H. Hara, E. Yamada, S.S. Hayashi, Thermomechanical properties in a thin film of shape memory polymer of polyurethane series, Smart Mater. Struct. 5 (1996) 483–491. https://doi.org/10.1088/0964-1726/5/4/012.

[120] T. Ohki, Q.Q. Ni, N. Ohsako, M. Iwamoto, Mechanical and shape memory behavior of composites with shape memory polymer, Compos. Part A Appl. Sci. Manuf. 35 (2004) 1065–1073. https://doi.org/10.1016/j.compositesa.2004.03.001.

[121] A. Shah Idil, N. Donaldson, The use of tungsten as a chronically implanted material, J. Neural Eng. 15 (2018). https://doi.org/10.1088/1741-2552/aaa502.

[122] T. Shimozuru, T. Kamezawa, J. Kuratsu, N. Sakai, I. Nagata, a Kishida, M. Akashi, M. Matsusaki, Hydroxyapatite and bFGF Coating of Detachable Coils for Endovascular Occlusion of Experimental Aneurysm., Interv. Neuroradiol. 9 (2003) 29–33. https://doi.org/10.1177/15910199010070S115.

[123] M. Kubo, N. Kuwayama, Y. Hirashima, A. Takaku, T. Ogawa, S. Endo, Hydroxyapatite ceramics as a particulate embolic material: Report of the physical properties of the hydroxyapatite particles and the animal study, Am. J. Neuroradiol. 24 (2003) 1540–1544.

[124] L. Song, L. Sun, N. Jiang, Z. Gan, Structural control and hemostatic properties of porous microspheres fabricated by hydroxyapatite-graft-poly(D,L-lactide) nanocomposites, Compos. Sci. Technol. 134 (2016) 234–241. https://doi.org/10.1016/j.compscitech.2016.09.001.

[125] T.M. Doherty, K. Asotra, L.A. Fitzpatrick, J.-H. Qiao, D.J. Wilkin, R.C. Detrano, C.R. Dunstan, P.K. Shah, T.B. Rajavashisth, Calcification in atherosclerosis: Bone biology and chronic inflammation at the arterial crossroads, Proc. Natl. Acad. Sci. 100 (2003) 11201–11206. https://doi.org/10.1073/pnas.1932554100.

[126] I.C. Romero-Ibarra, G. Rodríguez-Gattorno, M.F. García-Sánchez, A. Sánchez-Solís, O. Manero, Hierarchically nanostructured barium sulfate fibers, Langmuir. 26 (2010) 6954–6959. https://doi.org/10.1021/la904197k.

[127] G. Gergely, F. Wéber, I. Lukács, A.L. Tóth, Z.E. Horváth, J. Mihály, C. Balázsi, Preparation and characterization of hydroxyapatite from eggshell, Ceram. Int. 36 (2010) 803–806. https://doi.org/10.1016/j.ceramint.2009.09.020.

[128] M. Behl, A. Lendlein, Shape-memory polymers, Mater. Today. 10 (2007) 20–28. https://doi.org/10.1016/S1369-7021(07)70047-0.

[129] I.C. Romero-Ibarra, E. Bonilla-Blancas, A. Sánchez-Solís, O. Manero, Influence of X-ray opaque BaSO4 nanoparticles on the mechanical, thermal and rheological properties of polyoxymethylene nanocomposites, J. Polym. Eng. 32 (2012) 319–326. https://doi.org/10.1515/polyeng-2011-0135.

[130] S.Y. Fu, X.Q. Feng, B. Lauke, Y.W. Mai, Effects of particle size, particle/matrix interface adhesion and particle loading on mechanical properties of particulate-polymer composites, Compos. Part B Eng. 39 (2008) 933–961. https://doi.org/10.1016/j.compositesb.2008.01.002.

[131] J.J. Paszkowiak, A. Dardik, N. Haven, Arterial Wall Shear Stress : Observations from the Bench to the Bedside, Vasc. Endovascular Surg. 37 (2003) 47–57. https://doi.org/10.1177/153857440303700107.

[132] B. Yang, W.M. Huang, C. Li, L. Li, Effects of moisture on the thermomechanical properties of a polyurethane shape memory polymer, Polymer (Guildf). 47 (2006) 1348–1356. https://doi.org/10.1016/j.polymer.2005.12.051.

[133] Y. Yu, K. Hearon, T.S. Wilson, D.J. Maitland, The effect of moisture absorption on the

physical properties of polyurethane shape memory polymer foams, Smart Mater. Struct. 20 (2011) 085010. https://doi.org/10.1088/0964-1726/20/8/085010.

[134] M. Idicula, S.K. Malhotra, K. Joseph, S. Thomas, Dynamic mechanical analysis of randomly oriented intimately mixed short banana/sisal hybrid fibre reinforced polyester composites, Compos. Sci. Technol. 65 (2005) 1077–1087. https://doi.org/10.1016/j.compscitech.2004.10.023.

[135] B.J. Ash, R.W. Siegel, L.S. Schadler, Glass-transition temperature behavior of alumina/PMMA nanocomposites, J. Polym. Sci. Part B Polym. Phys. 42 (2004) 4371–4383. https://doi.org/10.1002/polb.20297.

[136] Q.Q. Ni, C. sheng Zhang, Y. Fu, G. Dai, T. Kimura, Shape memory effect and mechanical properties of carbon nanotube/shape memory polymer nanocomposites, Compos. Struct. 81 (2007) 176–184. https://doi.org/10.1007/s10803-012-1681-y.

[137] Á. Sonseca, O. Menes, E. Giménez, A comparative study of the mechanical, shape-memory, and degradation properties of poly(lactic acid) nanofiber and cellulose nanocrystal reinforced poly(mannitol sebacate) nanocomposites, RSC Adv. 7 (2017) 21869–21882. https://doi.org/10.1039/C7RA01256J.

[138] T. Xie, Tunable polymer multi-shape memory effect, Nature. 464 (2010) 267–270. https://doi.org/10.1038/nature08863.

[139] W. Li, J. Zhou, Y. Xu, Study of the in vitro cytotoxicity testing of medical devices, Biomed. Reports. 3 (2015) 617–620. https://doi.org/10.3892/br.2015.481.

[140] W.M. De Melo, W.M.A. Maximiano, A.A. Antunes, M.M. Beloti, A.L. Rosa, P.T. De Oliveira, Cytotoxicity testing of methyl and ethyl 2-cyanoacrylate using direct contact assay on osteoblast cell cultures, J. Oral Maxillofac. Surg. 71 (2013) 35–41. https://doi.org/10.1016/j.joms.2012.09.002.

[141] L. De Nardo, S. Bertoldi, A. Cigada, M.C. Tanzi, H.J. Haugen, S. Farè, Preparation and characterization of shape memory polymer scaffolds via solvent casting/particulate leaching, J. Appl. Biomater. Funct. Mater. 10 (2012) 119–126. https://doi.org/10.5301/JABFM.2012.9706.

[142] A. Shah Idil, N. Donaldson, The use of tungsten as a chronically implanted material, J. Neural Eng. 15 (2018) 1–13. https://doi.org/10.1088/1741-2552/aaa502.

[143] I. Dion, C. Baquey, B. Candelon, J.R. Monties, Hemocompatibility of titanium nitride,

Int. J. Artif. Organs. 15 (1992) 617–621. https://doi.org/10.1177/039139889201501009.

[144] M.H. Ahmed, J.A. Byrne, T.E. Keyes, W. Ahmed, A. Elhissi, M.J. Jackson, E. Ahmed, Characteristics and applications of titanium oxide as a biomaterial for medical implants, in: J.P. Davim (Ed.), Des. Manuf. Med. Devices, Woodhead Publishing, 2012: pp. 1–57. https://doi.org/10.1533/9781908818188.1.

[145] S.A. Skoog, Q. Lu, R.A. Malinauskas, A. V. Sumant, J. Zheng, P.L. Goering, R.J. Narayan, B.J. Casey, Effects of nanotopography on the in vitro hemocompatibility of nanocrystalline diamond coatings, J. Biomed. Mater. Res. - Part A. 105 (2017) 253–264. https://doi.org/10.1002/jbm.a.35872.

[146] Y.L. Jeyachandran, E. Mielczarski, B. Rai, J.A. Mielczarski, Quantitative and qualitative evaluation of adsorption/desorption of bovine serum albumin on hydrophilic and hydrophobic surfaces, Langmuir. 25 (2009) 11614–11620. https://doi.org/10.1021/la901453a.

[147] C. Popov, H. Vasilchina, W. Kulisch, F. Danneil, M. Stüber, S. Ulrich, A. Welle, J.P. Reithmaier, Wettability and protein adsorption on ultrananocrystalline diamond/amorphous carbon composite films, Diam. Relat. Mater. 18 (2009) 895–898. https://doi.org/10.1016/j.diamond.2009.02.004.

[148] G.G. Belz, Elastic properties and Windkessel function of the human aorta, Cardiovasc. Drugs Ther. 9 (1995) 73–83. https://doi.org/10.1007/BF00877747.

[149] R.E. Shadwick, Elasticity in Arteries: A similar combination of rubbery and stiff materials creates common mechanical properties in blood vessels of vertebrates and some invertebrates, Am. Sci. 86 (1998) 535–541. http://www.jstor.org/stable/27857132.

[150] 19.3 Cardiac Cycle – Anatomy & Physiology, (n.d.). https://open.oregonstate.education/aandp/chapter/19-3-cardiac-cycle/ (accessed December 9, 2021).

[151] H.K. Hammond, Exercise and the Cardiovascular System, Third Edition, Elsevier, 2014. https://doi.org/10.1016/b978-0-12-801238-3.00023-4.

[152] M.J. Thubrikar, M. Labrosse, J. Robicsek, Al-Soudi, B. Fowler, Mechanical properties of abdominal aortic aneurysm wall, J. Med. Eng. Technol. 25 (2001) 133–142. https://doi.org/10.1080/03091900110057780.

[153] A. Tuissi, S. Carr, J. Butler, A.A. Gandhi, L. O'Donoghue, K. McNamara, J.M. Carlson,

S. Lavelle, P. Tiernan, C.A. Biffi, P. Bassani, S.A.M. Tofail, Radiopaque Shape Memory Alloys: NiTi–Er with Stable Superelasticity, Shape Mem. Superelasticity. 2 (2016) 196–203. https://doi.org/10.1007/s40830-016-0066-z.

ANNEXURE

Permission for Fig. 1.2

Copyright Clearance Center Marketplace™

American Society of Neuroradiology - License Terms and Conditions

This is a License Agreement between Devarshi Kashyap ("You") and American Society of Neuroradiology ("Publisher") provided by Copyright Clearance Center ("CCC"). The license consists of your order details, the terms and conditions provided by American Society of Neuroradiology, and the CCC terms and conditions.

All payments must be made in full to CCC.

Order Date	15-Apr-2021	**Type of Use**	Republish in a thesis/dissertation
Order license ID	1016601-1	**Publisher**	WILLIAMS & WILKINS CO.]; American Society of Neuroradiology
ISSN	0195-6108	**Portion**	Image/photo/illustration

LICENSED CONTENT

Publication Title	AJNR, American journal of neuroradiology	**Country**	United States of America
		Rightsholder	American Society of Neuroradiology
Author/Editor	AMERICAN SOCIETY OF NEURORADIOLOGY., AMERICAN ROENTGEN RAY SOCIETY.	**Publication Type**	Journal
Date	01/01/1980		
Language	English		

REQUEST DETAILS

Portion Type	Image/photo/illustration	**Distribution**	Worldwide
Number of images / photos / illustrations	1	**Translation**	Original language of publication
Format (select all that apply)	Print, Electronic	**Copies for the disabled?**	No
		Minor editing privileges?	No
Who will republish the content?	Academic institution	**Incidental promotional use?**	No
Duration of Use	Life of current edition	**Currency**	USD
Lifetime Unit Quantity	Up to 499		
Rights Requested	Main product		

NEW WORK DETAILS

Title	3D printed Embolic agent for endovascular embolization	**Institution name**	IITG Guwahati
		Expected presentation date	2020-05-01
Instructor name	Devarshi Kashyap		

ADDITIONAL DETAILS

Order reference number	N/A	**The requesting person / organization to appear on the license**	Devarshi Kashyap

REUSE CONTENT DETAILS

Title, description or numeric reference of the portion(s)	fig 3	**Title of the article/chapter the portion is from**	Retrospective Review of Cerebral Mycotic Aneurysms in 26 Patients: Focus on Treatment in Strongly Immunocompromised Patients with a Brief Literature Review
Editor of portion(s)	N/A		
Volume of serial or monograph	N/A		
Page or page range of portion	826	**Author of portion(s)**	AMERICAN SOCIETY OF NEURORADIOLOGY.; AMERICAN ROENTGEN RAY SOCIETY.
		Issue, if republishing an article from a serial	N/A
		Publication date of portion	1980-01-01

Permission for Fig 1.3 (a)

WOLTERS KLUWER HEALTH, INC. LICENSE
TERMS AND CONDITIONS
Apr 15, 2021

This Agreement between Devarshi Kashyap ("You") and Wolters Kluwer Health, Inc. ("Wolters Kluwer Health, Inc.") consists of your license details and the terms and conditions provided by Wolters Kluwer Health, Inc. and Copyright Clearance Center.

License Number	4770610146665
License date	Feb 16, 2020
Licensed Content Publisher	Wolters Kluwer Health, Inc.
Licensed Content Publication	Circulation
Licensed Content Title	Thoracic and Abdominal Aortic Aneurysms
Licensed Content Author	Eric M. Isselbacher
Licensed Content Date	Feb 15, 2005
Licensed Content Volume	111
Licensed Content Issue	6
Type of Use	Dissertation/Thesis
Requestor type	University/College
Sponsorship	No Sponsorship
Format	Print and electronic
Will this be posted online?	No
Portion	Figures/tables/illustrations
Number of figures/tables/illustrations	1
Author of this Wolters Kluwer article	No
Will you be translating?	No
Intend to modify/change the content	No
Title	3D printed embolic agent for endovascular embolization
Institution name	IITG guwahati
Expected presentation date	May 2020
Portions	11
Requestor Location	Devarshi Kashyap T-63, Brahmaputra Hostel IIT Guwahati North guwahati Guwahati, Assam 781039 India Attn: Devarshi Kashyap
Billing Type	Invoice
Billing Address	Devarshi Kashyap T-63, Brahmaputra Hostel IIT Guwahati North guwahati Guwahati, India 781039 Attn: Devarshi Kashyap

Total 0.00 USD

Permission for Fig. 1.3(b)

All research articles published in **Journal of American Heart Association are fully Open Access:** immediately, freely available to read, download, and share. Articles are published under the terms of either the Creative Commons Attribution Non-Commercial License (CC BY-NC), which permits use, distribution, and reproduction in any medium, provided the original work is properly cited and is not used for commercial purposes; or the Creative Commons Attribution Non-Commercial NoDerivatives license (CC BY-NC-ND) which permits use and distribution in any medium, provided the original work is properly cited, the use is non-commercial and no modifications or adaptations are made.

Permission for Fig. 1.4

Reuse of Content Within a Thesis or Dissertation

Content (full-text or portions thereof) may be used in print and electronic versions of a dissertation or thesis without formal permission from the Massachusetts Medical Society (MMS), Publisher of the **New England Journal of Medicine**.

The following credit line must be printed along with the copyrighted material:

Reproduced with permission from (scientific reference citation), Copyright Massachusetts Medical Society.

Permission for Fig. 1.5

Fwd: Permission for using Fig. 2 from Clip ligation for ruptured intracranial aneurysm in a child with Loeys-Dietz syndrome: case report permissions <permissions@thejns.org>
Fri 4/16/2021 7:12 PM

To: Devarshi Kashyap <k.devarshi@iitg.ac.in>

Non-exclusive permission is granted at no charge for the use you describe, provided proper credit is given as determined by style guidelines of the publisher of the new work, or by some accepted style such as AP or Chicago. Please save this communication as proof of permission grant.

Best of luck on your thesis!

Gillian
Gillian Shasby
permissions@thejns.org

> Begin forwarded message:
> From: Devarshi Kashyap
> <k.devarshi@iitg.ac.in>
> Subject: Permission for using Fig. 2 from Clip ligation for ruptured intracranial aneurysm in a child with Loeys-Dietz syndrome: case report
> Date: April 15, 2021 at 1:40:10 PM EDT
> To: "permissions@thejns.org" <permissions@thejns.org>
>
> Respected Sir/Madam
>
> It will be very kind of you if you would grant me permission to use Fig.2 from the journal Clip ligation for ruptured intracranial aneurysm in a child with Loeys-Dietz syndrome: case report in my thesis report "DEVELOPMENT OF POROUS, PATIENT SPECIFIC SHAPE MEMORY POLYMER COMPOSITES AS AN EMBOLIC AGENT FOR ENDOVASCULAR EMBOLIZATION". The expected date of publication is 31st July 2021.
>
> Thanking you.
>
> Devarshi Kashyap
> Research Scholar,
> Dept.of Mechanical Engineering
> IITG, Guwahati

Permission for Fig. 1.6

SPRINGER NATURE LICENSE
TERMS AND CONDITIONS
Apr 15, 2021

This Agreement between Devarshi Kashyap ("You") and Springer Nature ("Springer Nature") consists of your license details and the terms and conditions provided by Springer Nature and Copyright Clearance Center.

License Number	5050321148599
License date	Apr 15, 2021
Licensed Content Publisher	Springer Nature
Licensed Content Publication	Nature Reviews Disease Primers
Licensed Content Title	Brain arteriovenous malformations
Licensed Content Author	Michael T. Lawton et al
Licensed Content Date	May 28, 2015
Type of Use	Thesis/Dissertation
Requestor type	academic/university or research institute
Format	print and electronic
Portion	figures/tables/illustrations
Number of figures/tables/illustrations	1
High-res required	no
Will you be translating?	no
Circulation/distribution	1 - 29
Author of this Springer Nature content	no
Title	3D printed embolic agent for endovascular embolization
Institution name	IITG guwahati
Expected presentation date	May 2021
Portions	1
Requestor Location	Devarshi Kashyap T-63, Brahmaputra Hostel IIT Guwahati North guwahati Guwahati, Assam 781039 India Attn: Devarshi Kashyap
Total	0.00 USD

Permission for Fig. 1.8

ELSEVIER LICENSE
TERMS AND CONDITIONS
Aug 03, 2020

This Agreement between Devarshi Kashyap ("You") and Elsevier ("Elsevier") consists of your license details and the terms and conditions provided by Elsevier and Copyright Clearance Center.

License Number	4881691052721
License date	Aug 03, 2020
Licensed Content Publisher	Elsevier
Licensed Content Publication	Computers & Graphics
Licensed Content Title	Interactive blood-coil simulation in real-time during aneurysm embolization
Licensed Content Author	Yiyi Wei,Stéphane Cotin,Jérémie Allard,Le Fang,Chunhong Pan,Songde Ma
Licensed Content Date	Apr 1, 2011
Licensed Content Volume	35
Licensed Content Issue	2
Licensed Content Pages	9
Start Page	422
End Page	430
Type of Use	reuse in a thesis/dissertation
Portion	figures/tables/illustrations
Number of figures/tables /illustrations	1
Format	both print and electronic
Are you the author of this Elsevier article?	No
Will you be translating?	No
Title	3D printed embolic agent for endovascular embolization
Institution name	IITG guwahati
Expected presentation date	May 2021
Portions	Fig 1
Requestor Location	Devarshi Kashyap T-63, Brahmaputra Hostel IIT Guwahati North guwahati Guwahati, Assam 781039 India Attn: Devarshi Kashyap
Publisher Tax ID	GB 494 6272 12
Total	0.00 USD

Permission for Fig. 1.9

ELSEVIER LICENSE
TERMS AND CONDITIONS
Apr 15, 2021

This Agreement between Devarshi Kashyap ("You") and Elsevier ("Elsevier") consists of your license details and the terms and conditions provided by Elsevier and Copyright Clearance Center.

License Number	4931350502082
License date	Oct 17, 2020
Licensed Content Publisher	Elsevier
Licensed Content Publication	Indian Heart Journal
Licensed Content Title	Vascular plugs – A key companion to Interventionists – 'Just Plug it'
Licensed Content Author	Sivasubramanian Ramakrishnan
Licensed Content Date	July–August 2015
Licensed Content Volume	67
Licensed Content Issue	4
Licensed Content Pages	7
Start Page	399
End Page	405
Type of Use	reuse in a thesis/dissertation
Portion	figures/tables/illustrations
Number of figures/tables /illustrations	1
Format	both print and electronic
Are you the author of this Elsevier article?	No
Will you be translating?	No
Title	3D printed embolic agent for endovascular embolization
Institution name	IITG guwahati
Expected presentation date	May 2021
Portions	1
Requestor Location	Devarshi Kashyap T-63, Brahmaputra Hostel IIT Guwahati North guwahati Guwahati, Assam 781039 India Attn: Devarshi Kashyap
Publisher Tax ID	GB 494 6272 12
Total	0.00 USD

Permission for Fig. 1.10

SPRINGER NATURE LICENSE
TERMS AND CONDITIONS
Apr 15, 2021

This Agreement between Devarshi Kashyap ("You") and Springer Nature ("Springer Nature") consists of your license details and the terms and conditions provided by Springer Nature and Copyright Clearance Center.

License Number	5050330011390
License date	Apr 15, 2021
Licensed Content Publisher	Springer Nature
Licensed Content Publication	Nature Reviews Disease Primers
Licensed Content Title	Uterine fibroids
Licensed Content Author	Elizabeth A. Stewart et al
Licensed Content Date	Jun 23, 2016
Type of Use	Thesis/Dissertation
Requestor type	academic/university or research institute
Format	print and electronic
Portion	figures/tables/illustrations
Number of figures/tables/illustrations	1
High-res required	no
Will you be translating?	no
Circulation/distribution	1 - 29
Author of this Springer Nature content	no
Title	3D printed embolic agent for endovascular embolization
Institution name	IITG guwahati
Expected presentation date	May 2021
Portions	7b
Requestor Location	Devarshi Kashyap T-63, Brahmaputra Hostel IIT Guwahati North guwahati Guwahati, Assam 781039 India Attn: Devarshi Kashyap
Total	0.00 USD

Permission for Fig. 1.11

ELSEVIER LICENSE
TERMS AND CONDITIONS
Apr 15, 2021

This Agreement between Devarshi Kashyap ("You") and Elsevier ("Elsevier") consists of your license details and the terms and conditions provided by Elsevier and Copyright Clearance Center.

License Number	4881920779300
License date	Aug 04, 2020
Licensed Content Publisher	Elsevier
Licensed Content Publication	Journal of Controlled Release
Licensed Content Title	Polymeric materials for embolic and chemoembolic applications
Licensed Content Author	Azadeh Poursaid,Mark Martin Jensen,Eugene Huo,Hamidreza Ghandehari
Licensed Content Date	Oct 28, 2016
Licensed Content Volume	240
Licensed Content Issue	n/a
Licensed Content Pages	20
Start Page	414
End Page	433
Type of Use	reuse in a thesis/dissertation
Portion	figures/tables/illustrations
Number of figures/tables /illustrations	1
Format	both print and electronic
Are you the author of this Elsevier article?	No
Will you be translating?	No
Title	3D printed embolic agent for endovascular embolization
Institution name	IITG guwahati
Expected presentation date	May 2021
Portions	Fig 1
Requestor Location	Devarshi Kashyap T-63, Brahmaputra Hostel IIT Guwahati North guwahati Guwahati, Assam 781039 India Attn: Devarshi Kashyap
Publisher Tax ID	GB 494 6272 12
Total	0.00 USD

Permission for Fig. 2.1

ELSEVIER LICENSE
TERMS AND CONDITIONS
Apr 15, 2021

This Agreement between Devarshi Kashyap ("You") and Elsevier ("Elsevier") consists of your license details and the terms and conditions provided by Elsevier and Copyright Clearance Center.

License Number	4786540437700
License date	Mar 12, 2020
Licensed Content Publisher	Elsevier
Licensed Content Publication	Progress in Polymer Science
Licensed Content Title	Shape memory polymers: Past, present and future developments
Licensed Content Author	Martin D. Hager,Stefan Bode,Christine Weber,Ulrich S. Schubert
Licensed Content Date	October–November 2015
Licensed Content Volume	49
Licensed Content Issue	n/a
Licensed Content Pages	31
Start Page	3
End Page	33
Type of Use	reuse in a thesis/dissertation
Portion	figures/tables/illustrations
Number of figures/tables /illustrations	1
Format	both print and electronic
Are you the author of this Elsevier article?	No
Will you be translating?	No
Title	3D printed embolic agent for endovascular embolization
Institution name	IITG guwahati
Expected presentation date	May 2020
Portions	fig 2
Requestor Location	Devarshi Kashyap T-63, Brahmaputra Hostel IIT Guwahati North guwahati Guwahati, Assam 781039 India Attn: Devarshi Kashyap
Publisher Tax ID	GB 494 6272 12
Total	**0.00 USD**

Permission for Fig. 2.2

Reprints and Permissions

J.Z. Gul, M. Sajid, M.M. Rehman, G.U. Siddiqui, I. Shah, K.H. Kim, J.W. Lee, K.H. Choi, 3D printing for soft robotics–a review, Sci. Technol. Adv. Mater. 19 (2018) 243–262. https://doi.org/10.1080/14686996.2018.1431862.

PUBLICATIONS AND CONFERENCES

Journals:

1) **Devarshi Kashyap**, Kishore Kumar Padi, S Kanagaraj, 4D printed porous radiopaque shape memory polyurethane for endovascular embolization. Additive Manufacturing 24 (2018); 687-695. 10.1016/j.addma.2018.04.009 (IF: 7.002)
2) **Devarshi Kashyap,** Surendra Gaur, S Kanagaraj, Development of hybrid shape memory polyurethane composites for endovascular applications. Materials Today Communications 22, (2020); 100751-100643. https://doi.org/10.1016/j.mtcomm. 2019. 100751 (IF: 2.67)
3) 3D printed nano $BaSO_4$ shape memory polyurethane composites for endovascular embolization. (Under preparation)

Book chapters:

1) **Devarshi Kashyap**, S Kanagaraj, Injectable Biomaterials for Endovascular Applications.; Advances in Polymer Materials and Technology (2016); Edited by Anandhan Srinivasan, Sri Bandyopadhyay. CRC press. Pages: 641-658, ISBN 9781498718813.
2) **Devarshi Kashyap**, Charan Mukundan, S Kanagaraj, Manufacturing and characterization of shape memory polymer and composites.; Primary and Secondary Manufacturing of Polymer Matrix Composites (2017); Edited by Kishore Debnath, Inderdeep Singh. CRC press. Pages: 43-74. ISBN978-1498799300.
3) **Devarshi Kashyap**, Vaibhav Jaiswal, S Kanagaraj, Biomaterials for Biomedical Devices and implants.; Advances in Sustainable Polymers: Processing and Application (2019); Edited by Vimal Katiyar, Raghvendra Gupta, Tabli Ghosh. Springer Pages: 85-109. ISBN 978-981-329-804-0

Conference (Oral/Poster):

1) **Devarshi Kashyap** and S. Kanagaraj, 3D Printed custom shaped radiopaque Shape Memory Composites as embolic materials for the treatment of cardiovascular malformation.; World Congress on Cardiac Sciences, 28-29th November 2018, Bangalore.
2) **Devarshi Kashyap** and S Kanagaraj, 3D printed Shape memory polyurethane foam for endovascular embolization; 6thAsian Biomaterials Congress (ABMC6), 25-27th October 2017, Thiruvananthapuram.

3) **Devarshi Kashyap** and S. Kanagaraj, Shape memory polymers for morphing wings; International Workshops, Conferences and Expo for Military and Marine Applications (IWCEM 2016), 4-6th June 2016, Jaipur.
4) **Devarshi Kashyap** and S. Kanagaraj, Development of nano-barium sulfate filled shape memory polymer composite for endovascular embolization.; Indo-Australian conference on biomaterials, tissue engineering, drug delivery system and Regenerative medicine (BiTERM-2016), 15-17th April 2016, New Delhi.
5) **Devarshi Kashyap** and S. Kanagaraj, Influence of nano BaSO4 particles on the mechanical properties of Shape memory polyurethane for the endovascular applications.; Indo-Australian conference on biomaterials, tissue engineering, drug delivery system and Regenerative medicine (BiTERM-2015), 5-7th February 2015, Chennai.

Awards:

1) Awarded **Prof S. Rajeswari award for best presentation**, Devarshi Kashyap and S. Kanagaraj; Radiopaque shape memory polymers for minimally invasive embolization.; National conference on Emerging Biomaterials (NCEB-2016), 19-21st October 2016, Coimbatore.